Modification of human Kv4 channels by KChIP1 splice variants

Dissertation

zur Erlangung des akademischen Grades eines

Doktors der Medizin (Dr. med.)

an der

Medizinischen Fakultät der Universität Hamburg

vorgelegt von

Wuyou Cao

aus

Jiangsu, China

2025

Betreuer:in / Gutachter:in der Dissertation: Prof. Dr. Robert Bähring
Gutachter:in der Dissertation: PD Dr. Torsten Christ

Vorsitz der Prüfungskommission: PD Dr. Torsten Christ
Mitglied der Prüfungskommission: Prof. Dr. Andreas Metzner
Mitglied der Prüfungskommission: PD Dr. Georg Rosenberger

Datum der mündlichen Prüfung: 11.11.2025

Content

1. Research hypothesis and questions

Voltage-gated potassium channels of the Kv4 subfamily mediate a subthreshold-activating somatodendritic A-type current (I_{SA}), which controls repetitive firing, dendritic excitation and synaptic plasticity (Hoffman et al., 1997; Johnston et al., 2003). Native Kv4 channels form ternary complexes with two types of auxiliary β-subunits, Kv channel interacting proteins (KChIPs) and dipeptidyl amino peptidase-related proteins (DPPs) (An et al., 2000; Maffie and Rudy, 2008; Nadal et al., 2003), which enhance Kv4 channel surface expression and modulate inactivation gating properties. In general, macroscopic inactivation (i.e., current decay) of Kv4 channels is accelerated by DPPs and slowed by KChIPs, whereas recovery from inactivation is accelerated by both KChIPs and DPPs (An et al., 2000; Bähring et al., 2001b; Beck et al., 2002; Jerng et al., 2007). However, our knowledge of the concerted modulation of channel properties by DPPs and KChIPs, especially by certain β-subunit splice variants is still fragmentary. Two splice variants of KChIP1 (a shorter KChIP1a and a longer KChIP1b), exhibit distinct effects on the recovery from inactivation. KChIP1b had been found to induce an extremely slow recovery component upon transient transfection of a stable Kv4.2-expressing cell-line with KChIP1b cDNA, while the effect of KChIP1a on recovery kinetics had been described as typical (Van Hoorick et al, 2003; Van Hoorick et al., 2007).

We hypothesized that KChIP1b effects on Kv4 channels is a prominent intrinsic feature of this β-subunit with general applicability, which differs from KChIP1a effects. However, KChIP1 transient cDNA transfection of a stable Kv4.2-expressing cell-line, as done previously, may be problematic because it does not control the transfection efficiency, and temporal expression profiles of α- and β-subunits may differ, which may result in the co-existence of Kv4.2 and Kv4.2 + KChIP1b complexes, leading to the observed biphasic kinetics of recovery. In order to rigorously test our hypothesis, we asked whether the special KChIP1b feature of slowing recovery from inactivation, previously reported for Kv4.2, can be also observed for other Kv4 channel subtypes and in a ternary configuration with DPP6, independent of the utilized expression system and recording technique. We further asked what are the mechanisms underlying the KChIP1b-mediated recovery kinetics. In order to answer the questions, our data were obtained with two-electrode voltage clamp under different conditions in cRNA-injected *Xenopus laevis* oocytes.

2. Introduction

2.1 Potassium channels

Among the various ion channels, potassium channels (K^+ channels) are the largest and most heterogeneous group (Coetzee et al., 1999), which can be found in almost all species, except for some parasites (Kuo et al., 2005). They participate in a variety of physiological processes, such as control of membrane potential, signal transduction, homeostasis of potassium and modulation of hormone secretion (Hille, 2001).

Based on the numbers of transmembrane segments, presence of voltage sensor domain and the pore-forming domains of the α-subunits, K^+ channels can be divided into five groups: (1) The simplest α-subunit of K^+ channels consists of only two transmembrane segments connected by a pore loop with a selectivity filter (2TM, 1P; Figure 2.1A), and it assembles as tetramers (González et al., 2012). These α-subunits had been found in the inward rectifier family (Kir channel) (Hibino et al., 2010). The Kir channels are grouped into 7 subfamilies (Kir1.x-Kir7.x), which allow K^+ ions to flow more easily into the cell than out of it and conduct inward currents because K^+ ions are conducted during hyperpolarization (Guo et al., 2003). (2) The α-subunit of two-pore domain potassium channels family (K_{2P} channel) contains four transmembrane segments and two pore-forming domains (4TM, 2P; Figure 2.2B). These channels assemble as dimers. K_{2P} channels can be classified into six subfamilies: TWIK, TASK, TREK, THIK, TALK and TRESK (Goldstein et al., 1996), which produce leak K^+ currents (also known as background K^+ currents) and are usually constitutively open (Piechotta et al., 2011). Leak K^+ currents play an important role in setting negative resting membrane potential and counterbalance depolarization (Enyedi and Czirják, 2010), with the feature of weak voltage dependence and sensitivity to the external factors, such as pH, temperature and regulatory proteins (Buckingham et al., 2005). (3) The α-subunit of voltage-gated potassium channels (Kv channels) contains six transmembrane segments (S1-S6) with the presence of voltage sensor domain (VSD) and a pore-forming domain (6TM with V-sensor, 1P; Figure 2.1C). The functional channel of Kv channels is composed of four α-subunits. Kv channels are the largest group of K^+ channels and consist of twelve members (Kv1-Kv12) according to amino acid sequence similarity (detailed information will be described later in Chapter 2.2). (4) K^+ channels that contain S1-S6 with no VSD and a pore-forming domain (6TM no V-sensor, 1P; Figure 2.1D) include the subfamily of small conductance Ca^{2+}-activated K^+ channels (SK channels). SK channels, which is divided into four subfamilies (SK1, SK2, SK3, SK4), are voltage independent and can be activated by a

low level of intracellular Ca^{2+} (< 1 μM) (Girault et al.,2012). SK channels are sensitive to Ca^{2+} ions, resulting in the involvement in regulation of Ca^{2+} signaling pathways, both in excitable and non-excitable cells (Dolga et al., 2011). SK4 is also referred as IK (intermediate conductance Ca^{2+}-activated K^+ or $K_{ca}3.1$) due to a higher conductance 20-80 pS (Vergara et al., 1998).

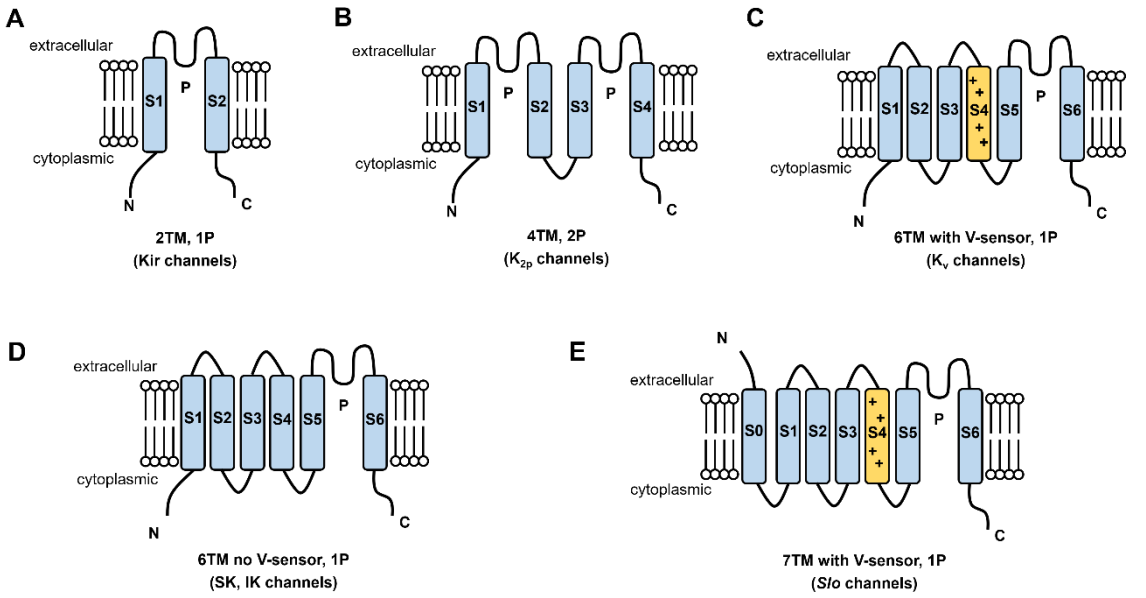

Figure 2.1 Topology of K^+ channel α-subunit. A: The α-subunit of Kir channels contains two transmembrane segments (TM; blue) and one pore-forming domain (P). B: The α-subunit of K_{2P} channels is formed from two subunits with 4TM and 2P. C: The α-subunits of voltage-dependent Kv channels have 6TM with the presence of voltage sensor (V-sensor; yellow) and 1P. D: The α-subunits of SK and IK channels contain 6TM with no V-sensor and 1P. E: The α-subunits of Slo channels contain 7TM and 1P. Extracellular and cytoplasmic side indicated, with an intracellular N-terminus (N) and an intracellular C-terminus (C).

(4) The α-subunits of *Slo* channel subfamily that form a tetrameric structure with seven transmembrane segments and one pore-forming domain (7TM, 1P; Figure 2.1E). *Slo* channels encoded by *Slo* genes consist of 4 members (*Slo*1, *Slo*2.1, *Slo*2.2, *Slo*3). In addition to the S1-S6 segments, *Slo*1 and *Slo*3 have a S0 segment in front of the S1, which is necessary for β-subunit modulation and voltage sensitivity (Koval et al., 2007). *Slo*1 and *Slo*3 belong to the "big" potassium channels (BK channels), which have high conductance and are calcium- and voltage- activated potassium channels (Zang et al., 2018). Due to their large conductance, BK channels can disproportionally affect neuronal excitability. However, *Slo*2.1 and *Slo*2.2 are different and have α-subunits containing six transmembrane segments, similar like Kv channels. *Slo*2 conduct high-conductance single-channel currents similar to

BK currents, but were activated by Na^+ instead of Ca^{2+}(Salkoff et al., 2006).

Most K^+ channels share a common amino acid sequence, GYG, which is also called the potassium channel signature sequence and located in the pore loop of the α-subunits. This sequence functions as the basis for a selectivity filter to conduct K^+ ions in the tetrameric complex (see below) and enable K^+ channels to be highly selective (Heginbotham et al., 1994). EAG-like K^+ channels and Kir6 channels subfamily contain a distinct sequence, GFG (Kim and Nimigean, 2016). Normally, K^+ channels are at least 10,000 times more permeable to K^+ ions than sodium (Na^+) ions (Doyle et al., 1998).

2.2 Voltage-gated potassium channels

Voltage-gated potassium channels or Kv channels, encoded by 40 different genes, are the largest group of K^+ channels and consist of a total of 12 subfamilies. Figure 2.2 shows two phylogenetic tree reconstructions, one for the Kv1-Kv9 families and the other for the Kv10-Kv12 families (EAG-family), based on amino acid sequence alignments of the hydrophobic core of the proteins and structural similarity (Gutman et al., 2005).

The first voltage-gated potassium channel, called *Shaker* channel or Kv1 channel, was cloned from *Drosophila melanogaster* in 1987 (Kamb et al., 1987), which served as the foundation to study the function and structure of other Kv channels. Shortly afterwards, three genes homologous to *Shaker* were discovered. The channels encoded by these three genes were named *Shab* (Kv2), *Shaw* (Kv3) and *Shal* (Kv4) channels (Salkoff et al., 1992). The molecular structures of Kv channels remain very similar. All Kv channels form homotetramers or heterotetramers of α-subunits, containing six transmembrane segments (S1-S6), intracellular N- and a C-termini, connected to S1 and S6, respectively (Lamothe et al., 2018). These helices can be divided into two important parts: segments S1-S4 form a voltage sensor domain (VSD), and segments S5-S6 comprise the pore domain (Long et al., 2007) (Figure 2.3).

The Kv channels are characterized by containing VSDs that carry many positively charged amino acids residues (arginine and lysine) in S4 segments, which make Kv channels electrically sensitive to the changes of membrane potential (Gutman et al., 2005). Upon membrane depolarization, the S4 segment goes up because of the movements of charge, and shifts outward across the membrane, which causes a conformational change and the opening of the channel pore, leading to voltage-dependent activation (Grizel et al., 2014). After the activation of the four voltage sensors, the movement will be transferred to the S6 segment

via the S4-S5 linkers. After the opening of the Kv channels, the K^+ ions are able to pass through the selectivity filter.

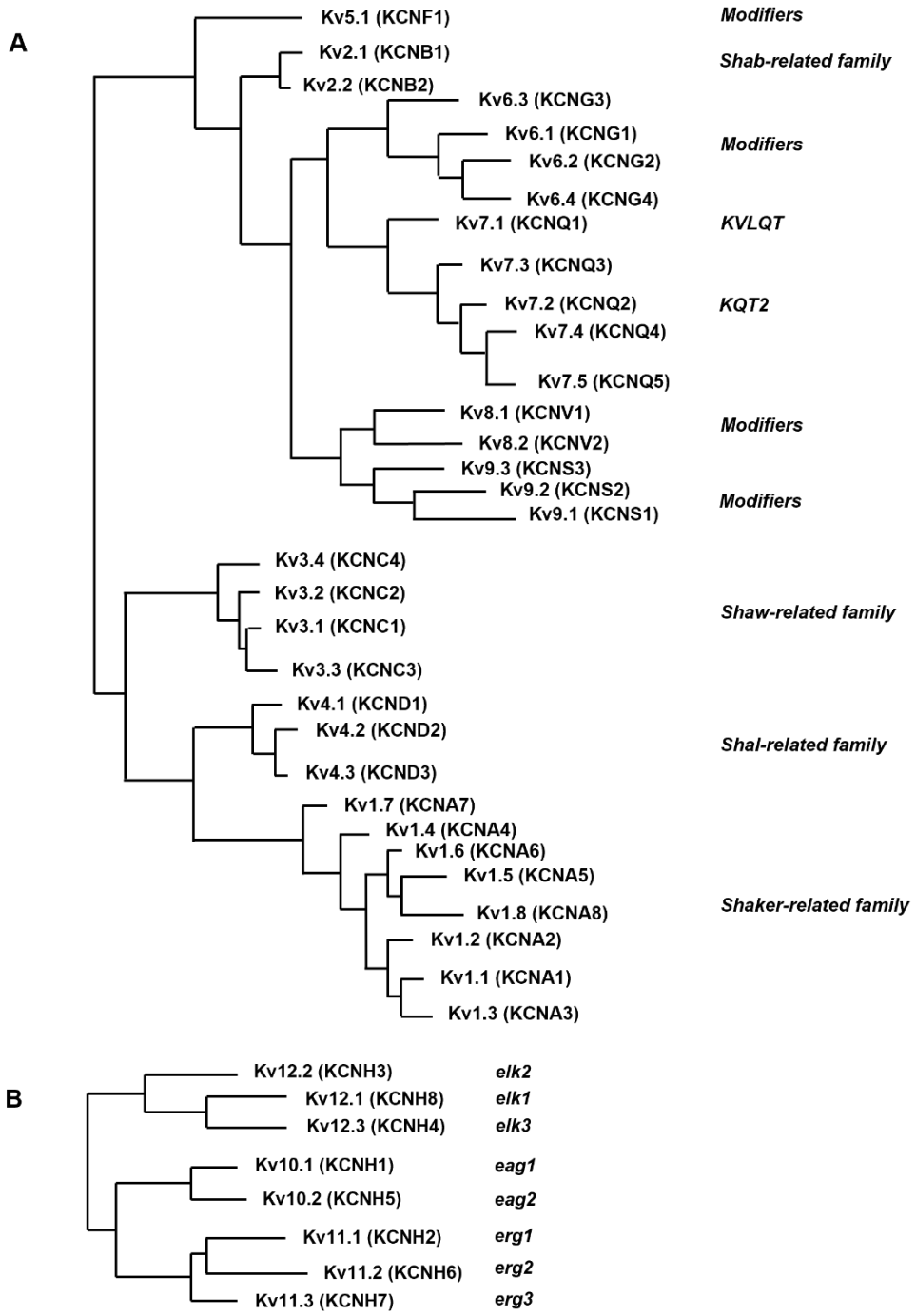

Figure 2.2 Phylogenetic trees for Kv1-12 families. A: Phylogenetic tree for the Kv1-9 families. Kv5, Kv6, Kv8 and Kv9 channels share similar structure, but they do not form functional channels and function as modifiers. Kv1 channels belong to *Shaker*-related family, Kv2 channels belong to *Shab*-related family, Kv3 channels belong to *Shaw*-related family and Kv4 channels belong to *Shal*-related family. An alternative name for Kv7.1 is KVLQT, while for Kv7.2 is KQT2. B: Phylogenetic tree for the Kv10-12 families (EAG-family). Kv10, Kv11 and Kv12 channels share less structural similarity to the classical Kv channels shown in A, and were originally named *eag, erg* and *elk* channels, respectively. The human gene names are shown in brackets together with the official IUPHAR (International Union of Pharmacology) receptor name, and other used names are shown next to it (Gutman et al., 2005).

For Kv1, Kv2, Kv3 and Kv4 channels, the cytoplasmic N-terminal region of the channel contains a tetramerization T1 domain, which is responsible for the assembly of α-subunits of Kv channels as tetramers into functional channels (Pischalnikova and Sokolova, 2009) and the binding of accessory β-subunits (Callsen et al., 2005). The four intracellular T1 domains are connected to the S1 segment by a S1-T1 linker (Tu et al., 2007). In contrast to Kv1-Kv4 channels, C-terminal of Kv7, Kv10, Kv11 and Kv12 channels are involved in channel assembly, gating and trafficking (Pischalnikova and Sokolova, 2009). Although Kv5, Kv6, Kv8 and Kv9 channels share the common structure as other members of the Kv channel family, they do not form functional channels. Instead, they form heterotetrameric channels with α-subunits of Kv2 and Kv3 in order to modify gating properties (Gutman et al., 2005; Salinas et al., 1997).

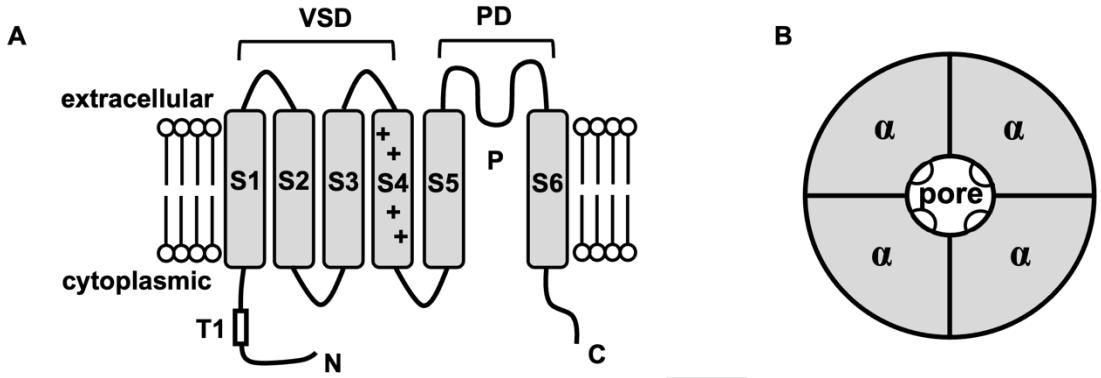

Figure 2.3 Structural organization of the Kv channel. A: The α-subunits of Kv channels consist of six transmembrane domains, S1 to S6, which are shown as gray boxes (extracellular and cytoplasmic side indicated), with an intracellular N-terminus (N) and an intracellular C-terminus (C), connected to S1 and S6, respectively. S1-S4 represent the voltage sensor domain (VSD) and the positively charged amino acid residues in S4 make the Kv channels sensitive to changes in membrane potential. S5 and S6 form the pore region (PD), and the pore loop (P) is located between S5 and S6. The pore domain contains the selectivity filter in the tetrameric complex and is responsible for the specificity of the channel. The tetramerisation domain (white box, T1), located on the N-terminal of Kv1, Kv2, Kv3 and Kv4 channels is responsible for the assembly of Kv α-subunits as tetramers into functional channels. B: An overview model of Kv channel as a tetramer. Four Kv α-subunits (α), each with a pore loop (semicircle), form a functional channel as a tetramer. Four α are arranged rotationally symmetrically around the central pore (pore). If the channel is made up of four identical α-subunits, it is called a homotetramer. If the channel is made up of different α-subunits, it is called a heterotetramer.

2.3 Classical inactivation mechanisms of Kv channels

The conformational states of Kv channels can be classified into four states: resting (closed), partially activated (closed, but opening-permissive), open and inactivated states (Bähring and Covarrubias, 2011). In the resting and partially activated states, the channels are non-conducting, however they can enter the open state and activate in response to the membrane

depolarization (Ye et al., 2022). After activation, most Kv channels do not remain open but can enter an inactivated state, in which the channels are not permeable to ions and become non-conducting despite the sustained stimulus (Jerng et al., 1999). This process is known as inactivation. The mechanisms of Kv channel inactivation are variable, which usually involve fast and slow processes particularly well studied in the *Shaker* channel (Rasmusson et al., 1998). Two classical mechanisms of *Shaker* channel inactivation are called N-type inactivation and P/C-type inactivation (Kuang et al., 2015). N-type and P/C-type inactivation belong to open-state inactivation (OSI) that the channel only enters the inactivated state (I) after channel opens (O) from the resting state (C) (Bähring and Covarrubias, 2011). The simplified gating model is shown in Figure 2.4. After the refractory period has expired, the channels switch back to the resting state and this process is referred to as recovery from inactivation.

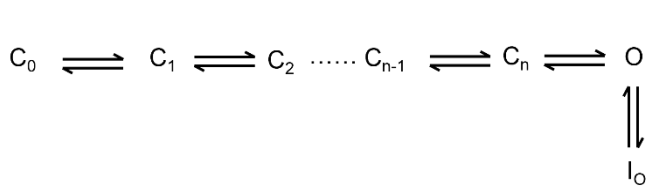

Figure 2.4 The simplified gating scheme of open-state inactivation (OSI). C, O and I represent closed, open and inactivated states, respectively. C_0 is the resting state, C_1–C_{n-1} represents a set of partially activated states, and C_n is the opening-permissive state. I_O is open-inactivated states.

2.3.1 N-type inactivation

N-type inactivation is a rapid form of inactivation and has been first described in *Shaker* B channels as a "ball-and-chain" model (Demo and Yellen, 1991), in which the cytoplasmic N-terminus (chain) carries an amino acid sequence that acts as an inactivating peptide (ball). In the "ball-and-chain" mechanism, the inactivating peptide binds to the activated channel, thereby occluding the intracellular mouth of the channel pore, preventing the further ion permeation and rendering the channel non-conducting (Rasmusson et al., 1998). The model of the "ball-and-chain" is illustrated in cartoon form in Figure 2.5A**.** One important feature of the fast N-type inactivation is that it can be prevented by deleting or enzymatic removal of the N-terminus of α-subunits of Kv channels (Hoshi et al., 1990), and can be restored by application of exogenous peptides derived from the N-terminus (Kurata and Fedida, 2006). Another feature of N-type inactivation is that it is sensitive to intracellular pore blockers, such as tetraethylammonium (TEA) and its derivatives, but is not affected by changes in the extracellular K^+ (Choi et al., 1991; Demo and Yellen, 1991). N-type inactivation keeps the

channel in an open-inactivated state and the presence of inactivating peptide prevents the channel from closing. Therefore, recovery from inactivation of *Shaker* channels usually proceeds via the open state (Demo and Yellen, 1991).

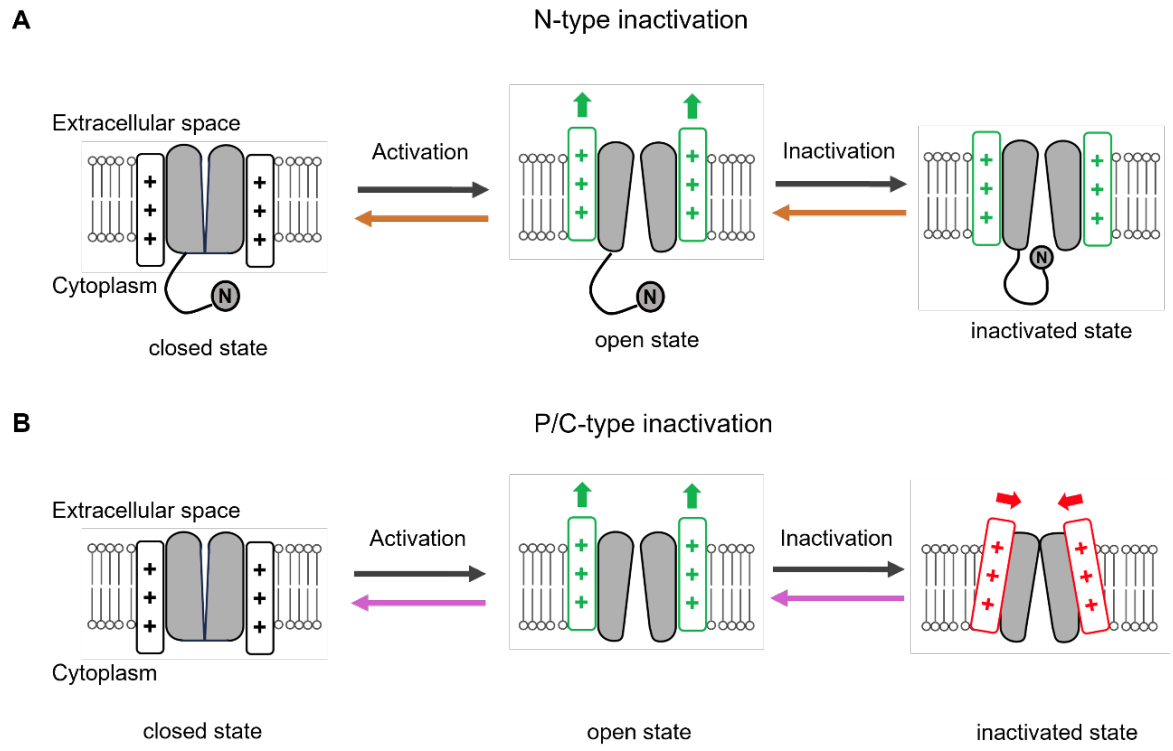

Figure 2.5 Two classical inactivation mechanisms of Kv channels. Firstly, Kv channels are in the closed state. Upon depolarization, the voltage sensor goes up, the channel starts to activate and the gate opens to form the open activated conformation (open state). After the channel opens, it enters an inactivated state where it becomes non-conductive despite the continuing depolarization. A: N-type inactivation, which resembles a "ball-and-chain" reaction, where the N-terminal (chain) inactivation peptide (ball) binds to the activated channel, thereby occluding the intracellular mouth of the channel pore. B: P/C-type inactivation is mainly characterized by a conformational rearrangement of the external pore domain through voltage sensor movement.

2.3.2 P/C-type inactivation

After removal of the N-terminus of *Shaker* channels, although the fast N-type inactivation is eliminated, a much slower inactivation process still remains, which develops over hundreds of milliseconds to seconds (Choi et al., 1991). It had been recognized that more C-terminal regions, such as the amino acid residues in the S5-, P-, and S6-segments of the channel, play a role in the slow inactivation mechanism, which had therefore been termed C-type inactivation (Chen et al., 2000; Xu and McDermott, 2019). The mechanism of C-type inactivation is mainly characterized by a conformational rearrangement of the external pore domain through voltage sensor movement, rather than involving the C-terminus (Ong et al.,

2022; Tan et al., 2022), and had later been referred to as P/C-type inactivation (Kurata et al., 2005; López-Barneo et al., 1993; Rasmusson et al., 1998). The model of P/C-type inactivation is illustrated in cartoon form in Figure 2.5B. The process of P/C-type inactivation can be slowed by elevated external K^+ concentrations and the application of extracellular TEA, as K^+ and TEA occupy the outer pore domain, inhibit conformational changes, and prevent the channel from inactivating (López-Barneo et al., 1993). The rate of recovery from P/C-type inactivation is accelerated by elevated extracellular K^+, because extracellular K^+ binds to a low-affinity modulatory site and results in the destabilization of an inactivated state (Levy and Deutsch, 1996). In contrast, P/C-type inactivation can be accelerated by methionine oxidation (Chen et al., 2000).

2.4 Kv4 subfamily channels

The Kv4 subfamily has three members, Kv4.1, Kv4.2, and Kv4.3, with a short and a long splice variant of the latter (Kv4.3S and Kv4.3L, respectively), encoded by the genes *KCND1-3* (Isbrandt et al., 2000). All these subtypes are characterized by mediating a fast transient outward A-type current, characterized by rapid activation upon membrane depolarization, fast inactivation and fast recovery from inactivation (Covarrubias et al., 2008). Kv4 channels play important roles in both the heart and the brain. In central neurons, they are expressed in the soma and dendrites, where they mediate the somatodendritic subthreshold A-type K^+ current (I_{SA}). Here, the Kv4 channels exhibit a somatodendritic distribution, with the density of the Kv4-mediated current increasing towards the distal dendrites (Hoffman et al., 1997). Therefore, I_{SA} attenuates the backpropagation of action potentials and, thus, controls dendritic excitation and synaptic plasticity (Jerng et al., 2004). In cardiomyocytes, Kv4 channels mediate the transient outward current (I_{to}) and are responsible for the early repolarization phase of the action potential (Niwa and Nerbonne, 2010).

In the brain, Kv4.1 channels are strongly expressed in granule cells (GCs), compared to CA1 or CA3 pyramidal neurons, based on *in situ* hybridization histochemistry analysis (Serôdio and Rudy, 1998). Kv4.1 channels play a role in the modulating cell proliferation in neural stem and progenitor cells. Minor changes in the biophysical properties of Kv4.1 channels may impair neuronal development and are thought to contribute to neuropsychiatric diseases (Kalm et al., 2024).In contrast, Kv4.2 and Kv4.3 are expressed at a higher level in the central nervous systems (CNS; Huang et al., 2005). Kv4.2 and Kv4.3 are localized in the somatodendritic domain of many neurons in the CNS, for example, Kv4.2 is present in the

apical and basal dendrites of hippocampal and neocortical pyramidal neurons, whereas Kv4.3 is concentrated in the somata and dendrites of hippocampal, striatal and neocortical interneurons (Rhodes et al., 2004). Kv4.2 and Kv4.3 are the major contributors to I_{SA} in central neurons (Carrasquillo et al., 2012). Furthermore, Kv4.3 is an important component of I_{to} and decreased Kv4.3 expression has been observed in many heart diseases, particularly in heart failure and cardiac hypertrophy (Huo et al., 2014). Members of Kv4 subfamily exhibit similar electrophysiological properties when expressed in heterologous expression systems (Pak et al., 1991). At the amino acid level, Kv4.2 and Kv4.3 share 75% identity and are more closely related to each other than to Kv4.1, which shares 65–68% identity with them (Nakamura et al., 2001).

2.5 Kv4 channel preferential closed-state inactivation

All Kv4 channels undergo rapid inactivation (Birnbaum et al., 2004). A simplified gating scheme of Kv4 channels is shown in Figure 2.6A. However, these processes exhibit features that are inconsistent with the classical N- and P/C-type inactivation mechanisms, as described in *Shaker* channels. The N-terminal deletion mutant of Kv4.2 channel does not show the complete loss of the fast component of the decay as observed in *Shaker* channels (Birnbaum et al., 2004). In addition, elevated external K^+ concentrations accelerate inactivation but does not affect recovery kinetics in Kv4 channels (Kaulin et al., 2008). Unlike *Shaker* channels, Kv4 channels can inactivate directly from a closed state before they open, upon a prolonged depolarization, which is referred to as closed-state inactivation (CSI) (Bähring and Covarrubias, 2011). During strong depolarization, Kv4 channels eventually accumulate in a closed-inactivated state and recover from this closed-inactivated state directly, bypassing the open state (Bähring et al., 2001a). CSI is the main inactivation mechanism of Kv4 channels, as illustrated in Figure 2.6B. A study from Ye and coworkers revealed the Kv4.2 channel structure in the closed-inactivated state (Ye et al., 2022). The inactivated conformation has an extremely narrow pore, less than 0.5 Å, which effectively inhibits ion permeation. Under this condition, the homotetrameric channel pore loses its four-fold rotational symmetry and becomes two-fold symmetric (Ye et al., 2022).

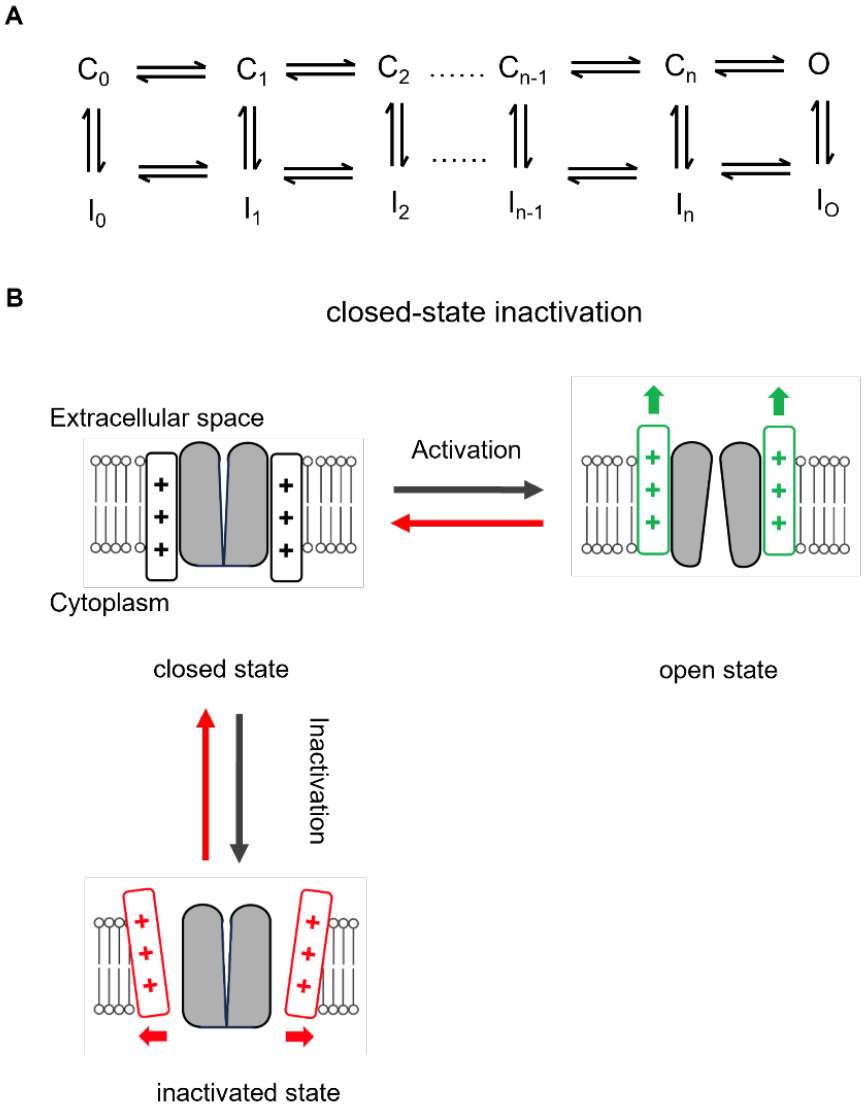

Figure 2.6 The simplified gating scheme and inactivation mechanism of closed-state inactivation (CSI) of Kv4 channels. A: C, O and I represent closed, open and inactivated states, respectively. C_0 is the resting state, C_1–C_{n-1} represents a set of partially activated states, and C_n is the opening-permissive state. I_0–I_{n-1} represents closed-inactivated states that are directly associated with inactivation-permissive closed states. I_O and I_n represent the open-inactivated and closed-inactivated states, respectively. Kv4 channel inactivation is only weakly coupled to open-permissive or open states. Recovery of Kv4 channels from inactivation and return to C occurs "silently", directly from I_n, bypassing O. B: The simplified cartoons illustrate the mechanism of CSI. Upon depolarization, the voltage sensor moves upward, the channel starts to activate and the gate opens to form the open activated conformation (open state). However, during prolonged depolarization, Kv4 channels can inactivate directly from a closed state, prior to opening.

2.6 Accessory subunits of Kv4 channels

Although α-subunits of Kv4 channels can mediate A-type currents in heterologous expression systems, such as in *Xenopus* oocytes, kinetic differences have been observed compared to native I_{SA} recorded in neuron (Maffie and Rudy, 2008). In the brain, Kv4 channels are thought to form ternary complexes with two types of auxiliary β-subunits,

dipeptidyl aminopeptidase-like proteins (DPPs) and Kv channel interacting proteins (KChIPs), both of which exist in numerous splice variants and modulate Kv4 channel surface expression as well as properties of activation and inactivation (Covarrubias et al., 2008). Cryo-EM have shown that α-subunits of Kv4 channels assemble with KChIPs and DPPs into dodecamer complexes in a 4:4:4 ratio (Figure 2.7; Kise et al., 2021).

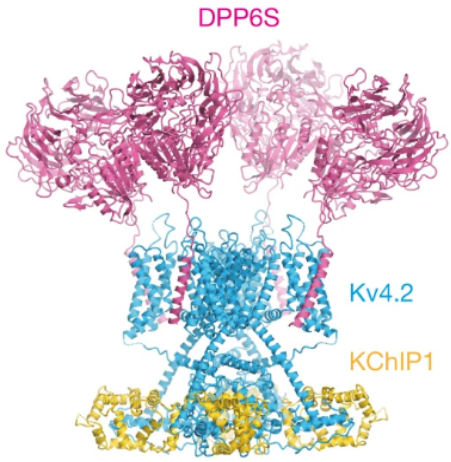

Figure 2.7 Structure of the Kv4.2-DPP6S-KChIP1 complexes (Kise et al., 2021). Kv4.2 α-subunits (blue) assemble with auxiliary subunits, KChIP1 (yellow) and DPP6S (pink), as a dodecamer in a 4:4:4 ratio.

2.6.1 Dipeptidyl-peptidase-like proteins (DPPs)

DPPs were first described in 2003 as a β-subunit associated with native Kv4 channels (Nadal et al., 2003). DPP6 and DPP10, also known as DPPX and DPPY, respectively, are two members of this protein family (Jerng et al., 2004; Qi et al., 2003). Unlike other DPP family members, both DPP6 and DPP10 carry a point mutation at the enzymatic serine, which causes a lack of peptidase activity. Instead, they play a crucial role in modulating Kv4 channel function (Strop et al., 2004).

DPP6 was the first identified member of this family, and is a type II transmembrane protein containing a single transmembrane domain, a short intracellular N-terminus, and a large extracellular domain with multiple glycosylation sites (Lin et al., 2014; Maffie et al., 2009). At least five alternatively spliced isoforms of DPP6 have been characterized: DPP6-S, DPP6-L, DPP6-K, DPP6-D and DPP6-E, which mainly differ in their cytoplasmic N-terminal regions (Maffie et al., 2009; Strop et al., 2004). When co-expressed with Kv4 channels in heterologous expression systems, such as *Xenopus* oocytes or CHO cells, DPP6 significantly increases current amplitude by enhancing membrane localization of Kv4 channels and increasing their unitary conductance (Malloy et al., 2022). Normally, DPP6

dramatically decreases the time to reach the maximum current, increases the rate of macroscopic inactivation, induces a hyperpolarizing shift in both voltage dependence of activation and steady-state inactivation curves, and accelerates the recovery from inactivation compared to Kv4 channels expressed alone (Nadal et al., 2003). DPP10, another member of the DPP family, shares 48–51% amino acid identity with DPP6 and has a similar structure (Qi et al., 2003). Similarly, DPP10 accelerates the macroscopic inactivation of Kv4.3 currents, increases surface expression of Kv4.2 channels, and produces a hyperpolarizing shift of steady-state inactivation for both Kv4.2 and Kv4.3 channels in different heterologous systems. On the contrary, DPP10 does not alter the steady-state inactivation of Kv4.1 channels, but induces a hyperpolarizing shift in the halfmaximal voltage of conductance-voltage (*G-V*) relationship. Thus, DPP6 and DPP10 produce similar, but not identical, modulatory effects on Kv4 channels (Bezerra et al., 2015; Jerng et al., 2007; Zagha et al., 2005).

2.6.2 Kv channel-interacting proteins (KChIPs)

KChIPs are another group of accessory β-subunits of Kv4 channels, which were first identified using yeast two-hybrid (YTH) system with the Kv4.3 N-terminal region as bait (An et al., 2000). KChIPs include 4 different members: KChIP1, KChIP2, KChIP3 and KChIP4, encoded by *KCNIP*1-4, respectively (Pruunsild and Timmusk, 2005). They exist in different splice variants and are highly expressed in both brain and heart (Holmqvist et al., 2002; Jerng et al., 2004). KChIPs are small cytoplasmic proteins with approximately 200-270 amino acids, which belong to the neuronal calcium sensor (NCS) family. They contains a highly conserved C-terminal core domain with four EF-hand calcium-binding motifs, and a variable N-terminal that varies in sequence and length, which determines the differences among KChIPs isoforms (Bähring, 2018). Among the four EF-hands, EF-3 and EF-4 mediate high affinity Ca^{2+} binding, EF-2 binds Mg^{2+} and EF-1 is non-functional (Jerng and Pfaffinger, 2014).

Utilizing alternative transcription start sites and alternative splicing, *KCNIP*1 leads to the synthesis of different KChIP1 isoforms, for example, KChIP1a, KChIP1b and KCNIP1-IaΔII (Pruunsild and Timmusk, 2005; Wu et al., 2023). Previous studies revealed KChIP1 was detected in multiple regions of the brain, including cortex, hippocampus, thalamus, hypothalamus, and cerebellum (Rhodes et al., 2004). KChIP1 is able to interact with all Kv4 channel subtypes. In the human heart, KChIP2 mRNA is highly expressed, and the encoded

protein assembles with Kv4.2 and Kv4.3 α-subunits to form and regulate I_{to} (Wang et al., 2022). In ventricular myocytes from KChIP2 knockout mouse, I_{to} was eliminated (Foeger et al., 2013). KChIP3 is special among four KChIP subtypes. In addition to interacting with Kv4 channels, KChIP3 has been reported to have a transcriptional regulatory function, and is therefore also referred to as DREAM, for downstream regulatory element antagonist modulator (Carrión et al., 1999). Moreover, KChIP3 may also interact with Ca^{2+}-signaling protein presenilin and, in this context, is referred to as calsenilin (Ramachandran et al., 2012). In the brain, KChIP3 are abundantly expressed in the dentate gyrus of the hippocampus and cerebellar granule cells (Jerng et al., 2005). KChIP4 was initially identified as calsenilin-like protein that binds to presenilin 2 (Alfaro-Ruíz et al., 2020). KChIP4 is concentrated in the apical and basal dendrites of cornu ammonis (CA) and subicula pyramidal neurons (Rhodes et al., 2004).

KChIPs bind to the cytoplasmic N-terminus of Kv4 α-subunits in a 4:4 ratio to form an octameric channel complex. Cryo-EM by Kise and coworkers revealed the structure of a Kv4.2/KChIP1 complex (Kise et al., 2021), showing that KChIP1s are laterally anchored to the T1 domains of Kv4.2. These interactions serve as a second connection and stabilize the T1-T1 interface by connecting two neighboring T1 domains. This structural feature is consistent with the crystal structures of the Kv4.3 + KChIP1 complex (Ma et al., 2022), and is thought to facilitate tetramerization. In the Kv4.2 + KChIP1 complex, the intracellular S6 helix interacts with the neighboring T1–S1 linker. Furthermore, the C-terminal cytoplasmic S6 helices of Kv4.2 and Kv4.3 are captured by KChIP1 through hydrophobic interactions (Kise et al., 2021; Ma et al., 2022; Wang et al., 2007). As a result, KChIPs play an important role in modulating trafficking and gating properties of Kv4 channels. In general, co-expression of Kv4 channels with KChIPs enhances surface expression, and modulates Kv4 gating properties as follows: slowing down the initial phase of Kv4 macroscopic inactivation, accelerating the recovery from inactivation, shifting the steady-state inactivation curve to more positive potentials and activation curve to more negative potentials (An et al., 2000; Beck et al., 2002).

2.6.3 KChIP1b is special – Aim of study

KChIP1b is a special KChIP1 splice variant that was first identified and cloned from mouse brain by Van Hoorick and coworkers in 2003 (Van Hoorick et al., 2003). It contains an additional 11 amino acids (highly aromatic; Figure 5.1), which was a formerly unrecognized

exon in the large intron between exons 1 and 2. The originally identified, shorter isoform was subsequently renamed KChIP1a. Different from other KChIP splice variants, KChIP1b has been reported to induce a second, extremely slow recovery component, which results in slowing recovery from inactivation, when co-expressed by transient cDNA transfection in a stable Kv4.2-expressing cell-line, while the recovery process behaved monoexponentially in the case of Kv4.2 alone or in the presence of KChIP1a. However, the mechanism underlying the special biphasic recovery kinetics induced by KChIP1b still remains unknown.

On this basis, in order to answer whether the special KChIP1b feature of slowing recovery from inactivation, previously reported for binary Kv4.2 + KChIP1b channels, exhibits a more general applicability, the aim of the present study was to investigate modulation of Kv4 channel subtypes by KChIP1 splice variants (KChIP1a and KChIP1b) in binary and ternary configurations with DPP in cRNA-injected *Xenopus laevis* oocytes and mechanism of KChIP1b-mediated recovery kinetics. Different experimental approaches were chosen for this purpose:

1) A detailed analysis of the modulation of Kv4.2 channels by KChIP1a and KChIP1b were first studied in both binary (Kv4 + KChIP1) and ternary (Kv4 + DPP + KChIP1) channel configurations in the *Xenopus* oocyte with two-electrode voltage clamp. 2) Modulation of other Kv4 channel subtypes (Kv4.1, Kv4.3S and Kv4.3L) by KChIP1a and KChIP1b was further investigated. 3) Mechanism of KChIP1b-mediated recovery kinetics was studied by investigating the specificities of KChIP1b-mediated recovery kinetics in the ternary (Kv4.2 + DPP + 1b) configuration using different pulse protocols; investigating the involvement of N-type inactivation using Kv4.2 N-terminal deletion mutant; investigating the involvement of P/C-type inactivation using elevated external K^+ or TEA concentration; investigating the relationship between closed-state inactivation and KChIP1b-associated P/C-type inactivation features using two Kv4.2 mutants located in the distal S6 segment from a previous alanine mutagenesis scan (Barghaan and Bähring, 2009).

3. Material and methods

3.1 Clones and vectors

The human clones of all Kv4 channel subtypes: Kv4.1, Kv4.2 and two splice variants of Kv4.3 (Kv4.3S, short splice variant; Kv4.3L, long splice variant) (Isbrandt et al., 2000), were used in this study. Kv4.3L (Abbott, 2017) was a kind gift from Geoffrey Abbott (Department of Physiology and Biophysics, University of California, Irvine, USA). The β-subunits of Kv4 channel subtypes: the short splice variant of KChIP1 (KChIP1a), the long splice variant of KChIP1 (KChIP1b), and the short splice variant of DPP6 (DPP6S) were used in this study. KChIP1a was kindly provided by Dirk Isbrandt (Center for Molecular Medicine, University of Cologne, Germany) and DPP6S was provided by Nicole Schmitt (Department of Biomedical Sciences, Faculty of Health and Medical Sciences, Copenhagen, Denmark). In order to generate KChIP1b, a 33 bp fragment was inserted into the KChIP1a coding region by overlap PCR with appropriate primers (fwd: accagtatcagagagaTAAGATTGAAGATGAGCTGGAG; rev: aataccaccaggcgatgTCTTTCGAGGGTCGCCTT) in a back-to-back orientation, using the Q5 Site Directed Mutagenesis Kit (New England Biolabs), which was performed by Georgios Tachtsidis (University Hamburg-Eppendorf). An N-terminal deletion mutant of Kv4.2, Kv4.2 Δ10 (Bähring et al., 2001b), in which 10 amino acids of the proximal N-terminus had been deleted, was used. An alanine-scanning mutagenesis in the distal part of S6 had been performed in previous study (Barghaan and Bähring, 2009). Two mutants located in the distal part of S6 of Kv4.2, either leucine at position 400 or asparagine at position 408, were replaced by alanine (Kv4.2 L400A and Kv4.2 N408A, respectively), were selected. All cDNAs used in this study were inserted into the multiple cloning site of the RNA transcription vector pGEM-HE.

3.2 In vitro synthesis of cRNA

The cDNA used in this work, as well as transformation of bacteria (JM109 *E.coli* cells), plasmid isolation (QIAprep Spin Miniprep Kit, Germany) were provided by Anett Hasse (University Hamburg-Eppendorf), as previously described (Barghaan and Bähring, 2009; Wollberg and Bähring, 2016). Plasmid DNA in pGEM-HE vector was transcribed into RNA as following.

1) Digestion and linearization of plasmid DNA

2 µg of template DNA (10µl of solution with a concentration of 0.2 µg/µl) was incubated

with 5µL FD-Puffer, 1.5 µL Enzyme (*Not* I/*Sal* I; New England Biolabs), 33.5 µL DEPC-H_2O in a total volume of 50 µL at 37 °C overnight.

2) Agarose electrophoresis

1% agarose gel was prepared to confirm the linearization of template DNA. 0.5 g agarose powder and 50 mL 1 × TBE – buffer was mixed and heated in the microwave for 2-3 minutes until the solution became clear. After the mixture had cooled slightly, 3 µL pecGREEN was added, mixed, and then filled into the gel form. Comb was carefully inserted into the gel. The solidified gel was placed in an electrophoresis chamber with covered 1 × TBE – buffer. 5 µL digested probe from the reaction mixture of DNA was added with 1 µL Loading-Dye 6x into the pocket of gel. 5 µL 1kb DNA ladder (ThermoFischer) was used as a marker. The gel was run at 110 V, 80 mA and 3-6 W for 50 minutes to separate the DNA fragments by size. After electrophoresis, the DNA bands were examined under the UV light TI1 (Biometra, Göttingen), with a wavelength of 312 nm.

3) cDNA precipitation

DNA precipitation was performed for purification. 45 µL digested probe DNA was mixed with 5 µL Na-acetate (pH 5.2), 2.5 µL 0.5M EDTA and 125 µL cold 100% Et-OH absolute. The mixture was incubated at -20 °C for 30 minutes. Afterwards, the reaction mixture was centrifuged with the speed of 14000 RPM, at 4 °C for 20 minutes. The supernatant was carefully pipetted out without disturbing the DNA pellet. 1 mL 70% Et-OH absolute was added into the tube, vortexed briefly and centrifuged with the speed of 14000 RPM, at 4 °C for 10 minutes. The supernatant was again removed and then the DNA precipitate was dried using a vacuum concentrator at room temperature for 10-15 minutes.

4) Capping (T7 reaction)

RiboMAX™ Large Scale T7 Production Kit (Promega, Walldorf) was used for cRNA synthesis. 17 µL DEPC-H_2O was first applied in the previous tube with DNA precipitation. 15 µL rNTP, 10 µL T7-Buffer, 5 µL T7-Enzyme-mix and 3.75 µL Ribo Cap-Analog (40 mM) were mixed with the DNA probe. The total volume for the T7 reaction was 50 µL. The mixture was incubated at 37 °C for 3 hours. After the incubation, 4 µL RQ1-DNAse was added and them incubated at 37 °C for 15 minutes in order to remove residual DNA contamination. 46 µL DEPC-H_2O was added for a total volume of 100 µL.

5) RNA precipitation

All the work in this step was performed on the ice and under the hood. The synthesized RNA was extracted and purified by phenol-chloroform extraction and ethanol precipitation. 100

µL phenol-chloroform-isoamyl-alcohol was added into the 100 µL RNA probe. The mixture was vortexed for 30 seconds, and then centrifuged with a speed of 14000 RPM, at 4 °C for 2 minutes. The supernatant was carefully transferred into a new RNase-Free tube and another 100 µL phenol-chloroform-isoamyl-alcohol was added. Then the vortex and centrifugation were repeated as previous step. After the top phase was transferred into a new RNase-Free tube, 100 µL Chloroform was added. The solution was vortexed for 30 seconds, and then centrifuged with the speed of 14000 RPM, at 4 °C for 2 minutes. The top layer was again transferred into a new RNase-Free tube, and 10 µL Natrium-Acetate, 250 µL 100 % cold Et-OH were added. The mixed solution was incubated on ice for 5 minutes to precipitate the RNA. After incubation, the mixture was centrifuged with the speed of 14000 RPM, at 4 °C for 10 minutes. After the upper layer was removed, 1 mL 70 % cold Et-OH was added. The solution was again centrifuged of a speed of 14000 RPM, at 4 °C for 5 minutes. The supernatant was discarded and then the RNA precipitate was dried using a vacuum concentrator at room temperature for 10-15 minutes until all visible liquid had evaporated. Finally, 100 µL of DEPC-H_2O were added into the tube and mixed until the pellet dissolved.

6) RNA quantification

The RNA concentration was measured with the IMPLEN NanoDrop spectrophotometer (Implen, Munich, German).

7) RNA quality control (agarose electrophoresis)

1% agarose gel was prepared as previously described. 5 µL of RNA probe was mixed with 5 µL 2 × RNA Loading Dye and incubated at 70 °C for 10 minutes. 3-5 µL RNA-Ladder RiboRuler high-range (ThermoFischer) was used as a marker. The gel was conducted at 110 V, 80 mA and 3-6 W for 40-50 minutes. After electrophoresis, the DNA bands were examined under the UV light TI1 (Biometra, Göttingen), with a wavelength of 312 nm.

3.3 Heterologous channel expression

Xenopus laevis oocytes can be induced to express ion currents on the surface of plasma membrane by injecting cRNA of ion channel protein into the oocytes (Gurdon et al., 1971; Weber, 1999). *Xenopus laevis* oocytes are huge cells (1.0 to 1.2 mm in diameter) and can be easily injected, manipulated and used for electrophysiological measurements (Weber, 1999). The endogenous channels and receptors are expressed at low levels on its membrane. The amount of RNA injected can be precisely adjusted, so that the levels of expressed protein can be controlled. Therefore, oocytes of *Xenopus laevis* serve as a standard heterologous

expression system for ion channels study (Baumgartner et al., 1999; Dascal, 2000), which enables the expression of membrane proteins either in isolation or in combination with other proteins (Dascal, 1987).

3.3.1 *Xenopus laevis* oocytes preparation

Fresh oocytes were obtained from female *Xenopus laevis* frogs. Frog surgeries were performed by Professor Robert Bähring. 1.2 g Ethyl 3-aminobenzoate methanesulfonate (Tricain, MS-222, Sigma-Aldrich) was dissolved together with 25 mL of 0.5 M $H_2Na_2PO_4$ buffer solution in 1 L tap water for anesthesia (approximately 10-20 minutes at room temperature). After anesthetized, a 1 cm long incision in the lower abdominal area of a frog was made. Part of the ovary lobes was gently removed and cut from the abdominal cavity. Fresh oocytes were transferred into a tube with 50 mL OR1 + 50 µg/mL gentamicin solution for transport. The fascia and abdominal wall of the frog were sutured and the frog was put back in the fresh tap water to recover.

To remove the follicular cell layer, the lobes of oocytes were manually pulled apart into smaller cluster of 10-20 cells. The tissue was digested in Ca^{2+}- free oocyte Ringer's solution (OR2 solution) with 1.3 mg/mL Collagenase II (Sigma, USA) at room temperature on a horizontal shaker (RM5, Assistant, Germany) for 4-5 hours. When the oocytes were completely isolated, the supernatant was carefully discarded and the oocytes are washed with OR1 at least 4-5 times to remove the follicular layer and blood. After washing procedure, the oocytes were transferred into a 10 cm cell culture dish with OR1 + 50 µg/mL gentamicin solution. Oocytes were incubated overnight at 16 °C until cRNA injection. Composition of *Xenopus* oocyte solutions can be found in Table 3.1. *Xenopus* oocyte solutions were stored at 4 °C. Usually 1 L *Xenopus* oocyte solutions were prepared every time, using ultrapure water in a volumetric flask. Stir was used to make sure all the reagents were completely dissolved.

Table 3.1 Solutions for *Xenopus* oocytes

Name	Composition
OR1	75 mM NaCl, 5 mM Na pyruvate, 2 mM KCl, 2 mM $CaCl_2$, 1 mM $MgCl_2$, 5 mM HEPES, pH 7.5 with NaOH/HCl, with 50µg/mL Gentamicin, sterile filtered
OR2	82.5 mM NaCl, 2 mM KCl, 1 mM $MgCl_2$, 5 mM HEPES, pH 7.5 with NaOH/HCl, sterile filtered

3.3.2 cRNA injection

1) Preparation of injection needles

Glass capillary (Injector, Glass Replacement 3.5 nL 4878, ONE, 08-J S/N) were heated and pulled by a puller (L/M-3P-A, List-Medical) into fine needles. The tips of the needles were carefully broken under the microscope to make the injection tip around 20-40 µm in diameter. Then the needles were placed in a metal box and backed at +200 °C together with fine glass capillaries for 2 hours in order to eliminate any RNAse and other contaminants.

2) Injection procedure

Workplace and equipment were treated with RNase Blocker before injection. Well-conditioned, non-folliculated V-VI stage oocytes were selected and placed in a culture dish with OR2 solution. The injection needle was first filled with oil, inserted under the microscope to the injector and then the oil was emptied forward. A cRNAs solution aliquot was taken from the -20 °C freezer, centrifuged and transferred to the injection needle using a fine glass capillary under the microscope. 12-15 oocytes were placed in a row in the injection chamber with OR2 solution each time, which were completely covered by the solution but did not float. The tip of the glass needle was positioned close to the surface of the oocytes and then they were impaled by a Nanoliter 2000 Microinjector (WPI, Freidberg, Germany). After each injection, the needle was withdrawn and turned to next oocyte. Injected oocytes were stored in 5 mL OR1 solution with 50 µg/mL gentamicin in 35 mm cell culture dishes, and incubated at 16 °C for 1-10 days until used for recordings.

3) Volume and concentration of cRNA

In order to study different aspects of Kv4 channel modulation by the two KChIP splice variants 1a and 1b, we expressed Kv4.x channels (Kv4.x = Kv4.1, Kv4.2, Kv4.3S or Kv4.3L) in *Xenopus* oocytes in the following configurations (Figure 3.1): (1) Kv4.x α-subunit alone (homotetrameric control): each oocyte was injected with either 0.8 ng of Kv4.x cRNA in 23 nL, or 1.7 or 5 ng in 50 nL. (2) Kv4.x α-subunit together with either KChIP1a or KChIP1b (referred to as 1a and 1b in figures and texts; Kv4.x + KChIP1x; binary configuration): To examine KChIP1 effect in a binary configuration, each oocyte was injected with 1.7 ng Kv4.x + 5, 10, or 20 ng of 1a or 1b in 50 nL, or with 0.8 ng Kv4.x + 5 ng of 1a or 1b in 23 nL. (3) Kv4.x α-subunit together with DPP6-S (referred to as DPP in figures and texts; Kv4.x + DPP): As a control for KChIP1 co-expression experiments in the presence of DPP, each oocyte was injected with 1.7 ng Kv4.x + 5 ng DPP in 50 nL, or with 0.8 ng Kv4.x + 5 ng DPP in 23 nL. (4) Kv4.x α-subunit together with DPP and either 1a or 1b (Kv4.x + DPP +

KChIP1x; ternary configuration): To examine KChIP1 effect in a ternary configuration with DPP, each oocyte was injected with 1.7 ng Kv4.x + 5 ng DPP + 10 ng of 1a or 1b in 50 nL, or with 0.8 ng Kv4.x + 5 ng DPP + 2.5 ng of 1a or 1b in 23 nL. Oocytes were used for electrophysiology recordings 1-10 days after cRNA injection.

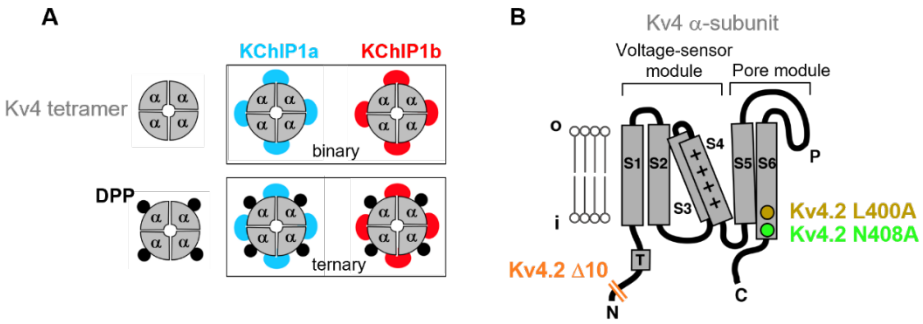

Figure 3.1 Kv4 channel subunit composition and structure. Cartoons depict the subunit assembly of Kv4 channels and the molecular structure of a Kv4 α-subunit. A: Tetrameric assembly of Kv4 α-subunits (grey quadrants) in the absence (upper row) and presence of DPPs (black circles, lower row); KChIP1 splice variants 1a (blue) or 1b (red) co-assembled with Kv4 channels in a binary configuration (upper box) or with Kv4 + DPP channels in a ternary configuration (lower box). B: Modification of selected Kv4.2 mutants: a ten amino acid N-terminal deletion construct (Kv4.2 Δ 10) and two constructs with amino acid substitutions in S6 (Kv4.2 L400A and N408A) were used in the present study.

3.4 Electrophysiology

3.4.1 Two-electrode voltage clamp

Measurements in this study were performed using the two-electrode voltage clamp (TEVC) technique. The electrophysiological experiments were carried out at room temperature (20 to 25 °C). In contrast to the original method applied by Hodgkin and Huxley (Hodgkin et al., 1952), modern TEVC use two glass electrodes: voltage electrode and current electrode. In this method, the membrane voltage is artificially set to a desired potential, called command voltage ($V_{command}$), which may be different from the resting potential. The membrane potential (V_m) is monitored by a voltage electrode. When there is a difference between $V_{command}$ and V_m, current electrode injects currents into the cell to maintain the membrane potential at the desired value through a feedback amplifier. The injected current amplitude, although opposite in sign, is equal to the membrane current and it is measured as the total membrane current (I_m) (Halliwell et al., 1999). The properties of ion channels can be studied by recording the membrane currents, using various recording protocols, different extracellular recording solutions and applying chemicals. Figure 3.2 illustrates a simplified setup of a typical TEVC recording from a *Xenopus laevis* oocyte, modified from Nowotny

and Levi (2013).

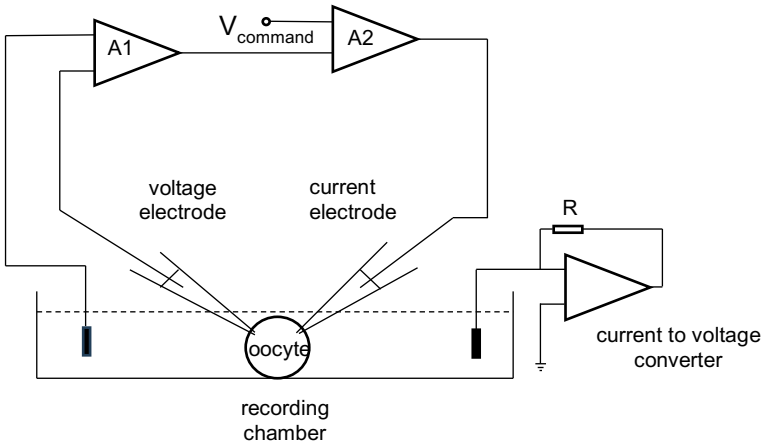

Figure 3.2 Illustration of a conventional TEVC setup from a *Xenopus* laevis oocyte. The *Xenopus* oocyte is placed in the middle of the recording chamber certainly superfused with recording solution. Two electrodes, one for voltage electrode and the other for current electrode, are inserted into an oocyte via glass capillaries filled with 3 M KCl. V_m is measured by the voltage electrode connecting to a high input impedance amplifier (A1). The output of A1, which is approximately equal to V_m, is passed to a clamping amplifier (A2). A2 is a high gain differential amplifier and the input of A2 is compared with $V_{command}$. If the two potentials are different, A2 produces current, which is injected into the oocyte by the current electrode, in order to bring the difference between commend voltage and membrane potential to zero. The injected current is calculated by measuring the potential across the resistance R via a current to voltage converter, as total membrane current (I_m). Reference electrodes are placed in the recording solution, one is connected with A1 and another one is connected to current to voltage converter.

3.4.2 Experimental set-up

1) Preparation of electrodes

4-5 cm long and 0.25 mm thick straight silver wires were used in the voltage electrode and the current electrode. Silver wires were chlorided using an automatic chloride (ACL-01, npi electronic GmbH). For this purpose, silver wires connected to the automatic chloride were immersed into 3 M KCl solution with less the 1cm end of each wire left in the air. After the immersed part was completely blackened, Ag/AgCl wires were coated. Recording glass pipettes (GB150TF-8P, Science Products, Hofheim) were pulled into two symmetric glass electrodes by a vertical Puller (L/M-3P-A List-Medical). The needle tips were slightly broken under the microscope in order to reduce its resistance in the range of 0.1-0.5 MΩ and later filled with 3 M KCl. A filled glass needle was placed onto the electrode holder with Ag/AgCl wire pre-installed, which were later installed on a micromanipulator (Märzhäuser, Wetzlar).

2) Set-up of the recording system

The recording apparatus for TEVC was placed on a metal plate on the table, with two

electrode holders attached to the mechanical micromanipulators. The angle between the electrode and the plane of the table was around 45°. A binocular microscope (Stemi DV4spot, Zeiss, Jena) was used for the optical monitoring and placed above the recording chamber, which was located in the center between two-electrodes. Superfusion of the oocytes with the recording solution was performed using a gravity-driven perfusion system, and a vacuum pump was used for aspiration. The extracellular solutions, used for measurement, if not specially noted, was standard physiological extracellular solution (ND 96). 98 mM-K^+ bath solution (high K^+ solution) and 98 mM-TEA bath solution (high TEA solution) were also utilized. An injected oocyte was picked and transferred from the culture dish to the cavity of the recording chamber with recording solution. The tips of voltage and current electrodes were impaled into the oocyte membrane, which was verified by monitoring the voltage. Resting membrane potential was usually between −20 and −50 mV. All recordings used -80 mV as holding potential. Recording signals were amplified by using a Turbo tec-03x amplifier (NPI, Tamm) and digitalized by an AD/DA converter (IntruTECH LIH 8 + 8, HEKA, Lambrecht) with a sampling frequency of 1 - 4 kHz. The outputs of the amplifier were monitored on a computer.

3.4.3 Experimental solutions

The measurements were carried out under constant flow of extracellular solutions. The composition of the extracellular solutions can be found in Table 3.2

Table 3.2 Recording solutions for electrophysiological measurement.

Name	Composition
ND96	96 mM NaCl, 2 mM KCl, lmM $CaCl_2$, l mM $MgCl_2$, 5 mM HEPES, pH 7.4 with NaOH/HCl, sterile filtered
high K^+ solution	98 mM KCl, lmM $CaCl_2$, l mM $MgCl_2$, 5 mM HEPES, pH 7.4 with NaOH/HCl, sterile filtered
high TEA solution	98 Mm TEA, lmM $CaCl_2$, l mM $MgCl_2$, 5 mM HEPES, pH 7.4 with NaOH/HCl, sterile filtered

For the high K^+ and high TEA bath solution, all NaCl was substituted with KCl or TEA.

3.4.4 Recording pulse protocols

The Software Patchmaster (v.2x9l, HEKA, Lambrecht) was used to define the pulse

protocols, control the amplifier and record the data.

Test pulse protocol

Test pulse protocols (Figure 3.3) were performed to study the peak current amplitudes and macroscopic inactivation (i.e., current decay). It consists of two similar recording protocols. The first test pulse: after a pre-pulse at -100 mV for 2 s, a depolarizing pulse at +40 mV (2.5 s) was recorded, which activated all the Kv4 channels. The second test pulse was similar, but with a pre-pulse at -35 mV for 2 s and then a depolarizing step to +40 mV for 2.5 s). The -35 mV pre-pulse inactivated all the Kv4 channels, and only endogenous currents and leak currents were recorded. In order to eliminate the endogenous currents and leak currents, the current recorded in the second test pulse was subtracted from the first pulse current.

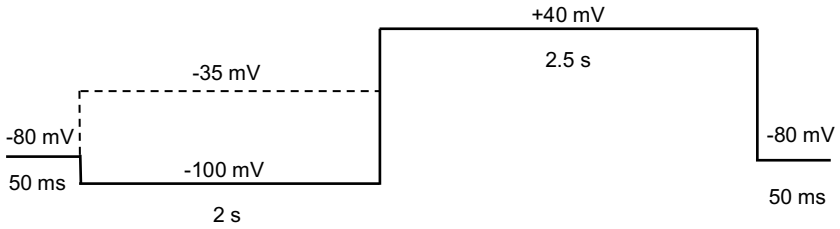

Figure 3.3 Test pulse protocol. First, starting from a holding potential of -80 mV, a pre-pulse at -100 mV for 2 s was applied, followed by a depolarizing pulse to +40 mV for 2.5 s. The second test pulse was performed with a pre-pulse at -35 mV for 2 s in order to subtract the endogenous currents and leak currents.

Recovery from inactivation

The first recovery protocol is a standard double-pulse protocol (Figure 3.4), in which inactivation is possible via the open state (recovery from high-voltage inactivation).

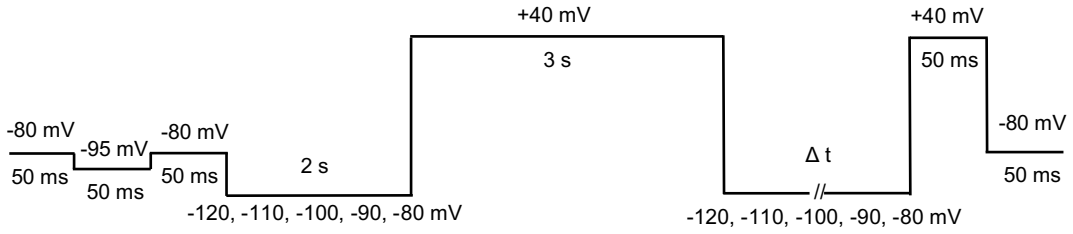

Figure 3.4 Pulse protocol of recovery from inactivation. After a brief pulse from a holding potential to -95 mV, at which contains only leak currents for test and control currents subtraction, a hyperpolarizing pre-pulse at -80 mV for 2 s was applied to make sure most of the channels were at the closed state. Then, the first depolarizing pulse to +40 mV for 3 s was recorded as control current ($I_{control}$), which was used to activate and inactivate almost all the channels in each run. Afterwards, a hyperpolarizing step was applied to -80 mV (recovery potential) with varying interpulse duration (Δ t), ranging from 0ms to 20480 ms, which was incremented by a factor of 2, to allow the channels to recover, and a second pulse to +40 mV for 50 ms was performed to determine the availability of the channels (I_{test}). Recovery potentials of -120, -110, -100, and -90 mV were also used to study the voltage dependence of recovery from high-voltage inactivation.

A second recovery protocol was applied, in which inactivation was induced by a pre-pulse below the activation threshold, so that inactivation can only occur from closed states (Figure 3.5).

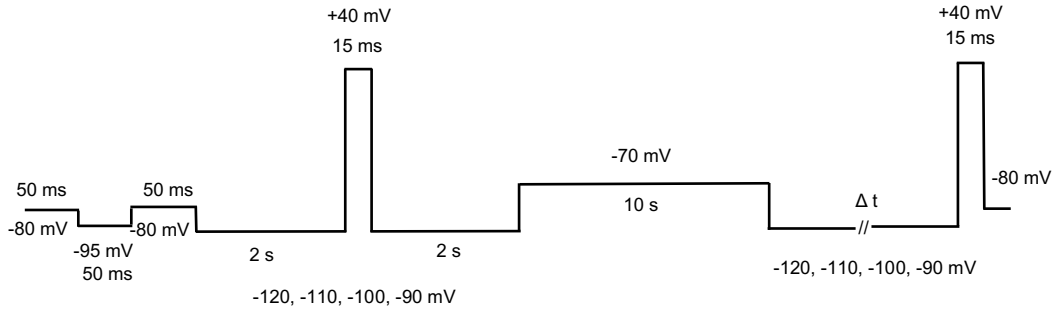

Figure 3.5 Pulse protocol for recovery from low-voltage inactivation. Similar to standard double-pulse protocol, after a brief pulse from a holding potential to -95 mV, a hyperpolarizing pre-pulse to -100 mV for 2 s was applied. The control depolarizing pulse at +40 mV for 15ms was recorded as control current ($I_{control}$). Then, a hyperpolarizing pulse returned to recovery potential for 2 s to make sure most of the channels were closed. The closed-state inactivation was induced with a depolarizing pulse to -70 mV for 10 s. Afterwards, a hyperpolarizing step was applied to -100 mV (recovery potential) with varying interpulse duration (Δ t), ranging from 0ms to 20480 ms, which was incremented by a factor of 2, allowing the channel to recover. The test pulse at +40 mV for 15 ms was recorded as test current (I_{test}) to determine the availability of the channels. Recovery potential of -120, -110, -90 mV were used to study the voltage dependence of recovery from low-voltage inactivation.

The third recovery protocol was performed to investigate recovery from inactivation with different inactivating voltages (Figure 3.6).

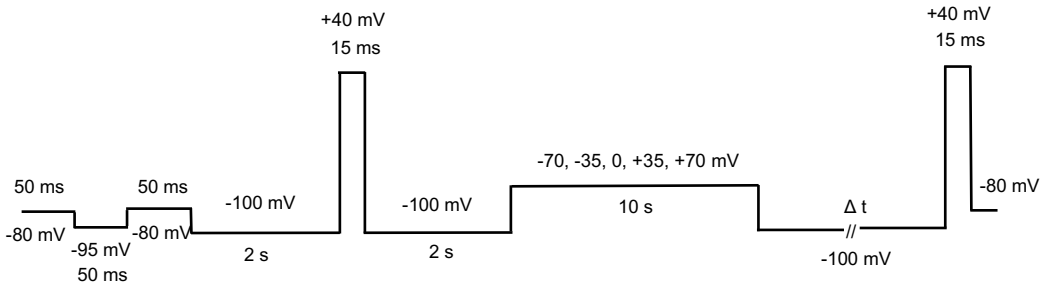

Figure 3.6 Pulse protocol for recovery from inactivation with different inactivating voltages. After a brief pulse from a holding potential to -95 mV, a hyperpolarizing pre-pulse to -100 mV (recovery potential) for 2 s was applied, the control depolarizing pulse at +40 mV for 15 ms was recorded as control current ($I_{control}$). Then, a hyperpolarizing pulse returned to recovery potential for 2 s. A depolarizing pulse at -70, -35, 0, +35 or +70 mV for 10 s was used to induce inactivation. Afterwards, a hyperpolarizing step was applied to -100 mV with varying interpulse duration (Δ t), ranging from 0ms to 20480 ms, which was incremented by a factor of 2. The test pulse at +40 mV for 15 ms was recorded as test current (I_{test}) to check the availability of the channels.

The fourth recovery protocol was performed to investigate recovery from inactivation with different inactivating pulse durations (Figure 3.7).

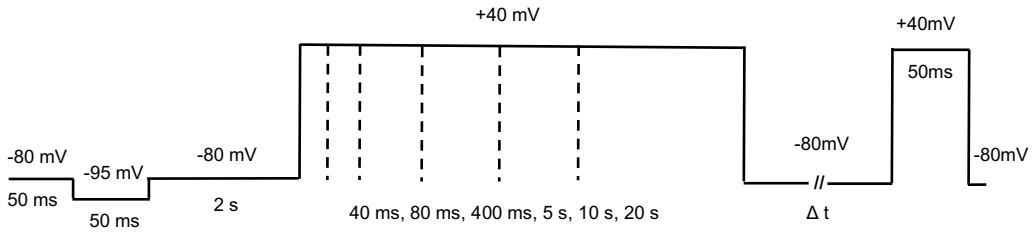

Figure 3.7 Pulse protocol for recovery from inactivation with different inactivating pulse durations. After a brief pulse from a holding potential to -95 mV, a hyperpolarizing pre-pulse to -80 mV for 2 s was applied to make sure most of the channels were in the closed state. Then, the first depolarizing pulse to +40mV for 40 ms, 80 ms, 400 ms, 5 s, l0 s or 20 s was recorded as control current ($I_{control}$), which was used to activate and inactivate part or all the channels in each run. Afterwards, a hyperpolarizing step was applied to -80 mV (recovery potential) with varying interpulse duration (Δ t), ranging from 0ms to 20480 ms, which was incremented by a factor of 2, and a second pulse to +40 mV for 50ms was performed to determine the availability of the channels (I_{test}).

Voltage dependence of steady-state activation

In order to investigate the steady-state inactivation, a double-pulses protocol was used as shown in Figure 3.8.

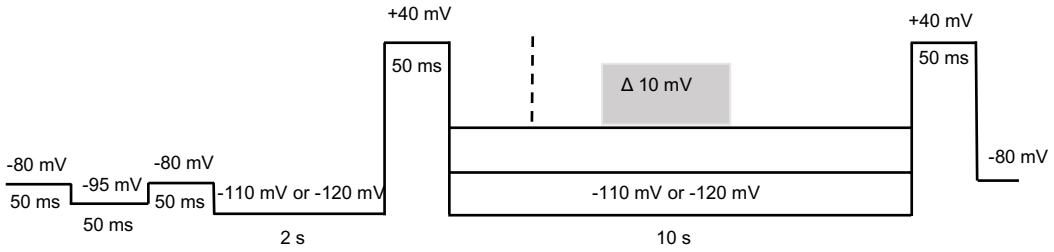

Figure 3.8 Pulse protocol for steady-state inactivation. After a brief pulse from holding potential to -95 mV, a prepulse at -l10 mV (in the presence of la) or -l20 mV (in the presence of lb) lasting for 2 s was applied. A depolarization step to +40 mV was recorded as a control current ($I_{control}$). Then different voltages starting from -l10 mV (in the presence of la) or -l20 mV (in the presence of lb) to +20 mV, increasing by +10 mV each repeat, were applied for 10 s. Afterwards, the test pulse at +40 mV was recorded as a test current (I_{test}) in order to determine how many channels still can be activated.

Voltage dependence of activation

In order to study the voltage dependence of activation, an *I-V* protocol was performed as shown in Figure 3.9.

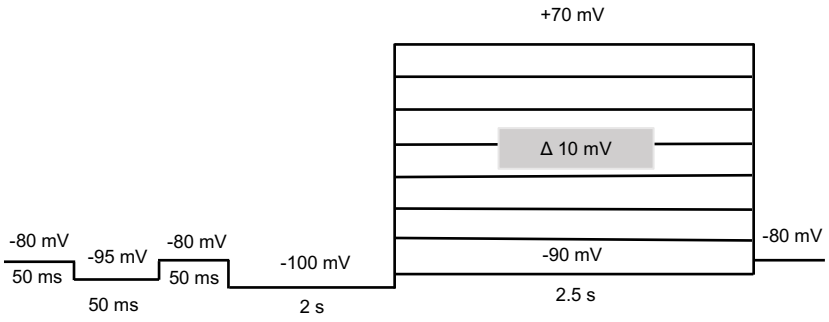

Figure 3.9 Pulse protocol for voltage dependence of activation (*I-V* protocol). After a brief pulse from holding potential to -95 mV, a pre-pulse at -100 mV was applied for 2 s. Then, the oocytes were depolarized to different voltages, from -90 mV to +70 mV for 2.5 s, in steps of 10 mV each sweep, in order to determine at which voltage, the channel starts to activate. After depolarization, the cells were hyperpolarized to holding potential.

3.5 Data collection and analysis

Fitmaster (v.2x91, HEKA, Lambrecht, Germany) was used to evaluate the current recordings. Current amplitudes and time constants of macroscopic inactivation could be determined by the software. The data processed with Fitmaster were further analysed using Kaleidagraph (v.5, Synergy Software, USA), to determine the kinetics of recovery from inactivation, the voltage dependence of steady-state inactivation and activation, Kaleidagraph was also used to perform statistic tests.

For consistency, current amplitudes were always compared between groups at a membrane potential of +40 mV when the same amount of Kv4.x cRNA was injected. Individual data points like current amplitudes, fit results and kinetic parameters are given as mean ± SD (standard deviation) in summary graphs. Normalized pooled data for recovery from inactivation, steady-state inaction and voltage dependence of activation are shown as mean ± SEM (standard error). The voltage dependences of recovery kinetics were defined by the apparent charge q_{app}, a fraction of the elementary charge q_e, dependent on the Boltzmann constant k_B and the absolute temperature T ($k_B\,T/q_e = RT/F = 25.28$ mV at room temperature) (Barghaan et al., 2008). To assess statistical significance, one-way analysis of variance (ANOVA) with Dunnett's post hoc test was used for multiple comparisons, and unpaired Student's *t*-tests were performed to compare two different groups. Paired Student's *t*-tests were performed for comparison of the time constants of recovery from inactivation in normal ND96 solution and high K^+ or high TEA solution. The difference was reported to be significant if $p<0.05$ and highly significant if $p<0.0001$.

Peak current amplitude

The peak current amplitudes at +40 mV (I_{+40}) were determined after leak subtraction. The leak current at +40 mV ($I_{leak\ (+40)}$) were calculated by using mean current from -95 mV (potassium reversal potential, only leak current):

$$I_{+40} = I - I_{leak(+40)}$$

$$I_{leak(+40)} = \frac{I_{-95}}{-95} \times 40$$

I: current amplitudes recorded at +40mV; I_{+40}: peak current amplitudes at +40 mV

$I_{leak(+40)}$: leak current at +40mV; I_{-95}: mean current from -95 mV

Macroscopic inactivation

The kinetics of macroscopic inactivation of Kv4 channels, in the absence or presence of auxiliary β-subunits were best described with a triple-exponential function by fitting the current decay:

$$I = A_0 + A_1 \cdot e^{-\frac{t}{\tau_1}} + A_2 \cdot e^{-\frac{t}{\tau_2}} + A_3 \cdot e^{-\frac{t}{\tau_3}}$$

The percentage of relative amplitudes was calculated from obtained data:

$$\%\tau_x = A_x / (A_1 + A_2 + A_3) \cdot 100$$

$\%\tau_x$**:** the percentage of relative amplitudes; A_x: amplitudes of time constant

In order to study the effect of high K^+/TEA (elevated external K^+/TEA) on the macroscopic inactivation, the current decay was fitted with a double-exponential function:

$$I = A_0 + A_1 \cdot e^{-\frac{t}{\tau_1}} + A_2 \cdot e^{-\frac{t}{\tau_2}}$$

I: current; τ_1, τ_2, τ_3: time constants; A_0: offset amplitude; A_1, A_2, A_3**:** amplitudes of the three-time constants; t: time

Recovery from inactivation

The peak current amplitudes of test pulse (I_{test}) and control pulse ($I_{control}$) were leak-subtracted by using the mean current from -95 mV and calculated as described. The normalized data ($I_{test}/I_{control}$) were plotted against the interpulse interval duration on a log-scale. The recovery data could be exponentially fitted in six different ways:

Single exponential function without offset:

$$\frac{I_{test}}{I_{control}} = 1 - e^{\frac{-t}{\tau_{rec}}}$$

Single exponential function with an offset:

$$\frac{I_{test}}{I_{control}} = (1 - A_0) \cdot \left(1 - e^{\frac{-t}{\tau_{rec}}}\right) + A_0$$

Double exponential function without offset:

$$\frac{I_{test}}{I_{control}} = (1 - A_2) \cdot \left(1 - e^{\frac{-t}{\tau_1}}\right) + A_2 \cdot \left(1 - e^{\frac{-t}{\tau_2}}\right)$$

Double exponential function with an offset:

$$\frac{I_{test}}{I_{control}} = (1 - A_0 - A_2) \cdot \left(1 - e^{\frac{-t}{\tau_1}}\right) + A_2 \cdot \left(1 - e^{\frac{-t}{\tau_2}}\right) + A_0$$

Triple exponential function without offset:

$$\frac{I_{test}}{I_{control}} = (1 - A_2 - A_3) \cdot \left(1 - e^{\frac{-t}{\tau_1}}\right) + A_2 \cdot \left(1 - e^{\frac{-t}{\tau_2}}\right) + A_3 \cdot \left(1 - e^{\frac{-t}{\tau_3}}\right)$$

Triple exponential function with an offset:

$$\frac{I_{test}}{I_{control}} = (1 - A_0 - A_2 - A_3) \cdot \left(1 - e^{\frac{-t}{\tau_1}}\right) + A_2 \cdot \left(1 - e^{\frac{-t}{\tau_2}}\right) + A_3 \cdot \left(1 - e^{\frac{-t}{\tau_3}}\right) + A_0$$

t: time (interpulse duration; see Figure 3.5-3.7); τ_x: time constant; A_0: offset amplitude; A_2, A_3: relative amplitude of τ_2 and τ_3; relative amplitude of τ_1 (A_1) was calculated: $A_1 = 1 - A_2$ or $A_1 = 1 - A_2 - A_3$; the percentage of relative amplitudes was calculated from the obtained data:

$$\%\tau_x = A_x / (A_1 + A_2) \cdot 100 \text{ or } \%\tau_x = A_x / (A_1 + A_2 + A_3) \cdot 100$$

A_x: amplitudes of time constant

Voltage dependence of activation

The voltage dependences of activation were calculated by measuring the maximum current amplitudes (I_{max}) in the *I-V* activation protocol and convert into the conductance (G):

$$G = \frac{I_{max}}{V_m - E_K}$$

V_m: respective membrane potential; E_K: reversal potential

The conductance values for the conductivities were normalized to respective maximum (G_{max}) and plotted against the membrane potential (V_m). A 4th order Boltzmann equation was used to fit the *G-V* data:

$$\frac{G}{G_{max}} = \left(\frac{1}{1 + e^{\left(\frac{V_m - V'}{s}\right)}}\right)^4$$

V': Voltage at 6.5% of maximum activation; *s*: slope factor of the *G-V* curve; the halfmaximal voltage of the *G-V* curve ($V_{1/2,act}$) was determined manually with Kaleidagraph (v.5, Synergy

Software, USA).

Voltage dependence of steady-state inactivation

The peak current amplitudes of test pulse (I_{test}) and control pulse ($I_{control}$) were leak-subtracted by using the mean current from -95 mV and calculated as described. The normalized data ($I_{test}/I_{control}$) were plotted against the voltage of the prepulse (V_m). A single Boltzmann function was used to fit the data points:

$$\frac{I_{test}}{I_{control}} = \frac{(1 - A_0)}{\left(1 + e^{\frac{V_m - V_{1/2,inact}}{s}}\right)} + A_0$$

V_m: membrane potential; A_0: offset amplitude; $V_{1/2,inact}$: voltage of halfmaximal inactivation, indicating that at this potential, 50% of the channels are at the inactivated state; *s*: slope factor at $V_{1/2,inact}$.

4. Results

4.1 Modulation of Kv4.2 channels by KChIP1 splice variants in binary and ternary configurations studied in the *Xenopus* oocyte expression system

In this chapter, the effects of KChIP1 splice variants co-expression on the Kv4.2 channel subtype in the *Xenopus* oocyte expression system, such as functional expression (i.e., peak current amplitude), the kinetics of both macroscopic inactivation (i.e., current decay) and recovery from inactivation, as well as voltage dependence of activation and steady-state inactivation, will be first described, in order to complement previous data obtained with a stable Kv4.2-expressing cell-line transfected with KChIP1a and KChIP1b cDNA in the absence of DPP. Here, we investigated the modulation of Kv4.2 channels by KChIP1 splice variants not only in the absence of DPP (binary configuration) but also in the presence of DPP (ternary configuration).

4.1.1 Peak current amplitude

To investigate the effects of KChIP1a and KChIP1b (referred to as 1a and 1b in Chapter 4) on the functional expression of Kv4.2 channels, Kv4.2 channel cRNA (1.7 ng per oocyte) was first injected alone into *Xenopus* oocytes. Kv4.2-mediated A-type currents were recorded using TEVC in response to a depolarizing voltage step (Figure 4.1A). The mean peak current amplitude at +40 mV for Kv4.2 was 0.5 ± 0.3 μA (n = 18; Figure 4.1B). In the binary configuration, co-expression with either 1a or 1b cRNA (5, 10, 20 ng injected per oocyte) significantly increased peak current amplitude of Kv4.2 channels (Figure 4.1A and B). When 1a (10 ng per oocyte) was co-expressed with Kv4.2, the peak current amplitude was increased to 8.3 ± 4.1 μA (n = 37), significantly larger than that observed with the same amount of 1b (2.0 ± 1.3 μA, n = 47; $p<0.0001$), indicating that the effect of 1b on increasing the current amplitude was weaker compared to 1a. The difference between 1a and 1b co-expression regarding current enhancement was highly significant and persisted even if 5 ng or 20 ng of KChIP1 cRNA was injected, and no dose-dependent increase in Kv4.2 current amplitudes was observed with either 1a or 1b (Figure 4.1B; Table 4.1). The 1b-induced increase in Kv4.2 currents in our study is consistent with previous results in a stable Kv4.2-expressing cell-line (Van Hoorick et al, 2003). Based on these results, 1.7 ng Kv4.x + 10 ng KChIP1x were used for all subsequent co-expression experiments, unless otherwise stated.

To investigate the effects of 1a and 1b on the functional expression of Kv4.2 channels in the presence of DPP, 1.7 ng Kv4.2 was co-expressed with 5 ng DPP as the control group and

measurements were carried out on day1 (d1) and day2 (d2) after cRNA injection.

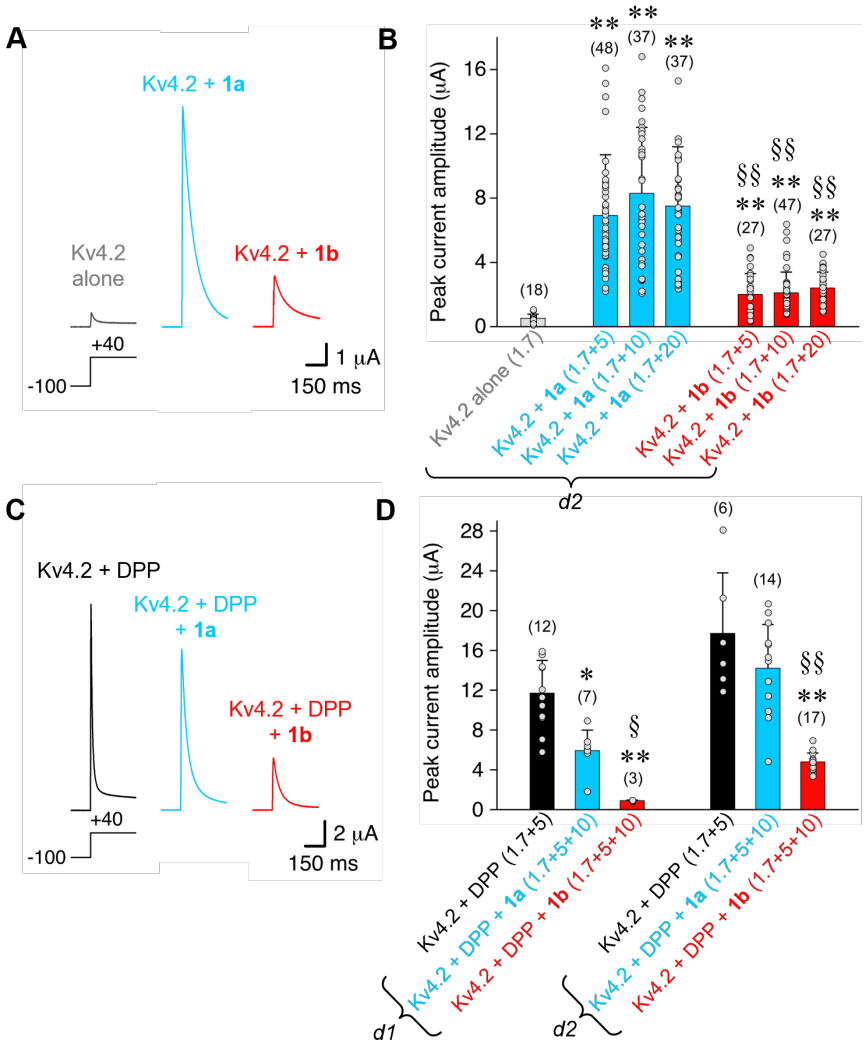

Figure 4.1 Effects of KChIP1 splice variant 1a and 1b co-expression on the peak current amplitude of Kv4.2 channel. A (binary configuration) and C (ternary configuration): Macroscopic currents mediated by Kv4.2 alone, with 1a or 1b in the absence or presence of DPP were recorded using TEVC in *Xenopus* oocytes. Recording were performed two days after cRNA injection (d2) using voltage steps from -100 mV to +40 mV, representative traces as indicated (grey trace: Kv4.2 alone (1.7); black trace: Kv4.2 + DPP (1.7 + 5); blue traces: Kv4.2 + 1a (1.7 + 10); or Kv4.2 + DPP + 1a (1.7 + 5 + 10); red traces: Kv4.2 + 1b (1.7 + 10) or Kv4.2 + DPP + 1b (1.7 + 5 + 10)). B (binary configuration) and D (ternary configuration): Bar graphs show peak current amplitudes (mean ± SD) of Kv4.2 alone (grey bar), Kv4.2 + DPP (black bar), Kv4.2 + 1a or Kv4.2 + DPP + 1a (blue bar), Kv4.2 + 1b or Kv4.2 + DPP + 1b (red bar), including individual data points. Numbers of oocytes (n) indicated; different amounts of Kv4.2, KChIP1 and DPP cRNA injected as indicated (ng per oocyte); the measurement day as indicated (d). Statistical analyses were done using one-way analysis of variance (ANOVA) with Dunnett's post hoc testing for more than two groups and unpaired Student's *t*-test for two groups. KChIP effect: significant effects of 1a and 1b co-expression (compared to Kv4.2 alone or Kv4.2 + DPP) are indicated with *($p<0.05$) or **($p<0.0001$). Special feature of the 1b splice variant: significant differences compared to Kv4.2 + 1a or Kv4.2 + DPP + 1a are indicated with § ($p<0.05$) or §§ ($p<0.0001$); comparisons were made using comparable amounts of KChIP1 cRNA and on the same day after cRNA injection.

The currents mediated by Kv4.2 + DPP, Kv4.2 + DPP + 1a and Kv4.2 + DPP + 1b (measured on d2) are shown in Figure 4.1C. Mean peak current amplitudes at +40 mV for Kv4.2 + DPP were 11.7 ± 3.3 µA (n = 12, d1) and 17.7 ± 6.1 µA (n = 6, d2). In the ternary configuration with DPP, co-expression with 10 ng of 1a or 1b did not increase peak current amplitudes either on d1 or d2, in contrast to the upregulation observed in the binary configuration (Table 4.1). However, as shown in Figure 4.1D, the peak current amplitudes for Kv4.2 + DPP + 1a (5.9 ± 2.1 µA, n = 7, d1; 14.2 ± 4.4 µA, n = 14, d2) were significantly larger compared to that of Kv4.2 + DPP + 1b (0.9 ± 0.1 µA, n=3, d1; 4.8 ± 0.9 µA, n =17, d2), which was consistent with the effects observed in the binary configuration.

4.1.2 Kinetics of macroscopic inactivation

As shown in Figure 4.2A, Kv4.2 channels activate rapidly and exhibit fast macroscopic inactivation upon depolarizing voltage pulses to +40 mV. A large portion of the current was already inactivated within less than 100 ms. To describe the kinetics of this macroscopic inactivation, a triple-exponential function was used to fit the current decays (Figure 4.2C): $\tau_{1,inact}$, $\tau_{2,inact}$ and $\tau_{3,inact}$ describe the fast, intermediate and slow time constant, respectively. The relative amplitude of each time constant ($amp_{x,inact}$) represents the proportion of the respective component in the overall decay. For Kv4.2 alone (measured between d2 and d10), $\tau_{1,inact}$ was 16.2 ± 2.1 ms (81.4 ± 2.8 %; n = 30), $\tau_{2,inact}$ was 67.7 ± 11.4 ms (14.8 ± 2.3 %), and $\tau_{3,inact}$ was 809 ± 128 ms (3.8 ± 2.1 %). Upon co-expression with 1a or 1b (10 ng per oocyte), the overall inactivation kinetics of the channels were changed in a similar manner: both fast and intermediate time constants were increased, while the slow time constant was decreased, compared to Kv4.2 alone (Figure 4.2A). Compared to Kv4.2 alone, for Kv4.2 + 1a, $\tau_{1,inact}$ and $\tau_{2,inact}$ significantly increased to 47.1 ± 14.6 ms (18.2 ± 7.7 %; n = 30) and 113 ± 24.3 ms (79.5 ± 14.5 %), respectively. The intermediate component ($amp_{2,inact}$) represented most of the decay, replacing $\tau_{1,inact}$ as the major component seen in Kv4.2 alone. On the other hand, $\tau_{3,inact}$ was significantly reduced to 697 ± 150 ms (2.3 ± 1.4 %). For Kv4.2 + 1b, $\tau_{1,inact}$ and $\tau_{2,inact}$ were significantly increased to 33.9 ± 5.0 ms (41.6 ± 7.1 %; n = 54) and 118 ± 20.0 ms (48.4 ± 8.5 %), respectively, and $\tau_{3,inact}$ was significantly reduced to 615 ± 137 ms (10.0 ± 1.4 %). In contrast to 1a, 1b slowed the inactivation by decreasing the relative amplitude of fast component and increasing the relative amplitude of intermediate component. Moreover, $\tau_{1,inact}$ of Kv4.2 + 1b was significantly smaller than that of Kv4.2 + 1a (Figure 4.2C; Table 4.1), indicating a less pronounced slowing of inactivation with 1b co-expression. The modulation of Kv4.2-mediated current decay by KChIP1 splice variants was

also not dose-dependent (Table 4.1).

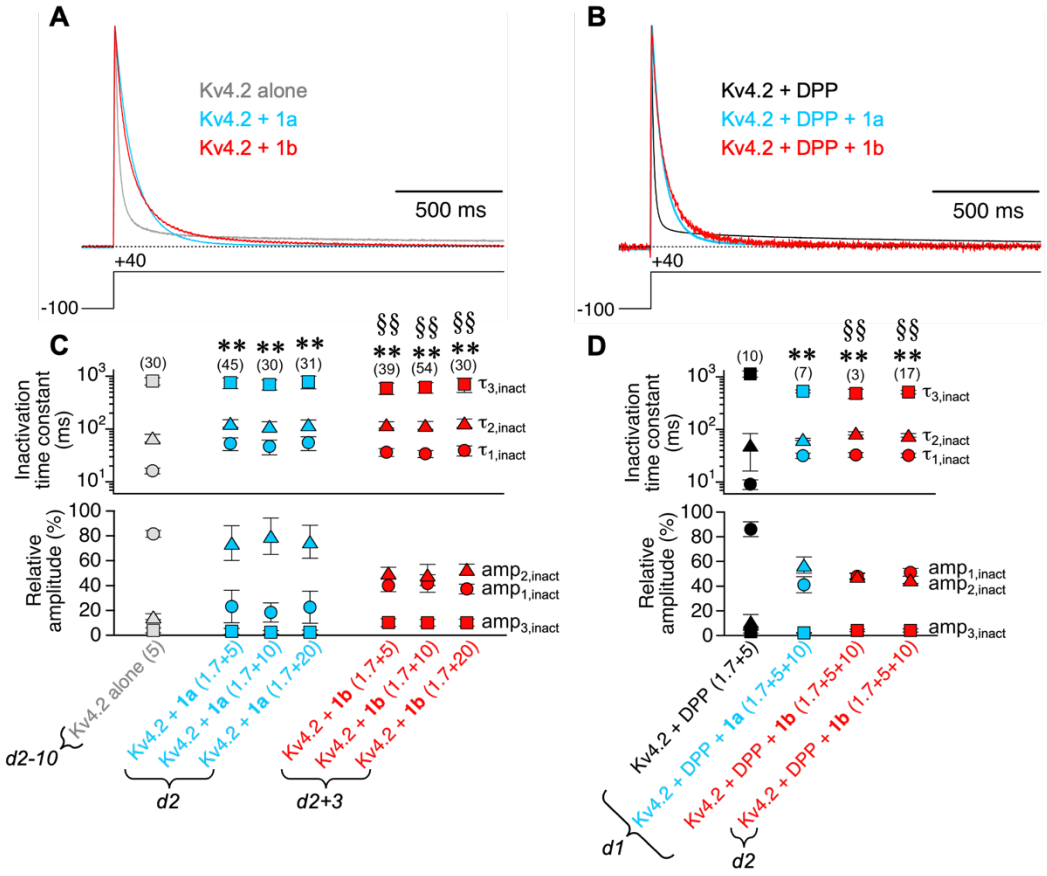

Figure 4.2 Modulation of Kv4.2 channel macroscopic inactivation by the KChIP1 splice variants 1a and 1b. A (binary configuration) and B (ternary configuration): Normalized currents mediated by Kv4.2 alone, with 1a or 1b in the absence and presence of DPP (grey trace: Kv4.2 alone (5); black trace: Kv4.2 + DPP (1.7 + 5); blue traces: Kv4.2 + 1a (1.7 + 10) or Kv4.2 + DPP + 1a (1.7 + 5 + 10); red traces: Kv4.2 + 1b (1.7 + 10) or Kv4.2 + DPP + 1b (1.7 + 5 + 10); dotted line represents zero current); currents were obtained with voltage pulses, as indicated (+40 mV for 2.5s), to study the kinetics of macroscopic inactivation (i.e., current decay). C (binary configuration) and D (ternary configuration): Inactivation time constants and their relative amplitudes obtained by fitting the current decay kinetics with a triple-exponential function ($\tau_{1,inact}$ and $amp_{1,inact}$: circle; $\tau_{2,inact}$ and $amp_{2,inact}$: triangles; $\tau_{3,inact}$ and $amp_{3,inact}$: squares) are plotted below (mean ± SD); grey symbols: Kv4.2 alone; black symbols: Kv4.2 + DPP; red symbols: Kv4.2 + 1a or Kv4.2 + DPP+ 1a; blue symbols: Kv4.2 + 1b or Kv4.2 + DPP + 1b; numbers of oocytes (n) indicated; different amounts of Kv4.2, KChIP1 and DPP cRNA injected as indicated (ng per oocyte); data were pooled from different days (d) after cRNA injction (also see Table 4.1). Statistical analyses were done using ANOVA with Dunnett's post hoc testing and unpaired Student's *t*-test for two groups. KChIP effect: significant effects of 1a and 1b co-expression (compared to Kv4.2 alone or Kv4.2 + DPP) are indicated with * ($p<0.05$) or ** ($p<0.0001$). Special feature of the 1b splice variant: significant differences compared to Kv4.2 + 1a or Kv4.2 + DPP + 1a are indicated with § ($p<0.05$) or §§ ($p<0.0001$); comparisons were made using comparable amounts of KChIP1 cRNA. Statistical significance symbols represent the highest degree of significance found in ⩾ 1 of 6 parameters analysed (see Table 4.1 for more details).

To further investigate the effects of 1a and 1b on macroscopic inactivation in the presence of DPP, normalized currents mediated by Kv4.2 + DPP, Kv4.2 + DPP + 1a and Kv4.2 + DPP + 1b were analysed (Figure 4.2B and 4.2D). Kv4.2 + DPP channels exhibited a $\tau_{1,inact}$ of 9.1

± 1.9 ms (86.0 ± 6.0 %; n = 10), $\tau_{2,inact}$ of 50 ± 33.8 ms (11 ± 6 %) and $\tau_{3,inact}$ of 1136 ± 156 ms (3.5 ± 1.2 %) on d1 after cRNA injection. Upon co-expression with 1a (Kv4.2 + DPP + 1a), $\tau_{1,inact}$ was significantly increased to 31.7 ± 3.6 ms (41.0 ± 6.5 %, n = 7), while $\tau_{3,inact}$ was decreased to 531 ± 32.0 ms (1.8 ± 0.5 %). Similarly, for Kv4.2 + DPP + 1b, $\tau_{1,inact}$ was increased to 32.8 ± 3.5 ms (48.4 ± 2.7 %; n = 3) and $\tau_{2,inact}$ was increased to 84.6 ± 5.8 ms (47.8 ± 2.1 %), while $\tau_{3,inact}$ was reduced to 483 ± 98 ms (3.7 ± 0.9 %), compared to Kv4.2 + DPP. Thus, the differences between 1a and 1b co-expression observed in the binary configuration, especially in the relative amplitudes of the three inactivation time constants, became less obvious in the presence of DPP (Table 4.1). Although peak current amplitudes differed considerably, macroscopic inactivation kinetics of Kv4.2 + DPP + 1b channels were virtually identical on d1 and d2.

4.1.3 Kinetics of recovery from inactivation

It has been previously reported that, unlike 1a, co-expression of 1b causes biphasic kinetics of recovery from inactivation, resulting in a remarkable slowing of the overall recovery process in Kv4.2 channels (Van Hoorick et al., 2003). To test whether this effect still exist in the *Xenopus* oocyte expression system, we used TEVC both in the absence and presence of DPP. Recovery kinetics were measured using a double-pulse protocol from -100 mV to +40 mV with varying time intervals between depolarizing pulses at -80 mV. Figure 4.3A and 4.3B show recovery current traces of Kv4.2 alone and Kv4.2 + 1b, Kv4.2 + DPP and Kv4.2 + DPP +1b. More channels can be activated with the increasing interpulse durations, which was reflected by the increase in test current amplitudes. Once the test currents reached a stable state, the recovery from inactivation was complete. In both binary and ternary configurations, 1b co-expression required longer interpulse intervals to complete the recovery process, indicating that 1b slowed the recovery from inactivation compared to Kv4.2 alone or Kv4.2 + DPP. The recovery of Kv4.2 alone was well described with a single-exponential function, with a recovery time constant (τ_{rec}) of 563 ± 76.0 ms (n = 16). Surprisingly, when co-expressed with 1a, the recovery was fitted with a double-exponential function, in contrast to the previous findings in a stable Kv4.2-expressing cell-line (Van Hoorick et al., 2003). For Kv4.2 + 1a (1.7 + 10 ng cRNA per oocyte), the fast ($\tau_{1,rec}$) and slow ($\tau_{2,rec}$) time constants were 149 ± 22 ms (85.0 ± 2.8 %; n = 16) and 1674 ± 296 ms (15.3 ± 2.9 %), respectively, resulting in an overall acceleration of recovery (Figure 4.3C).

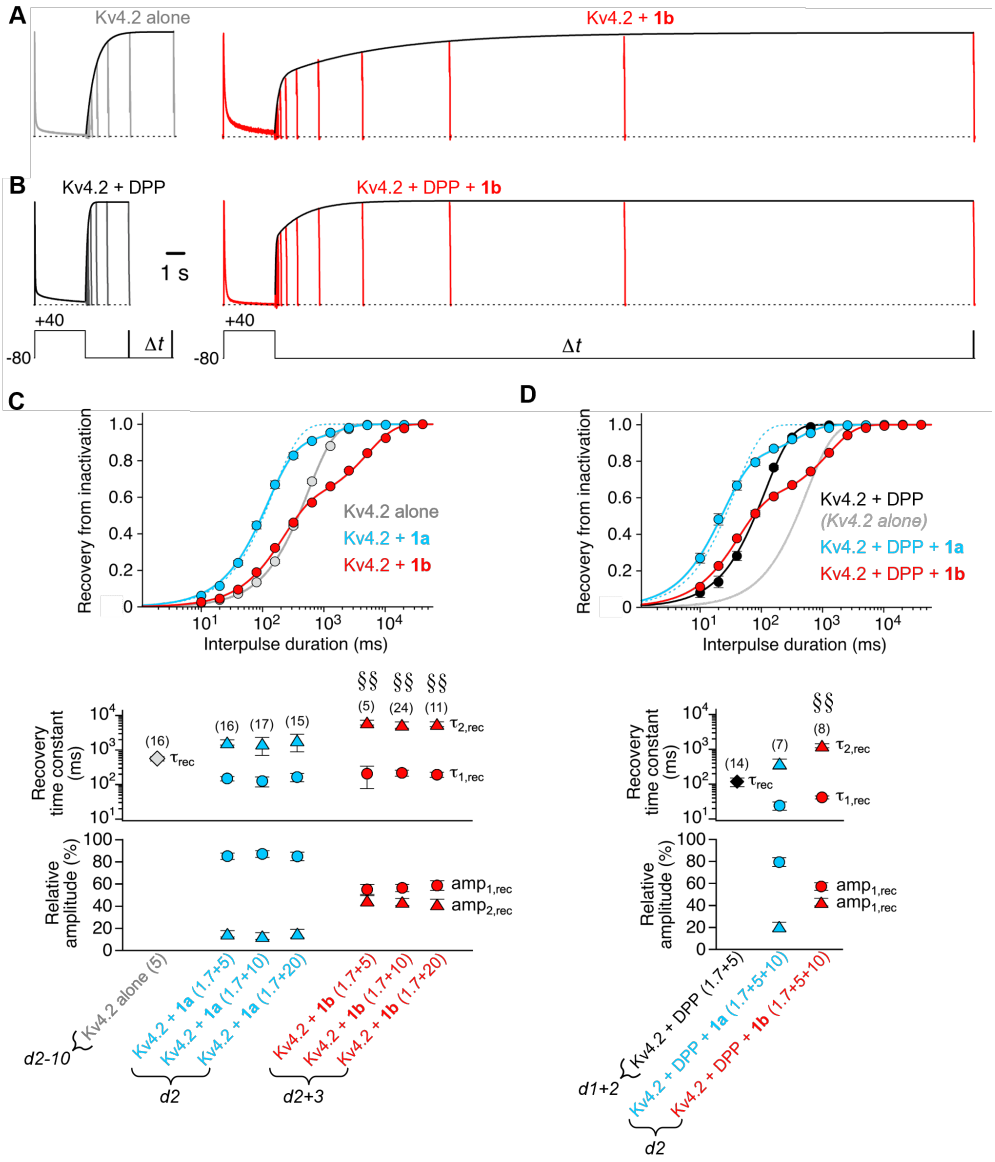

Figure 4.3 Modulation of Kv4.2 channel recovery kinetics by the KChIP1 splice variants 1a and 1b. A (binary configuration) and B (ternary configuration): Recovery from inactivation was measured using a double-pulse protocol with long control and brief test pulses to +40 mV (3 s) and variable interpulse durations at −80 mV (recovery potential; Δt, see inset). C (binary configuration) and D (ternary configuration): Normalized data ($I_{test}/I_{control}$, mean ± SEM) were plotted against the interpulse duration on a log-scale and described by a single- (Kv4.2 alone (5) and Kv4.2 + DPP (1.7 + 5)) or double-exponential function (Kv4.2 + KChIP1 (1.7 + 10) and Kv4.2 + DPP + KChIP1 (1.7 + 5 + 10)). Recovery time constants from single-exponential fits (τ_{rec}, diamonds) and time constants including their relative amplitudes from double-exponential fits ($\tau_{1,rec}$ and $amp_{1,rec}$: circles; $\tau_{2,rec}$ and $amp_{2,rec}$: triangles) are presented as means ± SD; grey symbols and curves: Kv4.2 alone; black symbols and curves: Kv4.2 + DPP; red symbols and curves: Kv4.2 + 1a or Kv4.2 + DPP+ 1a; blue symbols and curves: Kv4.2 + 1b or Kv4.2 + DPP + 1b. Numbers of oocytes (n) indicated; different amounts of Kv4.2, KChIP1 and DPP cRNA applied as indicated (ng per oocyte); data were pooled from different days (d) after cRNA injction (also see Table 4.1). Statistical analyses were done using ANOVA with Dunnett's post hoc testing and unpaired Student's *t*-test for two groups. KChIP effect: significant effects of 1a and 1b co-expression (compared to Kv4.2 alone or Kv4.2 + DPP) are indicated with * ($p<0.05$) or ** ($p<0.0001$). Special feature of the 1b splice variant: significant differences compared to Kv4.2 + 1a or Kv4.2 + DPP + 1a are indicated with § ($p<0.05$) or §§ ($p<0.0001$); comparisons were made using comparable amounts of KChIP1 cRNA. Statistical significance symbols represent the highest degree of significance found in ⩾ 1 of 4 parameters analysed (see Table 4.1 for more details).

Similarly, co-expression with 10 ng 1b also induced a second but extremely slow recovery component. The $\tau_{2,rec}$ was 5347 ± 1125 ms, representing approximately 44 % of the recovery from inactivation (Table 4.1), and was significantly larger compared to τ_{rec} of Kv4.2 alone or $\tau_{2,rec}$ of Kv4.2 + 1a. Compared to Kv4.2 + 1a, the relative amplitudes of $\tau_{2,rec}$ was larger in the presence of 1b ($p<0.0001$). Thus, the effect of 1b on Kv4.2 recovery kinetics, slowing rather than accelerating recovery from inactivation, was still present in the *Xenopus* oocyte expression system. Of note, the modulatory effects of 1a and 1b on recovery from inactivation were also not dose-dependent (Table 4.1).

The recovery of Kv4.2 + DPP was well described by a single-exponential function, with a τ_{rec} of 117 ± 32 ms (n = 14), indicating a faster recovery kinetics compared to Kv4.2 alone (Figure 4.3D). Biphasic recovery kinetics were also observed for both 1a and 1b co-expression in the ternary configuration with DPP. For Kv4.2 + DPP + 1a, $\tau_{1,rec}$ was 24.2 ± 6.6 ms (79.3 ± 4.0 %; n = 7) and $\tau_{2,rec}$ was 395 ± 128 ms (20.7 ± 4.0 %). The contribution of the slow component appeared to be more pronounced in the ternary configuration with 1a. For Kv4.2 + DPP + 1b, $\tau_{1,rec}$ was 41.1 ± 4.2 ms (57.1 ± 3.5 %; n = 8) and $\tau_{2,rec}$ was 1275 ± 167 ms (42.9 ± 3.5 %). Despite the presence of DPP, the relative amplitudes of each time constant of Kv4.2 + DPP + 1b remained consistent. Notably, the slow component with 1b was approximately four times longer compared to that seen with 1a ($p<0.0001$), confirming that the special 1b effect of slowing recovery kinetics is also visible in the ternary configuration with DPP.

4.1.4 Voltage dependence of activation and steady-state inactivation

The voltage dependence of the steady-state inactivation was determined from the peak currents during test pulses at +40 mV, which were separated by different interpulse voltages between -120 mV and 0 mV (ΔV: 10mV increments, 10 s). The resulting test currents were normalized to control currents ($I_{test}/I_{control}$) and were plotted against the voltages of the interpulse and fitted with a single Boltzmann function (Figure 4.4A and 4.4C), which yielded the voltage of halfmaximal inactivation ($V_{1/2,inact}$) and the slope factor (s_{inact}), shown in Figure 4.4B and D. $V_{1/2,inact}$ of the inactivation described that at this potential, 50% of the channels were at the inactivated state. For Kv4.2 alone, $V_{1/2,inact}$ was -68.3 ± 2.2 mV (n = 14) with an s_{inact} of 6.4 ± 2.2 mV. Upon co-expression with 10 ng of 1a, $V_{1/2,inact}$ (-66.3 ± 2.7 mV; n = 16) was not significantly different from Kv4.2 alone, although s_{inact} became smaller (5.2 ± 0.8 mV). Co-expression with 10 ng of 1b shifted $V_{1/2,inact}$ to -76.0 ± 2.5 mV (n = 14), with

an s_{inact} of 6.1 ± 1.2 mV, which was significantly more negative compared to Kv4.2 alone and with 1a ($p<0.0001$). The leftward shift of the steady-state inactivation curve indicates that the channels are more likely to inactivate at hyperpolarized potentials. The modulatory effects of 1a and 1b on the voltage dependence of steady-state inactivation of Kv4.2 channels in *Xenopus* oocytes were consistent with previous results in HEK cells (Van Hoorick et al., 2003). Similarly, these effects were also not dose-dependent (Table 4.1). Typically, DPP co-expression caused a negative shift of the inactivation curve (Nadal et al., 2003), so that $V_{1/2,inact}$ was -73.5 ± 1.5 mV (s_{inact} was 4.7 ± 0.2 mV; n = 6) for Kv4.2 + DPP. In the ternary configuration with DPP, halfmaximal inactivation occurred at -74.4 ± 2.5 mV (s_{inact} was 4.3 ± 0.3 mV; n = 7) for Kv4.2 + DPP + 1a, and at -81.3 ± 1.5 mV (s_{inact} was 7.4 ± 1.0 mV; n = 9) for Kv4.2 + DPP + 1b, respectively, suggesting that 1b still induced a leftward shift of steady-state inactivation curve in the presence of DPP, similar to its effect in the binary configuration (Figure 4.4D; Table 4.1).

In order to investigate the voltage dependence of activation, the *I-V* protocol was performed using test pulses to voltages between -90 mV and +70 mV (ΔV: 10 mV increments, 2.5 s). The measured peak current amplitudes were converted to conductance of the channels, normalized to maximum and plotted against the test pulse voltage. Fitting the data with a 4th order Boltzmann equation (Figure 4.4A and 4.4C) yielded the voltage of halfmaximal activation ($V_{1/2,act}$) and the slope factor (s_{act}), shown in Figure 4.4B and 4.4D. The $V_{1/2,act}$ indicated the potential at which there was a 50 % probability that the channel was in the open state. For Kv4.2 alone, $V_{1/2,act}$ was +5.5 ± 5.0 mV (n = 12), with an s_{act} of 33.8 ± 2.5 mV. Co-expression of both KChIP1 splice variants (10 ng per oocyte) caused a steepening and a negative shift of activation curves. For Kv4.2 + 1a, $V_{1/2,act}$ was –9.6 ± 4.8 mV and s_{act} was 25.6 ± 1.3 mV (n = 14), whereas for Kv4.2 + 1b, $V_{1/2,act}$ was –5.7 ± 5.6 mV and s_{act} was 30.8 ± 4.9 mV (n = 11). Although both 1a and 1b modulated activation, the effect of 1b was weaker compared to that of 1a, and this difference seen in the binary configuration was not dependent on the amount of KChIP1 cRNA (Figure 4.4A and 4.4B; Table 4.1). In the presence of DPP, $V_{1/2,act}$ for Kv4.2 + DPP was –28.5 ± 5.0 mV (n = 8) and s_{act} was 23.2 ± 5.0 mV, indicating the typical DPP effect in a negative shift of the activation curve (Figure 4.4A and 4.4C). By contrast, in a ternary configuration with DPP, 1a and 1b co-expression caused a positive shift of activation curves compared to Kv4.2 + DPP. For Kv4.2 + DPP + 1a, $V_{1/2,act}$ was -19.2 ± 3.6 mV (n = 6) and s_{act} was 26.1 ± 2.1 mV, and for Kv4.2 + DPP + 1b, $V_{1/2,act}$ was -12.1 ± 3.6 mV (n = 7) and s_{act} was 33.7 ± 2.4 mV. Specially, the effect of 1b in

modulating $V_{1/2,act}$ was stronger than 1a, and it also had a larger slope factor (Table 4.1). In summary, the typical KChIP1-mediated negative shift of $V_{1/2,act}$ of the activation observed in the binary configuration was not seen in the presence of DPP.

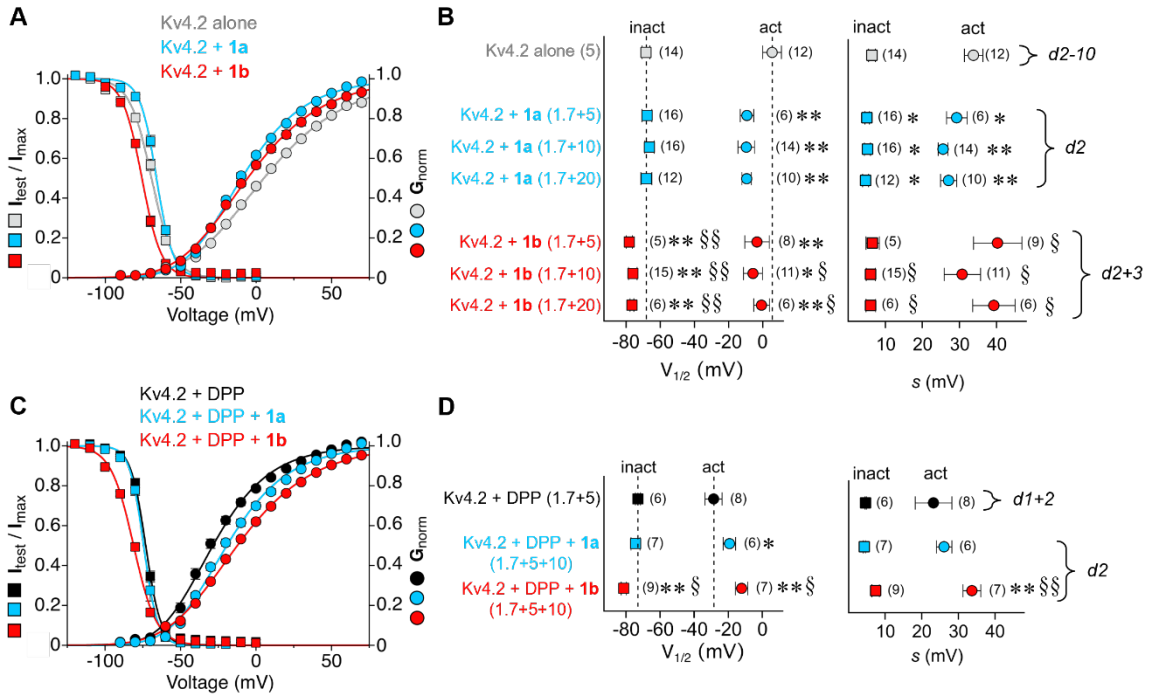

Figure 4.4 Effects of KChIP1 splice variants 1a and 1b on the voltage dependence of Kv4.2 channel gating. A (binary configuration) and C (ternary configuration): Voltage dependences of activation (circles) and steady-state inactivation (squares) are shown in the same graphs. Normalized conductance values of voltage dependences of activation were plotted against the test pulse voltages and fitted with a 4th Boltzmann equation. Normalized data ($I_{test}/I_{control}$) of steady-state inactivation were plotted against the voltages of the interpulse and fitted with a single Boltzmann function. Grey curves: Kv4.2 alone (5); black curves: Kv4.2 + DPP (1.7 + 5); blue curves: Kv4.2 + 1a (1.7 + 10) or Kv4.2 + DPP + 1a (1.7 + 5 + 10); red curves: Kv4.2 + 1b (1.7 + 10) or Kv4.2 + DPP + 1b (1.7 + 5 + 10). Error bars are SEM. B (binary configuration) and D (ternary configuration): Voltages of halfmaximal inactivation (inact, squares) and halfmaximal activation (act, circles) and corresponding slope factors ($V_{1/2}$ and *s*, respectively) are presented as mean ± SD; grey symbols: Kv4.2 alone; black symbols: Kv4.2 + DPP; blue symbols: Kv4.2 + 1a or Kv4.2 + DPP + 1a; red symbols: Kv4.2 + 1b or Kv4.2 + DPP + 1b. Numbers of oocytes (n) indicated; different amounts of Kv4.2, KChIP1 and DPP cRNA applied as indicated (ng per oocyte); data were pooled from different days (d) after cRNA injction (also see Table 4.1). Statistical analyses were done using ANOVA with Dunnett's post hoc testing and unpaired Student's *t*-test for two groups. KChIP effect: significant effects of 1a and 1b co-expression (compared to Kv4.2 alone or Kv4.2 + DPP) are indicated with * ($p<0.05$) or ** ($p<0.0001$). Special feature of the 1b splice variant: significant differences compared to Kv4.2 + 1a or Kv4.2 + DPP + 1a are indicated with § ($p<0.05$) or §§ ($p<0.0001$); comparisons were made using comparable amounts of KChIP1 cRNA.

Table 4.1 Functional characterization of Kv4.2 in the absence and presence of KChIP1 splice variants 1a and 1b in different channel configurations.

configuration (ng, *day*)	I (+40) (µA)	$\tau_{1.inact}$ (ms)	$amp_{1.inact}$ (%)	$\tau_{2.inact}$ (ms)	$amp_{2.inact}$ (%)	$\tau_{3.inact}$ (ms)	$amp_{3.inact}$ (%)	$\tau_{1.rec}/\tau_{rec}$ (ms)	$amp_{1.rec}$ (%)	$\tau_{2.rec}$ (ms)	$amp_{2.rec}$ (%)	$V_{1/2.act}$ (mV)	s_{act} (mV)	$V_{1/2.inact}$ (mV)	s_{inact} (mV)
Kv4.2 alone (5, *d2-d10*)	-	16.2 ± 2.1 (30)	81.4 ± 2.8 (30)	67.7 ± 11.4 (30)	14.8 ± 2.3 (30)	809 ± 128 (30)	3.8 ± 2.1 (30)	563 ± 76 (16)	-			5.5 ± 5.0 (12)	33.8 ± 2.5 (12)	-68.3 ± 2.2 (14)	6.4 ± 0.9 (14)
Kv4.2 alone (1.7, *d2*)	0.5 ± 0.3 (18)	-													
Kv4.2 + 1a (1.7+5, *d2*)	6.9 ± 3.8^{kk} (48)	53.4 ± 14.5^{kk} (45)	23.0 ± 13.0^{kk} (45)	128 ± 21$^{kk,\#}$ (45)	74.0 ± 14.0^{kk} (45)	753 ± 175 (45)	3.0 ± 2.5 (45)	149 ± 22 (16)	85.0 ± 2.8$^{\#}$ (16)	1674 ± 296 (16)	15.3 ± 2.9$^{\#}$ (16)	-9.2 ± 3.9^{kk} (6)	29.3 ± 2.8$^{k,\#}$ (6)	-67.7 ± 2.9 (16)	5.1 ± 0.6^{k} (16)
Kv4.2 + 1a (1.7+10, *d2*)	8.3 ± 4.1^{kk} (37)	47.1 ± 14.6^{kk} (30)	18.2 ± 7.7^{kk} (30)	113 ± 24.3^{kk} (30)	79.5 ± 14.5^{kk} (30)	697 ± 150 (30)	2.3 ± 1.4^{k} (30)	126 ± 40 (17)	87.0 ± 3.0 (17)	1514 ± 825 (17)	12.5 ± 2.4 (17)	-9.6 ± 4.8^{kk} (14)	25.6 ± 1.3^{kk} (14)	-66.3 ± 2.7 (16)	5.2 ± 0.8^{k} (16)
Kv4.2 + 1a (1.7+20, *d2*)	7.5 ± 3.7^{kk} (37)	55.2 ± 16.3^{kk} (31)	22.5 ± 12.9^{kk} (31)	121 ± 27^{kk} (31)	75.1 ± 13.2^{kk} (31)	789 ± 216 (31)	2.3 ± 1.6^{k} (31)	164 ± 44$^{\#}$ (15)	84.8 ± 3.9$^{\#}$ (15)	1893 ± 1002 (15)	15.2 ± 3.9$^{\#}$ (15)	-9.4 ± 2.7^{kk} (10)	27.1 ± 2.2^{kk} (10)	-68.1 ± 3.2 (12)	4.7 ± 0.8^{k} (12)
Kv4.2 + 1b (1.7+5, *d2*)	2.0 ± 1.3^{kk,cc} (27)	36.5 ± 6.1^{kk,cc} (39)	40.0 ± 5.0^{kk,cc} (39)	121 ± 16.1^{kk} (39)	50.0 ± 4.5^{kk,cc} (39)	594 ± 145^{kk,cc} (39)	10.1 ± 3.1^{kk,cc} (39)	207 ± 131 (5)	55.0 ± 4.5^{cc} (5)	6325 ± 1047^{c} (5)	45.0 ± 5.0^{cc} (5)	-3.3 ± 7.2^{kk} (8)	40.3 ± 6.5$^{\#,c}$ (8)	-78.1 ± 1.8^{kk,cc} (5)	6.6 ± 1.8 (5)
Kv4.2 + 1b (1.7+5, *d3*)	-														
Kv4.2 + 1b (1.7+10, *d2*)	2.1 ± 1.3^{kk,bb} (47)	33.9 ± 5^{kk,bb} (54)	41.6 ± 7.1^{kk,bb} (54)	117.9 ± 20.0^{kk} (54)	48.4 ± 8.5^{kk,bb} (54)	615 ± 137^{kk,b} (54)	10.0 ± 2.7^{kk,bb} (54)	218 ± 43^{bb} (24)	56.3 ± 3.3^{bb} (24)	5347 ± 1125^{bb} (24)	44.1 ± 4.0^{bb} (24)	-5.7 ± 5.6^{k,b} (11)	30.8 ± 4.9^{b} (11)	-76.0 ± 2.5^{kk,bb} (15)	6.1 ± 1.2^{b} (15)
Kv4.2 + 1b (1.7+10, *d3*)	-														
Kv4.2 + 1b (1.7+20, *d2*)	2.4 ± 1.0^{kk,dd} (27)	39.3 ± 8.5^{kk,dd} (30)	37.2 ± 3.9^{kk,dd} (30)	130 ± 24^{kk} (30)	52.9 ± 4.3^{kk,dd} (30)	707 ± 214$^{k,\#}$ (30)	10.0 ± 2.8^{kk,dd} (30)	192 ± 33 (11)	58.5 ± 4.5^{dd} (11)	5658 ± 945^{dd} (11)	41.5 ± 4.5^{dd} (11)	-0.7 ± 4.6^{kk,d} (6)	39.3 ± 5.7^{d} (6)	-76.5 ± 1.1^{kk,dd} (6)	6.1 ± 1.3^{d} (6)
Kv4.2 + 1b (1.7+20, *d3*)	-														
Kv4.2 + DPP (1.7+5, *d1*)	11.7 ± 3.3 (12)	9.1 ± 1.9 (10)	86.0 ± 6.0 (10)	50.0 ± 33.8 (10)	11.0 ± 6.0 (10)	1136 ± 156 (10)	3.5 ± 1.2 (10)	117 ± 32 (14)	-			-28.5 ± 5.0 (8)	23.2 ± 5 (8)	-73.5 ± 1.5 (6)	4.7 ± 0.2 (6)
Kv4.2 + DPP (1.7+5, *d2*)	17.7 ± 6.1 (6)	-													
Kv4.2 + DPP + 1a (1.7+5+10, *d1*)	5.9 ± 2.1^{tt} (7)	31.7 ± 3.6^{tt} (7)	41.0 ± 6.5^{tt} (7)	64.5 ± 3.0 (7)	57.2 ± 6.5^{tt} (7)	531 ± 32^{tt} (7)	1.8 ± 0.5^{t} (7)	-							
Kv4.2 + DPP + 1a (1.7+5+10, *d2*)	14.2 ± 4.4 (14)	-						24.2 ± 6.6 (7)	79.3 ± 4.0 (7)	395 ± 128 (7)	20.7 ± 4.0 (7)	-19.2 ± 3.6^{t} (6)	26.1 ± 2.1 (6)	-74.4 ± 2.6 (7)	4.3 ± 0.3 (7)
Kv4.2 + DPP + 1b (1.7+5+10, *d1*)	0.9 ± 0.1^{tt,bb} (3)	32.8 ± 3.5^{tt} (3)	48.4 ± 2.7^{tt,b} (3)	84.6 ± 5.8^{b} (3)	47.8 ± 2.1^{tt,b} (3)	483 ± 98^{tt} (3)	3.7 ± 0.9 (3)	-							
Kv4.2 + DPP + 1b (1.7+5+10, *d2*)	4.8 ± 0.9^{tt,bb} (17)	32.0 ± 3.0^{tt} (17)	51.0 ± 3.2^{tt,b} (17)	77.4 ± 6.4^{t,bb} (17)	45.2 ± 2.8^{tt,b} (17)	513 ± 40^{tt} (17)	4.0 ± 1.3^{bb} (17)	41.4 ± 4.2^{b} (8)	57.1 ± 3.5^{bb} (8)	1275 ± 167^{bb} (8)	42.9 ± 3.5^{bb} (8)	-12.1 ± 3.6^{tt,b} (7)	33.7 ± 2.4^{tt,bb} (7)	-81.3 ± 1.5^{tt,b} (9)	7.4 ± 1.0^{tt,bb} (9)

Kv4.2 was expressed alone or in different channel configurations with either KChIP1a (1a) or KChIP1b (1b) in *Xenopus* oocytes (cRNA amounts in ng per oocyte indicated). Functional characterization under two-electrode voltage-clamp was performed on day 1 - 10 after cRNA injection (as indicated; *d1 - d10*). Mean values ± SD and number of oocytes (n) are given for the peak current amplitude, time constants of macroscopic inactivation and recovery from inactivation (including relative amplitudes in %), and the voltages of halfmaximal activation and inactivation (including slope factors, *s*). Statistical analyses were done using one-way analysis of variance (ANOVA) with Dunnett's post hoc testing for more than two groups and an unpaired Student's *t*-test for two groups. Superscript letters k, b, c, d, t and # denote significant differences; single letter: $p<0.05$; two letters: $p<0.0001$; k, kk: significantly different from Kv4.2 alone (KChIP effect, binary); b, bb: significantly different from Kv4.2 co-expressed with 10 ng 1a cRNA in the absence or presence of DPP; c,cc: significantly different from Kv4.2 co-expressed with 5 ng 1a cRNA; d, dd: significantly different from Kv4.2 co-expressed with 20 ng 1a cRNA (special features of the KChIP1b splice variant); #: significantly different from Kv4.2 co-expressed with 10 ng 1a or 1b cRNA; t,tt: significantly different from Kv4.2 + DPP (KChIP effect in the presence of DPP, ternary).

4.2 Modulation of other Kv4 channel subtypes by KChIP1 splice variants

We found that 1a and 1b induced a second recovery component both in the absence and presence of DPP, although effects of KChIP1 splice variants on functional expression, current decay and voltage dependence of activation and inactivation were not exactly the same in different configurations. To investigate whether 1a and 1b modulate all Kv4 channel subtypes in a same manner, Kv4.1, Kv4.3S and Kv4.3L are illustrated.

4.2.1 Peak current amplitude

The mean peak current amplitude for Kv4.1 (1.7 ng per oocyte) was 1.1 ± 0.5 μA (n = 8) on d2 after cRNA injection (Figure 4.5). Co-expression with 1a significantly increased the current amplitude to 9.5 ± 3.1 μA (n = 33), while 1b increased it to 4.0 ± 1.6 μA (n = 33), which was significantly smaller than that of Kv4.1 + 1a ($p<0.0001$). The weaker effect of 1b on current enhancement in Kv4.1 was similar to that observed in Kv4.2. Mean peak current amplitudes at +40 mV for Kv4.1 + DPP, Kv4.1 + DPP + 1a and Kv4.1 + DPP + 1b were measured on both d1 and d2 (Figure 4.5B). For Kv4.1 + DPP, the current amplitudes were 4.4 ± 1.0 μA (n = 9; d1) and 19.4 ± 5.4 μA (n = 17; d2). In the ternary configuration with DPP, co-expression of 1a increased the current amplitude on d1 to 6.9 ± 1.2 μA (n = 10) compared to Kv4.1 + DPP. On d2, although the current further increased to 20.3 ± 3.7 μA, it was no longer significantly different from Kv4.1 + DPP. In contrast, co-expression of 1b did not increase current amplitude on d1 (Table 4.2), but it was decreased to 14.6 ± 3.0 μA on d2 (n = 10).

To ensure high-quality current recordings, 0.8 ng cRNA of Kv4.3S and 5 ng cRNA of 1a or 1b were injected (Table 4.3). For Kv4.3S alone, the peak current amplitude was 2.6 ± 1.2 μA (n = 25). Co-expression with both KChIP1 splice variants increased Kv4.3S currents, with 17.3 ± 4.4 μA (n = 22) for Kv4.3S + 1a and 6.2 ± 1.7 μA (n = 16) for Kv4.3S + 1b (Figure 4.5C). A weaker effect of 1b on current enhancement in Kv4.3S was also observed here. For Kv4.3S + DPP, the current amplitudes were 16.7 ± 3.9 μA (n = 7; d1) and 38.9 ± 12 μA (n = 8; d2). In the ternary configuration with DPP, co-expression of 1a significantly increased current amplitude to 23.3 ± 5.8 μA (n = 5) on d1 and 54.9 ± 15.8 μA (n = 4) on d2 compared to Kv4.3S + DPP. In contrast, co-expression of 1b reduced current amplitudes both on d1 (10 ± 2.1 μA; n = 7) and d2 (23.7 ± 5.4 μA; n = 8; Figure 4.5D). Thus, 1a increased the current amplitudes of Kv4.3S in both binary and ternary configurations, while 1b only upregulated Kv4.3S in the absence of DPP.

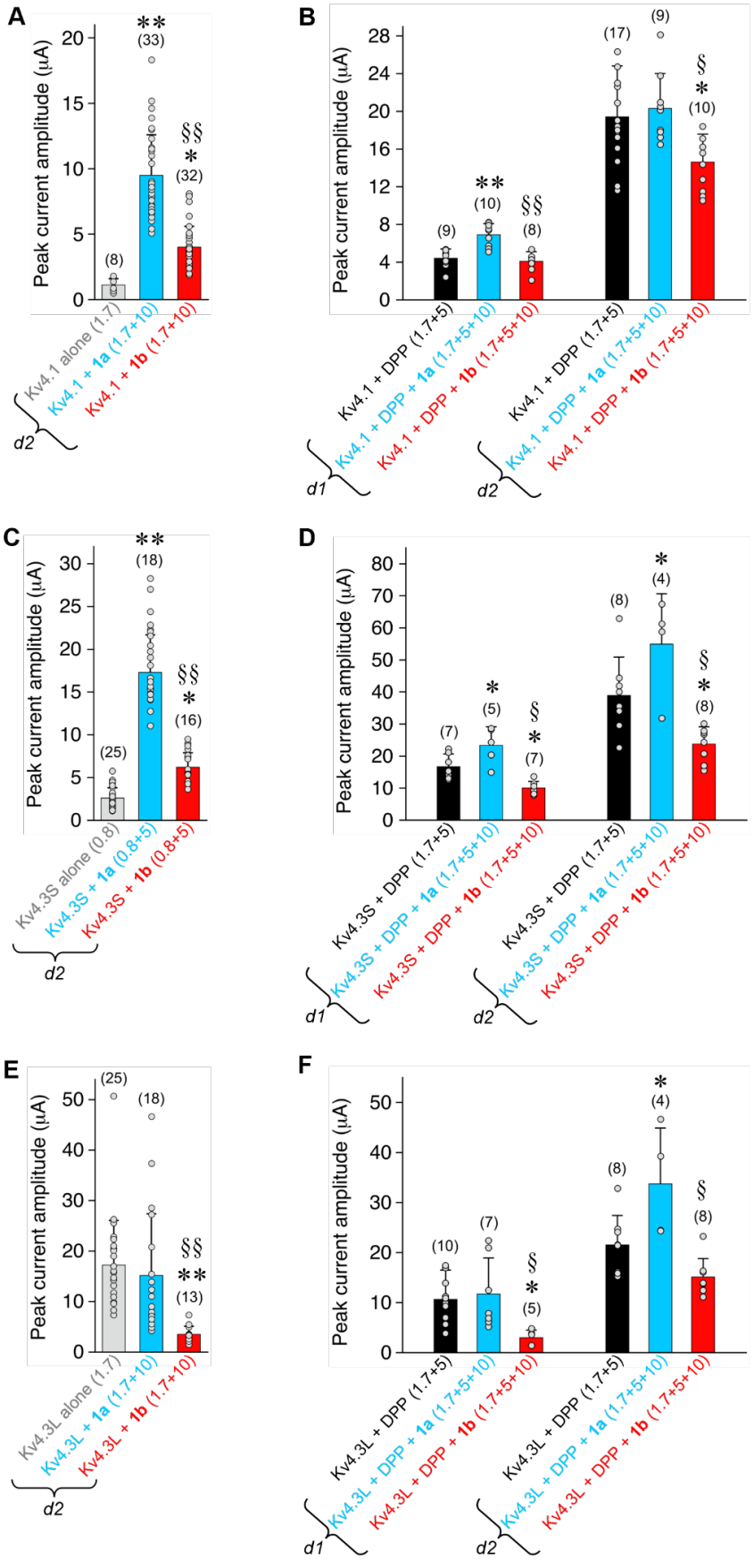
A
Peak current amplitude (µA)
Kv4.1 alone (1.7)
Kv4.1 + 1a (1.7+10)
Kv4.1 + 1b (1.7+10)
d2
B
Peak current amplitude (µA)
Kv4.1 + DPP (1.7+5)
Kv4.1 + DPP + 1a (1.7+5+10)
Kv4.1 + DPP + 1b (1.7+5+10)
d1
d2
C
Peak current amplitude (µA)
Kv4.3S alone (0.8)
Kv4.3S + 1a (0.8+5)
Kv4.3S + 1b (0.8+5)
d2
D
Peak current amplitude (µA)
Kv4.3S + DPP (1.7+5)
Kv4.3S + DPP + 1a (1.7+5+10)
Kv4.3S + DPP + 1b (1.7+5+10)
d1
d2
E
Peak current amplitude (µA)
Kv4.3L alone (1.7)
Kv4.3L + 1a (1.7+10)
Kv4.3L + 1b (1.7+10)
d2
F
Peak current amplitude (µA)
Kv4.3L + DPP (1.7+5)
Kv4.3L + DPP + 1a (1.7+5+10)
Kv4.3L + DPP + 1b (1.7+5+10)
d1
d2

Figure 4.5 Modulation of other Kv4 channels peak current amplitudes by KChIP1 splice variants. Kv4 channels were expressed in the absence or presence of auxiliary β-subunits by cRNA injection in *Xenopus laevis* oocytes. Currents were activated by voltage jumps from -100 to +40 mV under TEVC, and peak current amplitudes were measured. Summary graphs are shown for Kv4.1 (**A, B**), Kv4.3S (**C, D**) and Kv4.3L (**E, F**). Kv4.x alone: grey bars; Kv4.x + DPP: black bars; co-expression with 1a (blue) or 1b (red) in a binary (left) and a ternary configuration (right); individual data points, number of oocytes (n) and amounts of cRNA (ng per oocyte) indicated. Measurements were performed one (d1) or two days (d2) after cRNA injection. Significant differences of KChIP1 effects (compared to Kv4.x alone or Kv4.x + DPP) are indicated with * ($p<0.05$) or ** ($p<0.0001$; ANOVA). Significant differences seen with special features of the 1b splice variant (compared to 1a co-expression for comparable amounts of KChIP1 cRNA) are indicated with § ($p<0.05$) or §§ ($p<0.0001$; unpaired Student's *t*-test).

For Kv4.3L alone (1.7 ng per oocyte), the peak current amplitude was 17.2 ± 8.9 µA (n = 25; Figure 4.5E). Unlike the other Kv4 subfamily members, co-expression with 1a did not increase Kv4.3L current amplitude (15.2 ± 12.2 µA; n = 18). By contrast, co-expression with 1b significantly decreased Kv4.3L currents to 3.5 ± 1.6 µA (n = 13). For Kv4.3L + DPP, the current amplitudes were 10.6 ± 5.9 µA (n = 10; d1) and 21.5 ± 5.9 µA (n = 8; d2). In the ternary configuration with DPP (Figure 4.5F), the current amplitude of Kv4.3L + DPP + 1a was 11.7 ± 7.2 µA (n = 7) on d1, not significantly different from Kv4.3L + DPP. On d2, it increased to 33.7 ± 11.2 µA (n = 4), which was significantly larger compared to Kv4.3L + DPP. For Kv4.3L + DPP + 1b, a decrease in current amplitude on d1 (3.0 ± 1.5 µA; n = 5) compared to Kv4.3L + DPP was observed, while on d2, current amplitude was 15.1 ± 3.7 µA (n = 8), which was not significantly different from Kv4.3L + DPP. These results indicate that 1a and 1b may modulate Kv4.3L current amplitudes in a time-dependent manner in the ternary configuration. In all Kv4 channels, 1a co-expression consistently mediated larger current amplitudes than 1b co-expression on both d1 and d2, regardless of the presence of DPP.

4.2.2 Kinetics of macroscopic inactivation

Kv4.1 channels activated and inactivated rapidly upon depolarization (Figure 4.6A). The kinetics of macroscopic inactivation were described with a triple-exponential function. For Kv4.1 alone, $\tau_{1,inact}$ was 22.9 ± 6.4 ms (62.2 ± 7.5 %; n = 35), $\tau_{2,inact}$ was 107 ± 25 ms (22.5 ± 3.8 %) and $\tau_{3,inact}$ was 507 ± 57ms (15.3 ± 3.8 %). Compared to Kv4.1 alone, co-expression with 1a modulated macroscopic inactivation by decreasing $\tau_{2,inact}$ to 87.4 ± 25.5 ms (52.5 ± 20.2 %; n = 30) and $\tau_{3,inact}$ to 405 ± 174 ms (2.5 ± 2.4 %), and increasing $\tau_{1,inact}$ to 41.9 ± 11.3 ms (44.9 ± 19.6 %). Co-expression with 1b also decreased $\tau_{2,inact}$ to 81.9 ± 25.6 ms (49 ± 1.3 %; n = 39) and $\tau_{3,inact}$ to 292 ± 103 ms (7.8 ± 2.5 %), accompanied with a higher contribution of the intermediate component and a reduced contribution of fast component

(43.2 ± 10.5 %; Table 4.2).

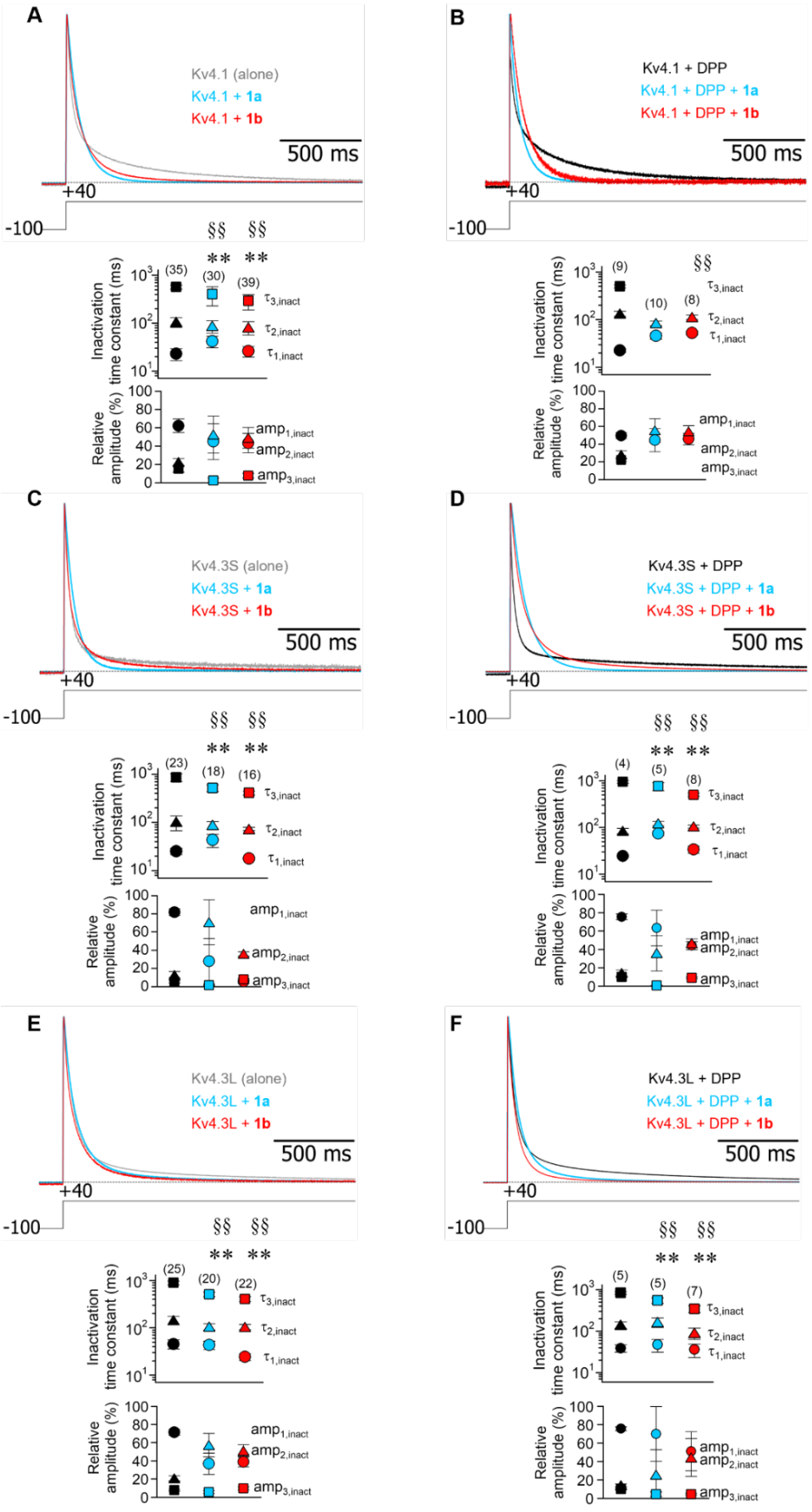

Figure 4.6 Modulation of other Kv4 channels macroscopic inactivation by KChIP1 splice variants. Kv4 channel macroscopic inactivation kinetics were studied using extended voltage pulses to +40 mV, and the time course of current decay was described by the sum of three exponential functions. Representative current traces and summary graphs are shown for Kv4.1 (**A, B**), Kv4.3S (**C, D**) and Kv4.3L (**E, F**). Currents were normalized to peak and superimposed to demonstrate the effects of KChIP1 splice variant co-expression on current decay kinetics in a binary (left) or a ternary (right) configuration; Kv4.x alone: grey traces; Kv4.x + DPP: black traces; co-expression with 1a: blue traces; co-expression with 1b: red traces. Inactivation time constants and their relative amplitudes ($\tau_{1,inact}$ and $amp_{1,inact}$: circles; $\tau_{2,inact}$ and $amp_{2,inact}$: triangles; $\tau_{3,inact}$ and $amp_{3,inact}$: squares) are presented as means ± SD below; number of oocytes (n) indicated. Significant differences of KChIP1 effects (compared to Kv4.x alone or Kv4.x + DPP) are indicated with * ($p<0.05$) or ** ($p<0.0001$; ANOVA). Significant differences seen with special features of the 1b splice variant (compared to 1a co-expression for comparable amounts of KChIP1 cRNA) are indicated with § ($p<0.05$) or §§ ($p<0.0001$; unpaired Student's *t*-test). Statistical significance symbols represent the highest degree of significance found in ≥ 1 of 6 parameters analysed (amount of injected cRNA and days of recording see Table 4.2,4.3,4.4).

The macroscopic inactivation of Kv4.1 + DPP was fitted with a triple-exponential function, while Kv4.1 + DPP + 1a or Kv4.1 + DPP + 1b was better fitted with a double-exponential function (Figure 4.6B). For Kv4.1 + DPP + 1a, $\tau_{1,inact}$ was 45.8 ± 6.5 ms (44.5 ± 13.2 %; n = 10), and $\tau_{2,inact}$ was 84.2 ± 9.9 ms (55.5 ± 13.2 %). In comparison, co-expression with 1b resulted in significantly larger time constants compared to Kv4.1 + DPP + 1a: $\tau_{1,inact}$ was 52.6 ± 5.1 ms (45.7 ± 6.5 %; n = 8), and $\tau_{2,inact}$ was 113 ± 12 ms (54.3 ± 6.5 %).

Kv4.3S macroscopic inactivation kinetics were well described by a triple-exponential function (Figure 4.6C), with the following time constants: $\tau_{1,inact}$ was 25.3 ± 3.8 ms (81.8 ± 3.7 %; n = 23), $\tau_{2,inact}$ was 103 ± 35.4 ms (12.9 ± 3.5 %) and $\tau_{3,inact}$ was 858 ± 156 ms (5.4 ± 1.4 %). Upon co-expression with 1a, $\tau_{1,inact}$ became significantly larger (43.1 ± 13.2 ms; 27.8 ± 24.9 %; n = 18), and $\tau_{2,inact}$ (88.5 ± 16.2 ms; 70.4 ± 24.7 %) and $\tau_{3,inact}$ (518 ± 82.4 ms; 1.4 ± 0.5 %) were decreased, compared to Kv4.3S alone (Table 4.3). The intermediate component accounted for the majority of the current decay. Co-expression of 1b decreased all the inactivation time constants, with less contribution of fast inactivation component (Table 4.3; $p<0.05$). For Kv4.3S + DPP, $\tau_{1,inact}$ was 24.6 ± 1.5 ms (75.6 ± 3.2 %; n = 4), $\tau_{2,inact}$ was 84.8 ± 10.8 ms (14.3 ± 3.3 %) and $\tau_{3,inact}$ was 949 ± 58.9 ms (10.1 ± 0.6 %). In the ternary configuration with DPP, both 1a and 1b increased $\tau_{1,inact}$ and $\tau_{2,inact}$, but decreased $\tau_{3,inact}$ of Kv4.3S (Figure 4.6D; Table 4.3), which was consistent with the typical KChIP effects of slowing inactivation.

For Kv4.3L alone, $\tau_{1,inact}$ was 45.6 ± 10 ms (71.5 ± 3.3 %; n = 25), $\tau_{2,inact}$ was 145 ± 29.3 ms (20.8 ± 2.7 %), and $\tau_{3,inact}$ was 892 ± 83 ms (7.7 ± 1.0 %). In the binary configuration, co-expression with 1a decreased $\tau_{2,inact}$ to 106 ± 10 ms (57.3 ± 12.8 %; n = 20) and $\tau_{3,inact}$ to 509 ± 57.3 ms (5.8 ± 1.5 %), accompanied by an increased contribution of the intermediate component. Similarly, co-expression with 1b significantly reduced all the time constants,

and increased the contribution of $\tau_{2,inact}$ (51.1 ± 6.8 %; Figure 4.6E; Table 4.4). For Kv4.3L + DPP, $\tau_{1,inact}$ was 39 ± 7.7 ms (75.7 ± 2.1 %; n = 5), $\tau_{2,inact}$ was 142 ± 26.3 ms (14.2 ± 1.6 %), and $\tau_{3,inact}$ was 840 ± 60.7 ms (10.1 ± 1.2 %). In the ternary configuration with DPP, 1a only reduced $\tau_{3,inact}$ to 551 ± 81.3 ms (4.5 ± 2.5 %; n = 5), accompanied by a decrease in its relative amplitude. In contrast, 1b co-expression significantly decreased $\tau_{2,inact}$ (90.5 ± 27.1 ms; 44.3 ± 20.6 %; n = 7) and $\tau_{3,inact}$ (346 ± 65 ms; 4.5 ± 1.0 %), while $\tau_{1,inact}$ remained unchanged (Figure 4.6F; Table 4.4). The currents of Kv4.3L + DPP + 1b inactivated faster than that of Kv4.3L + DPP + 1a, as both $\tau_{2,inact}$ and $\tau_{3,inact}$ were significantly smaller with 1b. Thus, 1a and 1b accelerated the macroscopic inactivation of Kv4.3L in absence and presence of DPP, which differed from the typical KChIP effects of slowing inactivation.

4.2.3 Kinetics of recovery from inactivation

The recovery from inactivation of Kv4.1 alone was described with a single-exponential function, with a recovery time constant (τ_{rec}) of 270 ± 93 ms (n = 10). Similar to the observations in Kv4.2, the recovery kinetics of Kv4.1 were fitted with a double-exponential function upon 1a or 1b co-expression. For Kv4.1 + 1a, $\tau_{1,rec}$ was 57.6 ± 17.3 ms (95.6 ± 1.8 %; n = 14) and $\tau_{2,rec}$ was 1300 ± 491 ms (4.4 ± 1.8 %), resulting in an overall acceleration of recovery. In contrast, co-expression with 1b resulted in a slower recovery process compared to Kv4.1. Both $\tau_{1,rec}$ (123 ± 31.4 ms; 73.3 ± 3.9 %; n = 12) and $\tau_{2,rec}$ (2979 ± 1661 ms; 26.7 ± 3.9 %) were also larger than those observed in Kv4.1 + 1a (Figure 4.7A; Table 4.2). DPP co-expression significantly decreased τ_{rec} of Kv4.1 (Kv4.1 + DPP) to 116 ± 21 ms (n = 7). In the ternary configuration with DPP, for Kv4.1 + DPP + 1a (Figure 4.7B), $\tau_{1,rec}$ was 48.2 ± 10.3 ms (89.5 ± 2.8 %; n = 12) and $\tau_{2,rec}$ was 1042 ± 521 ms (10.5 ± 2.8 %).

Figure 4.7 Modulation of other Kv4 channels recovery kinetics by KChIP1 splice variants. Recovery plots and summary graphs are shown for Kv4.1 (**A, B**), Kv4.3S (**C, D**) and Kv4.3L (**E, F**) in a binary (left) and a ternary configuration (right). Relative current amplitudes (I_{test} / $I_{control}$; error bars are SEM) were plotted against interpulse duration, and the data were described by exponential functions: A single-exponential function was used for the recovery kinetics of Kv4.x alone (grey) and Kv4.x + DPP (black), except for Kv4.3L alone, which required a double-exponential function. A double-exponential function was necessary for the recovery kinetics of Kv4.x + KChIP1 and Kv4.x + DPP + KChIP1 (1a: blue; 1b: red); Dotted lines: single-exponential functions fitted to apparently biphasic recovery data. Recovery time constants from single-exponential fits (τ_{rec}, diamonds) and time constants including their relative amplitudes from double-exponential fits ($\tau_{1,rec}$ and $amp_{1,rec}$: circles; $\tau_{2,rec}$ and $amp_{2,rec}$: triangles) are presented as means ± SD; number of oocytes (n) indicated. Significant differences of KChIP1 effects (compared to Kv4.x alone or Kv4.x + DPP) are indicated with * ($p<0.05$) or ** ($p<0.0001$; ANOVA). Significant differences seen with special features of the 1b splice variant (compared to 1a co-expression for comparable amounts of KChIP1 cRNA) are indicated with § ($p<0.05$) or §§ ($p<0.0001$; unpaired Student's *t*-test). Statistical significance symbols represent the highest degree of significance found in ≥ 1 of 4 parameters analyzed (amount of injected cRNA and days of recording see Table 4.2,4.3,4.4).

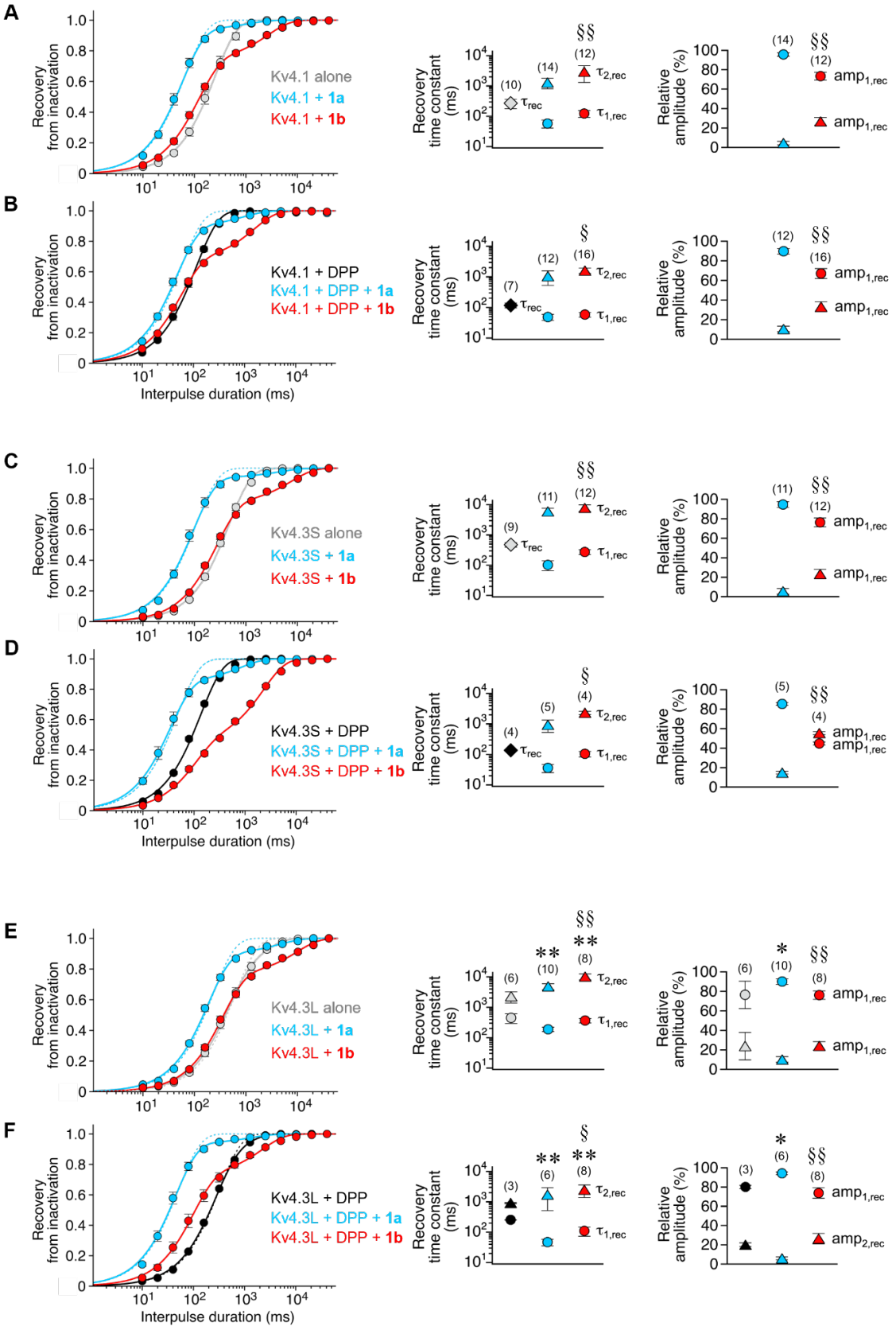

Similarly, for Kv4.1 + DPP + 1b, $\tau_{1,rec}$ was 58.0 ± 10.3 ms (66.9 ± 5.0 %; n = 16) and $\tau_{2,rec}$

was 1605 ± 311 ms (33.1 ± 5.0 %), which were both larger compared to those of Kv4.1 + DPP+ 1a (Figure 4.7B; Table 4.2), indicating the special 1b effect of slowing recovery is still present for Kv4.1 in a binary and a ternary configuration.

The recovery from inactivation of Kv4.3S alone and Kv4.3S + DPP was described with a single-exponential function and τ_{rec} obtained were 478 ± 82.3 ms (n = 9) and 136 ± 11 ms (n = 4), respectively. Upon co-expression with 1a or 1b, the recovery kinetics were better fitted with a double-exponential function, both in the absence and presence of DPP. For Kv4.3S + 1a, $\tau_{1,rec}$ was 102 ± 36.4 ms (94.5 ± 2.9 %; n = 11) and $\tau_{2,rec}$ was 5970 ± 1625 ms (5.5 ± 2.9 %). For Kv4.3S + 1b, $\tau_{1,rec}$ was 274 ± 47.6 ms (76.2 ± 4.6 %; n = 12) and $\tau_{2,rec}$ was 7826 ± 1931 ms (23.2 ± 4.6 %; Figure 4.7C). In the ternary configuration with DPP, for Kv4.3S + DPP + 1a, $\tau_{1,rec}$ was 35.7 ± 10.4 ms (85.2 ± 1.5 %; n = 5), and $\tau_{2,rec}$ was 930 ± 408 ms (14.8 ± 1.5 %). For Kv4.3S + DPP + 1b, $\tau_{1,rec}$ was 104 ± 21.9 ms (44.7 ± 1.5 %; n = 4) and $\tau_{2,rec}$ was 2309 ± 277 ms (55.3 ± 1.5 %; Figure 4.7D). Thus, 1b slowed the Kv4.3S recovery kinetics in the same manner as observed in Kv4.1 and Kv4.2.

Different from other Kv4 subtypes, recovery from inactivation of Kv4.3L alone, as well as Kv4.3L + 1a and Kv4.3L + 1b, was best described with a double-exponential function. For Kv4.3L alone, $\tau_{1,rec}$ was 448 ± 156 ms (76.3 ± 14.1 %; n = 6) and $\tau_{2,rec}$ was 2293 ± 905 ms (23.7 ± 14.1 %). Co-expression with 1a significantly decreased $\tau_{1,rec}$ to 189 ± 31.5 ms (89.9 ± 2.8 %; n = 10) compared to Kv4.3L alone, whereas $\tau_{2,rec}$ was increased to 4848 ± 1085 ms (10.1 ± 2.8 %), resulting in an acceleration of recovery kinetics (Figure 4.7E; Table 4.4). 1b slowed Kv4.3L recovery process, as $\tau_{2,rec}$ increased to 10158 ± 2237 ms (24.0 ± 4.3 %), approximately 5 times larger than that of Kv4.3L alone (Figure 4.7E; Table 4.4). Similarly, recovery from inactivation of Kv4.3L + DPP, Kv4.3L + DPP + 1a, and Kv4.3L + DPP + 1b was best described by a double-exponential function. In the ternary configuration with DPP, 1a co-expression accelerated recovery by significantly decreasing the fast recovery time constant, while 1b slowed the recovery by increasing both fast and slow time constants (Figure 4.7F; Table 4.4).

In summary, 1a and 1b modulate recovery from inactivation of other Kv4 channel subtypes (Kv4.1, Kv4.3S, and Kv4.3L) in a similar manner to that observed in Kv4.2.

4.2.4 Voltage dependence of activation and steady-state inactivation

The pulses protocols applied to determine the voltage dependences of activation and steady-state inactivation were the same as described in Chapter 4.1.4.

For Kv4.1 alone, Boltzmann analysis yielded voltages of -6.1 ± 2.1 mV (s_{act} was 25.7 ± 2.2 mV; n = 8) and -63.4 ± 2.6 mV (s_{inact} was 6.2 ± 1.2; n = 15) for voltage of halfmaximal activation ($V_{1/2,act}$) and halfmaximal inactivation ($V_{1/2,inact}$), respectively, including slope factors. In the binary configuration, upon co-expression with 1a, $V_{1/2,act}$ was -9.0 ± 4.5 mV (n = 15), which was not significantly different from Kv4.1 alone. In contrast, 1b co-expression shifted $V_{1/2,act}$ to -14.2 ± 3.2 mV (n = 11), which was more negative compared to Kv4.1 alone and Kv4.1 + 1a (Figure 4.8A). Both 1a and 1b co-expression significantly decreased the slope factors of activation curves (Figure 4.8A; Table 4.2). Regarding the modulation of steady-state inactivation, 1a and 1b exerted opposite effects on Kv4.1 channels. Co-expression with 1a caused a positive shift of $V_{1/2,inact}$ to -55.2 ± 2.4 mV, accompanied by a smaller s_{inact} of 5.0 ± 1.2 mV (n = 16), compared to Kv4.1. However, 1b shifted $V_{1/2,inact}$ to a more negative potential (-68.0 ± 2.5 mV; n = 11; Figure 4.8A). For Kv4.1 + DPP, Boltzmann analysis yielded a $V_{1/2,act}$ of -19.6 ± 5.6 mV with an s_{act} of 27.8 ± 2.9 mV (n = 6), and a $V_{1/2,inact}$ of -73.2 ± 3.9 mV with an s_{inact} of 8.3 ± 1.5 (n = 9). In the ternary configuration with DPP, co-expression with 1a or 1b induced no significant effect on either $V_{1/2,act}$ or s_{act} (Figure 4.8B; Table 4.2). On the other hand, 1a induced a positive shift of $V_{1/2,inact}$ to -66.7 ± 5.5 (n = 11), compared to Kv4.1 + DPP. For Kv4.1 + DPP + 1b, $V_{1/2,inact}$ (-76.9 ± 2.2 mV; n = 14) was not different from Kv4.1 + DPP, but was significantly more negative compared to Kv4.1 + DPP + 1a.

For Kv4.3S alone, Boltzmann analysis yielded a $V_{1/2,act}$ of 1.2 ± 4.3 mV with a slope factor of 28.3 ± 1.5 mV (n = 12), and a $V_{1/2,inact}$ of –63.9 ± 1.0 mV with a slope factor of 4.0 ± 0.2 mV (n = 8). In the binary configuration, both 1a and 1b shifted the $V_{1/2,act}$ to more hyperpolarized potentials and reduced the s_{act} (Figure 4.8C; Table 4.3). Furthermore, 1a co-expression positively shifted $V_{1/2,inact}$ to -58.0 ± 4.6 mV (n = 15), while 1b had no significant effect on $V_{1/2,inact}$ (-66.3 ± 2.9 mV), but increased the s_{inact} to 4.5 ± 0.7 (n = 14), compared to Kv4.3S (Figure 4.8C; Table 4.3). As shown in Figure 4.8D, for Kv4.3S + DPP, Boltzmann analysis yielded a $V_{1/2,act}$ of –24.0 ± 4.4 mV with a slope factor of 24.3 ± 0.4 mV (n = 4), and a $V_{1/2,inact}$ of –68.7 ± 2.6 mV with a slope factor of 4.1 ± 0.3 mV (n = 4). In the ternary configuration with DPP, co-expression with both 1a and 1b decreased the s_{act}, without affecting $V_{1/2,act}$ (Table 4.3). Regarding steady-state inactivation, 1a reduced the s_{inact} to 3.4 ± 0.3 mV (n = 5), while 1b significantly shifted $V_{1/2,inact}$ to -77.1 ± 1.0 mV with an s_{inact} of 4.0 ± 0.2 mV (n = 5). In summary, for Kv4.3S, 1a modulated the voltage dependence of activation and inactivation only in the binary complex, while 1b shifted the $V_{1/2,inact}$ in the

presence of DPP.

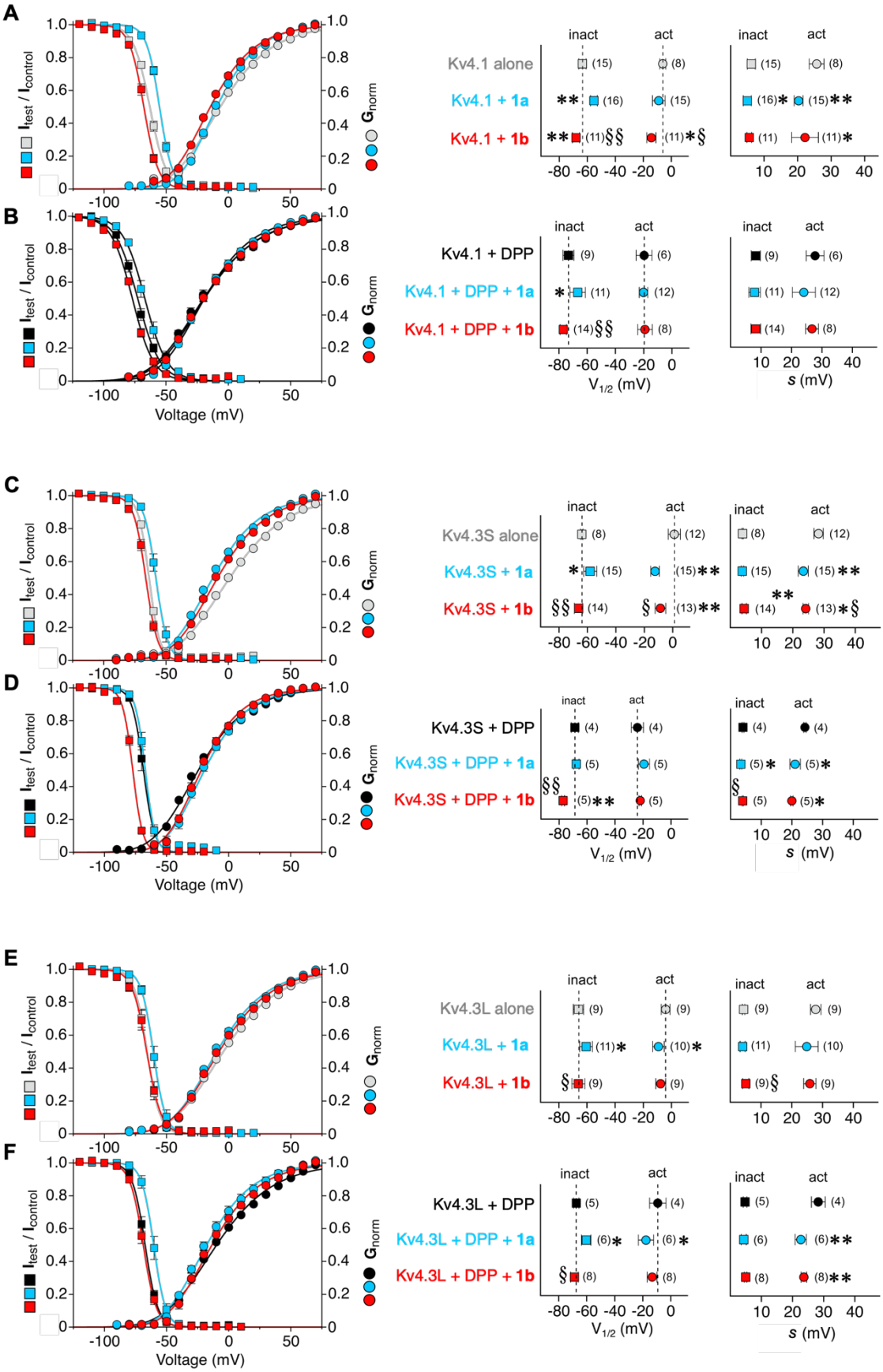

Figure 4.8 Effects of KChIP1 splice variants on the voltage dependences of other Kv4 channels. The voltage dependences of activation and steady-state inactivation were measured. Activation and inactivation curves, and summary graphs are shown for Kv4.1 (**A, B**), Kv4.3S (**C, D**) and Kv4.3L (**E, F**). Normalized data (I_{test} / $I_{control}$) from steady-state inactivation protocols and normalized conductance values (G_{norm}) from activation protocols were plotted against conditioning and test pulse voltage, respectively, in the same graph (error bars are SEM); upper graphs: Kv4.x alone (grey) and binary channels with 1a (blue) or 1b (red); lower graphs: Kv4.2 + DPP (black) and ternary channels with 1a (blue) or 1b (red). Voltages of halfmaximal activation (act, circles) and inactivation (inact, squares) and corresponding slope factors ($V_{1/2}$ and *s*, respectively) from Boltzmann-analysis are presented as mean ± SD; numbers of oocytes (n) indicated. Grey symbols: Kv4.x alone; black symbols: Kv4.x + DPP; blue symbols: Kv4.x + 1a or Kv4.x + DPP + 1a; red symbols: Kv4.x + 1b or Kv4.x + DPP + 1b. Significant differences of KChIP1 effects (compared to Kv4.x alone or Kv4.x + DPP) are indicated with * ($p<0.05$) or ** ($p<0.0001$; ANOVA). Significant differences seen due to special features of the 1b splice variant (compared to 1a co-expression for comparable amounts of KChIP1 cRNA) are indicated with § ($p<0.05$) or §§ ($p<0.0001$; unpaired Student's *t*-test; amount of injected cRNA and days of recording see Table 4.2,4.3,4.4).

As shown in Figure 4.8E, for Kv4.3L alone, Boltzmann analysis yielded a $V_{1/2,act}$ of –4.1 ± 3.1 mV with a slope factor of 27.8 ± 1.7 mV (n = 9), and a $V_{1/2,inact}$ of –66.0 ± 3.7 mV with a slope factor of 4.4 ± 0.4 (n = 9). In the binary configuration, co-expression with 1a negatively shifted the $V_{1/2,act}$ to -9.2 ± 4.1 mV (s_{act} of 24.9 ± 3.7; n = 10), and also positively shifted $V_{1/2,inact}$ to -60.6 ± 4.5mV (s_{inact} of 4.1 ± 0.8; n = 11). In contrast, 1b had no significant effect on either activation or inactivation parameters (Figure 4.8E; Table 4.4). For Kv4.3L + DPP, Boltzmann analysis yielded a $V_{1/2,act}$ of –9.2 ± 5.9 mV with a slope factor of 28.3 ± 2.2 mV (n = 4), and a $V_{1/2,inact}$ of –67.4 ± 1.9 mV with a slope factor of 4.8 ± 0.6 (n = 5). In the ternary configuration with DPP, co-expression with 1a shifted the $V_{1/2,act}$ to –17.6 ± 5.4 mV with a reduced s_{act} of 22.7 ± 1.8 mV (n = 6), and positively shifted the $V_{1/2,inact}$ to –60.3 ± 3.4 mV (n = 6), compared to Kv4.3L + DPP. In contrast, 1b neither modulated activation nor steady-state inactivation of Kv4.3L channel in a ternary configuration (Figure 4.8F; Table 4.4).

Table 4.2 Functional characterization of Kv4.1 in the absence and presence of KChIP1 splice variants 1a and 1b in different channel configurations.

configuration (ng, *day*)	I (+40) (µA)	$\tau_{1,inact}$ (ms)	$amp_{1,inact}$ (%)	$\tau_{2,inact}$ (ms)	$amp_{2,inact}$ (%)	$\tau_{3,inact}$ (ms)	$amp_{3,inact}$ (%)	$\tau_{1,rec}/\tau_{rec}$ (ms)	$amp_{1,rec}$ (%)	$\tau_{2,rec}$ (ms)	$amp_{2,rec}$ (%)	$V_{1/2,act}$ (mV)	s_{act} (mV)	$V_{1/2,inact}$ (mV)	s_{inact} (mV)
Kv4.1 alone (5, *d2-d3*)	-	22.9 ± 6.4 (35)	62.2 ± 7.5 (35)	107 ± 25 (35)	22.5 ± 3.8 (35)	570 ± 57 (35)	15.3 ± 3.8 (35)	270 ± 93 (10)	-			-6.1 ± 2.1 (8)	25.7 ± 2.2 (8)	-63.4 ± 2.6 (15)	6.2 ± 1.2 (15)
Kv4.1 alone (1.7, *d2*)	1.1 ± 0.5 (8)	-													
Kv4.1 + 1a (1.7+10, *d2*)	9.5 ± 3.1^{kk} (33)	41.9 ± 11.3^{kk} (30)	44.9 ± 19.6^{kk} (30)	87.4 ± 25.5^{k} (30)	52.5 ± 20.2^{kk} (30)	405 ± 174^{kk} (30)	2.5 ± 2.4^{kk} (30)	57.6 ± 17.3 (14)	95.6 ± 1.8 (14)	1300 ± 491 (14)	4.4 ± 1.8 (14)	-9.0 ± 4.5 (15)	20.3 ± 1.3^{kk} (15)	-55.2 ± 2.4^{kk} (16)	5.0 ± 1.2^{k} (16)
Kv4.1 + 1a (1.7+10, *d3*)	-											-			
Kv4.1 + 1b (1.7+10, *d2*)	4.0 ± 1.6^{k,bb} (32)	26.0 ± 6.4^{bb} (39)	43.2 ± 10.5^{kk} (39)	81.9 ± 25.6^{k} (39)	49.0 ± 11.3^{kk} (39)	292 ± 103^{kk,b} (39)	7.8 ± 2.5^{kk,b} (39)	123 ± 31.4^{bb} (12)	73.3 ± 3.9^{bb} (12)	2979 ± 1661^{bb} (12)	26.7 ± 3.9^{bb} (12)	-14.2 ± 3.2^{k,b} (11)	22.2 ± 4.0^{k} (11)	-68.0 ± 2.5^{kk,bb} (11)	5.6 ± 0.7 (11)
Kv4.1 + 1b (1.7+10, *d3*)	-														
Kv4.1 + DPP (1.7+5, *d1*)	4.4 ± 1.0 (9)	22.7 ± 2.2 (9)	48.4 ± 1.7 (9)	134 ± 16 (9)	23.9 ± 1.7 (9)	498 ± 37 (9)	27.7 ± 2.1 (9)	116 ± 21 (7)	-			-19.6 ± 5.6 (6)	27.8 ± 2.9 (6)	-73.2 ± 3.9 (9)	8.3 ± 1.5 (9)
Kv4.1 + DPP (1.7+5, *d2*)	19.4 ± 5.4 (17)	-													
Kv4.1 + DPP + 1a (1.7+5+10, *d1*)	6.9 ± 1.2^{tt} (10)	45.8 ± 6.6 (10)	44.5 ± 13.2 (10)	84.2 ± 9.9 (10)	55.5 ± 13.2 (10)	-		48.2 ± 10.3 (12)	89.5 ± 2.8 (12)	1042 ± 521 (12)	10.5 ± 2.8 (12)	-20.1 ± 3.0 (12)	24.1 ± 3.8 (12)	-66.7 ± 5.5^{t} (11)	7.9 ± 1.9 (11)
Kv4.1 + DPP + 1a (1.7+5+10, *d2*)	20.3 ± 3.7 (9)	-													
Kv4.1 + DPP + 1b (1.7+5+10, *d1*)	4.1 ± 1.0^{bb} (8)	52.6 ± 5.1^{b} (8)	45.7 ± 6.5 (8)	113 ± 12^{bb} (8)	54.3 ± 6.5 (8)	-		58.0 ± 10.3^{b} (16)	66.9 ± 5.0^{bb} (16)	1605 ± 311^{b} (16)	33.1 ± 5.0^{bb} (16)	-19.0 ± 5.1 (8)	26.8 ± 2.1 (8)	-76.9 ± 2.2^{bb} (14)	8.3 ± 1.6 (14)
Kv4.1 + DPP + 1b (1.7+5+10, *d2*)	14.6 ± 3.0^{t,b} (10)	-													
Kv4.1 + DPP + 1b (1.7+5+10, *d5*)	-														

Kv4.1 was expressed alone or in different channel configurations (i.e., in the absence or presence of DPP) with either KChIP1a (1a) or KChIP1b (1b) in *Xenopus* oocytes (cRNA amounts in ng per oocyte indicated). Functional characterization under two-electrode voltage-clamp was performed on day 1 - 5 after cRNA injection (as indicated; *d1 - d5*). Mean values ± SD and number of oocytes (n) are given for the peak current amplitude, the time constants of macroscopic inactivation and recovery from inactivation (including relative amplitudes in %), and the voltages of halfmaximal activation and steady-state inactivation (including slope factors, *s*). Statistical analyses were done using one-way analysis of variance (ANOVA) with Dunnett's post hoc testing for more than two groups and an unpaired Student's *t*-test for two groups. Superscript letters k, b and t denote significant differences; single letter: $p<0.05$; two letters: $p<0.0001$; k, kk: significantly different from Kv4.1 alone (KChIP effect, binary); b, bb: significantly different from 1a co-expression (special feature of the 1b splice variant); t,tt: significantly different from Kv4.1 + DPP (KChIP effect in the presence of DPP, ternary).

Table 4.3 Functional characterization of Kv4.3S in the absence and presence of KChIP1 splice variants 1a and 1b in different channel configurations.

configuration (ng, *day*)	I (+40) (µA)	$\tau_{1,inact}$ (ms)	$amp_{1,inact}$ (%)	$\tau_{2,inact}$ (ms)	$amp_{2,inact}$ (%)	$\tau_{3,inact}$ (ms)	$amp_{3,inact}$ (%)	$\tau_{1,rec}/\tau_{rec}$ (ms)	$amp_{1,rec}$ (%)	$\tau_{2,rec}$ (ms)	$amp_{2,rec}$ (%)	$V_{1/2,act}$ (mV)	s_{act} (mV)	$V_{1/2,inact}$ (mV)	s_{inact} (mV)
Kv4.3S alone (0.8, *d2*)	2.6 ± 1.2 (25)	25.3 ± 3.8 (23)	81.8 ± 3.7 (23)	103 ± 35.4 (23)	12.9 ± 3.5 (23)	858 ± 156 (23)	5.4 ± 1.4 (23)	-							
Kv4.3S alone (1.7, *d2*)								478 ± 82.3 (9)	-			1.2 ± 4.3 (12)	28.3 ± 1.5 (12)	-63.9 ± 1.0 (8)	4.0 ± 0.2 (8)
Kv4.3S + 1a (0.8+5, d2)	17.3 ± 4.4^{kk} (22)	43.1 ± 13.2^{kk} (18)	27.8 ± 24.9^{kk} (18)	88.5 ± 16.2 (18)	70.7 ± 24.7^{kk} (18)	518 ± 82.4^{kk} (18)	1.4 ± 0.5^{kk} (18)	-							
Kv4.3S + 1a (1.7+10, *d2*)								102 ± 36.4 (11)	94.5 ± 2.9 (11)	5970 ± 1625 (11)	5.5 ± 2.9 (11)	-12.4 ± 3.0^{kk} (15)	23.4 ± 1.6^{kk} (15)	-58.0 ± 4.6^{k} (15)	3.9 ± 0.4 (15)
Kv4.3S + 1b (0.8+5, *d2*)	6.2 ± 1.7^{k,bb} (16)	17.8 ± 1.2^{k,bb} (16)	56.2 ± 2.1^{kk,b} (16)	73.1 ± 5.4^{k,b} (16)	35.8 ± 2.5^{kk,bb} (16)	408 ± 36.9^{kk,bb} (16)	8.1 ± 0.8^{kk,bb} (16)	-							
Kv4.3S + 1b (1.7+10, *d2*)								274 ± 47.6^{bb} (12)	76.2 ± 4.6^{bb} (12)	7826 ± 1931^{b} (12)	23.3 ± 4.6^{bb} (12)	-8.6 ± 3.7^{kk,b} (13)	24.2 ± 0.9^{kk} (13)	-66.3 ± 2.9^{bb} (14)	4.5 ± 0.7^{k,b} (14)
Kv4.3S + DPP (1.7+5, *d1*)	16.7 ± 3.9 (7)	-													
Kv4.3S + DPP (1.7+5, *d2*)	38.9 ± 12.0 (8)														
Kv4.3S + DPP (0.8+2.5, *d2*)	-	24.6 ± 1.5 (4)	75.6 ± 3.2 (4)	84.8 ± 10.8 (4)	14.3 ± 3.3 (4)	949 ± 58.9 (4)	10.1 ± 0.6 (4)	136 ± 11.0 (4)	-			-24.0 ± 4.4 (4)	24.3 ± 0.4 (4)	-68.7 ± 2.6 (4)	4.1 ± 0.3 (4)
Kv4.3S + DPP + 1a (1.7+5+10, *d1*)	23.3 ± 5.8^{t} (5)	74.3 ± 7.1^{tt} (5)	63.4 ± 19.4 (5)	122 ± 13.4^{t} (5)	35.8 ± 19.3^{t} (5)	764 ± 148^{t} (5)	0.7 ± 0.2^{tt} (5)	-							
Kv4.3S + DPP + 1a (1.7+5+10, *d2*)	54.9 ± 15.8^{t} (4)	-													
Kv4.3S + DPP + 1a (0.8+2.5+5, *d2*)	-							35.7 ± 10.4 (5)	85.2 ± 1.5 (5)	930 ± 408 (5)	14.8 ± 1.5 (5)	-19.3 ± 4.0 (5)	21.1 ± 1.7^{t} (5)	-67.7 ± 2.0 (5)	3.4 ± 0.3^{t} (5)
Kv4.3S + DPP + 1b (1.7+5+10, *d1*)	10.0 ± 2.1^{t,b} (7)	-						-							
Kv4.3S + DPP + 1b (1.7+5+10, *d2*)	23.7 ± 5.4^{t,b} (8)	34.1 ± 6.1^{t,bb} (8)	44.2 ± 4.4^{t} (8)	105 ± 8.1^{t,b} (8)	46.7 ± 4.9^{t} (8)	501 ± 35.8^{tt,b} (8)	9.1 ± 1.0 (8)	-							
Kv4.3S + DPP + 1b (0.8+2.5+5, *d2*)	-							104 ± 21.9^{b} (4)	44.7 ± 1.5^{bb} (4)	2309 ± 277^{b} (4)	55.3 ± 1.5^{bb} (4)	-21.9 ± 1.0 (5)	20.0 ± 0.4^{t} (5)	-77.1 ± 1.0^{tt,bb} (5)	4.0 ± 0.2^{b} (5)

Kv4.3S (short splice variant) was expressed alone or in different channel configurations (i.e., in the absence or presence of DPP) with either KChIP1a (1a) or KChIP1b (1b) in *Xenopus* oocytes (cRNA amounts in ng per oocyte indicated). Functional characterization under two-electrode voltage-clamp was performed on day 1 - 2 after cRNA injection (as indicated; *d1 - d2*). Mean values ± SD and number oocytes (n) are given for the peak current amplitude, the time constants of macroscopic inactivation and recovery from inactivation (including relative amplitudes in %), and the voltages of halfmaximal activation and inactivation (including slope factors, *s*). Statistical analyses were done using one-way analysis of variance (ANOVA) with Dunnett's post hoc testing for more than two groups and an unpaired Student's *t*-test for two groups. Superscript letters k, b and t denote significant differences; single letter: $p<0.05$; two letters: $p<0.0001$; k, kk: significantly different from Kv4.3S alone (KChIP effect, binary); b, bb: significantly different from 1a co-expression (special feature of the 1b splice variant); t,tt: significantly different from Kv4.3S + DPP (KChIP effect in the presence of DPP, ternary).

Table 4.4 Functional characterization of Kv4.3L in the absence and presence of KChIP1 splice variants 1a and 1b in different channel configurations.

Kv4.x configuration (ng cRNA, *day*)	I (+40) (µA)	$\tau_{1,inact}$ (ms)	$amp_{1,inact}$ (%)	$\tau_{2,inact}$ (ms)	$amp_{2,inact}$ (%)	$\tau_{3,inact}$ (ms)	$amp_{3,inact}$ (%)	$\tau_{1,rec}$ (ms)	$amp_{1,rec}$ (%)	$\tau_{2,rec}$ (ms)	$amp_{2,rec}$ (%)	$V_{1/2,act}$ (mV)	s_{act} (mV)	$V_{1/2,inact}$ (mV)	s_{inact} (mV)
Kv4.3L alone (1.7, *d2*)	17.2 ± 8.9 (25)	45.6 ± 10.0 (25)	71.5 ± 3.3 (25)	145 ± 29.3 (25)	20.8 ± 2.7 (25)	892 ± 83.0 (25)	7.7 ± 1 (25)	448 ± 156 (6)	76.3 ± 14.1 (6)	2294 ± 905 (6)	23.7 ± 14.1 (6)	-4.1 ± 3.1 (9)	27.8 ± 1.7 (9)	-66.0 ± 3.7 (9)	4.4 ± 0.4 (9)
Kv4.3L + 1a (1.7+10, *d2*)	15.2 ± 12.2 (18)	43.6 ± 8.7 (20)	36.9 ± 11.7^{kk} (20)	106 ± 16.4^{kk} (20)	57.3 ± 12.8^{kk} (20)	509 ± 57.3^{kk} (20)	5.8 ± 1.5^{kk} (20)	189 ± 31.5^{kk} (10)	89.9 ± 2.8^{k} (10)	4848 ± 1085^{k} (10)	10.1 ± 2.8^{k} (10)	-9.2 ± 4.1^{k} (10)	24.9 ± 3.7 (10)	-60.6 ± 4.5^{k} (11)	4.1 ± 0.8 (11)
Kv4.3L + 1b (1.7+10, *d2*)	3.5 ± 1.6^{kk,bb} (13)	24.3 ± 4.0^{kk,bb} (22)	39.1 ± 5.8^{kk} (22)	105 ± 13.2^{kk} (22)	51.1 ± 6.8^{kk} (22)	406 ± 50.1^{kk,bb} (22)	9.8 ± 1.6^{kk,bb} (22)	363 ± 60.3^{bb} (8)	76 ± 4.3^{bb} (8)	10158 ± 2237^{kk,bb} (8)	24 ± 4.3^{bb} (8)	-7.6 ± 3.5 (9)	25.9 ± 2.0 (9)	-66.1 ± 4.6^{b} (9)	5.1 ± 1.0^{b} (9)
Kv4.3L + 1b (1.7+10, *d3*)	-														
Kv4.3L + DPP (1.7+5, *d1*)	10.6 ± 5.9 (10)	-													
Kv4.3L + DPP (1.7+5, *d2*)	21.5 ± 5.9 (8)														
Kv4.3L + DPP (0.8+2.5, *d2*)	-	39.0 ± 7.7 (5)	75.7 ± 2.1 (5)	142 ± 26.3 (5)	14.2 ± 1.6 (5)	840 ± 60.7 (5)	10.1 ± 1.2 (5)	253 ± 5.2 (3)	79.9 ± 1.9 (3)	912 ± 28.3 (3)	20.1 ± 1.9 (3)	-9.2 ± 5.9 (4)	28.3 ± 2.2 (4)	-67.4 ± 1.9 (5)	4.8 ± 0.6 (5)
Kv4.3L + DPP (0.8+2.5, *d3*)								-							
Kv4.3L + DPP + 1a (1.7+5+10, *d1*)	11.7 ± 7.2 (7)	-													
Kv4.3L + DPP6 + 1a (1.7+5+10, *d2*)	33.7 ± 11.2^{t} (4)														
Kv4.3L + DPP + 1a (0.8+2.5+5, *d2*)	-	47.3 ± 16.3 (5)	70 ± 29.7 (5)	166 ± 43.5 (5)	25.5 ± 27.3 (5)	551 ± 81.3^{tt} (5)	4.5 ± 2.5^{t} (5)	46.7 ± 11.4^{tt} (6)	94.1 ± 1.5^{t} (6)	1709 ± 1193 (6)	5.9 ± 1.5^{t} (6)	-17.6 ± 5.4^{t} (6)	22.7 ± 1.8^{tt} (6)	-60.3 ± 3.4^{t} (6)	4.4 ± 0.8 (6)
Kv4.3L + DPP + 1a (0.8+2.5+5, *d3*)															
Kv4.3L + DPP + 1b (1.7+5+10, *d1*)	3.0 ± 1.5^{t,b} (5)	-													
Kv4.3L + DPP + 1b (1.7+5+10, *d2*)	15.1 ± 3.7^{b} (8)														
Kv4.3L + DPP + 1b (0.8+2.5+5, *d2*)	-	36.0 ± 12.9 (7)	51.2 ± 21.2 (7)	90.5 ± 27.1^{t,b} (7)	44.3 ± 20.6^{t} (7)	346 ± 65.0^{tt,b} (7)	4.5 ± 1^{tt} (7)	110 ± 37.3^{tt,b} (8)	73.7 ± 5.4^{bb} (8)	2482 ± 1098 (8)	26.3 ± 5.4^{bb} (8)	-13.2 ± 3.5 (8)	23.7 ± 0.9^{tt} (8)	-68.7 ± 2.8^{b} (8)	5.0 ± 0.4 (8)

Kv4.3L (long splice variant) was expressed alone or in different channel configurations (i.e., in the absence or presence of DPP) with either KChIP1a (1a) or KChIP1b (1b) in *Xenopus* oocytes (cRNA amounts in ng per oocyte indicated). Functional characterization under two-electrode voltage-clamp was performed on days 1 - 3 after cRNA injection (as indicated; *d1* - *d3*). Mean values ± SD and number of oocytes (n) are given for the peak current amplitude, the time constants of macroscopic inactivation and recovery from inactivation (including relative amplitudes in %), and the voltages of halfmaximal activation and inactivation (including slope factors, *s*). Statistical analyses were done using one-way analysis of variance (ANOVA) with Dunnett's post hoc testing for more than two groups and an unpaired Student's *t*-test for two groups. Superscript letters k, b and t denote significant differences; single letter: $p<0.05$; two letters: $p<0.0001$; k, kk: significantly different from Kv4.3L alone (KChIP effect, binary); b, bb: significantly different from 1a co-expression (special feature of the 1b splice variant); t,tt: significantly different from Kv4.3L + DPP (KChIP effect in the presence of DPP, ternary).

4.3 Mechanism of KChIP1b-mediated recovery kinetics

By analyzing the modulation of all Kv4 channel subtypes by two splice variants of KChIP1, we noticed that special 1b effects of inducing a second, extremely slow recovery component, thereby slowing the overall recovery process were reproducible for all Kv4 channel subtypes in the absence and presence of DPP, which was noted as a unique feature on recovery kinetics compared to other KChIPs. In this chapter, the mechanism of special 1b-mediated recovery kinetics was investigated in the presence of DPP.

4.3.1 General features of KChIP1b-mediated recovery kinetics studied in ternary Kv4.2 + DPP + 1b channels

As 1b modulated recovery kinetics of Kv4 channel subtypes in the same manner, here we used Kv4.2 as an example to investigate the specificities of KChIP1b-mediated recovery kinetics in the ternary configuration Kv4.2 + DPP + 1b (1.7 + 5 + 10 ng per oocyte).

4.3.1.1 Voltage dependence of recovery from high- and low-voltage inactivation

Previous research carried out on Kv4.2 channels alone indicated that the recovery from inactivation is strongly voltage dependent, being faster at more negative potentials (Bähring et al., 2001a). Here, we applied different double-pulse recovery protocols to investigate the voltage dependence of recovery from inactivation in the ternary configuration (Kv4.2 + DPP + 1b), and to find out whether recovery time constants ($\tau_{1,rec}$ and $\tau_{2,rec}$) have different voltage dependences. First, we measured the voltage dependence of recovery from high-voltage inactivation (+40 mV) of Kv4.2 + DPP + 1b. Recovery current traces from the same oocyte, obtained with recovery potentials of -120 and -90 mV, are shown (Figure 4.9A). It can be noticed that the maximum currents obtained with a recovery potential of -120 mV were larger than with -90 mV, and the time of test currents to saturate a stable state was faster at -120 mV than at -90 mV. Normalized data ($I_{test}/I_{control}$) at different recovery potentials (-120, -110, -100, -90 and -80 mV) were plotted against the interpulse duration on a log-scale (Figure 4.9C). With all recovery potentials tested, biphasic kinetics were observed, and recovery proceeded faster at more negative recovery potentials (Table 4.5). As the recovery was measured at -120 mV, $\tau_{1,rec}$ was 13.7 ± 2.1 ms (50.0 ± 9.8 %; n = 10) and $\tau_{2,rec}$ was 423 ± 64.2 ms (50.0 ± 9.8 %), which were significantly faster compared to the recovery time constants at -90 mV ($\tau_{1,rec}$ = 29.3 ± 5.6 ms; $\tau_{2,rec}$ = 900 ± 98.1 ms; n = 5). The voltage dependence of recovery was shallow with similar apparent charge values (q_{app}) of 0.65 and

0.53 for the first and second recovery time constant, respectively.

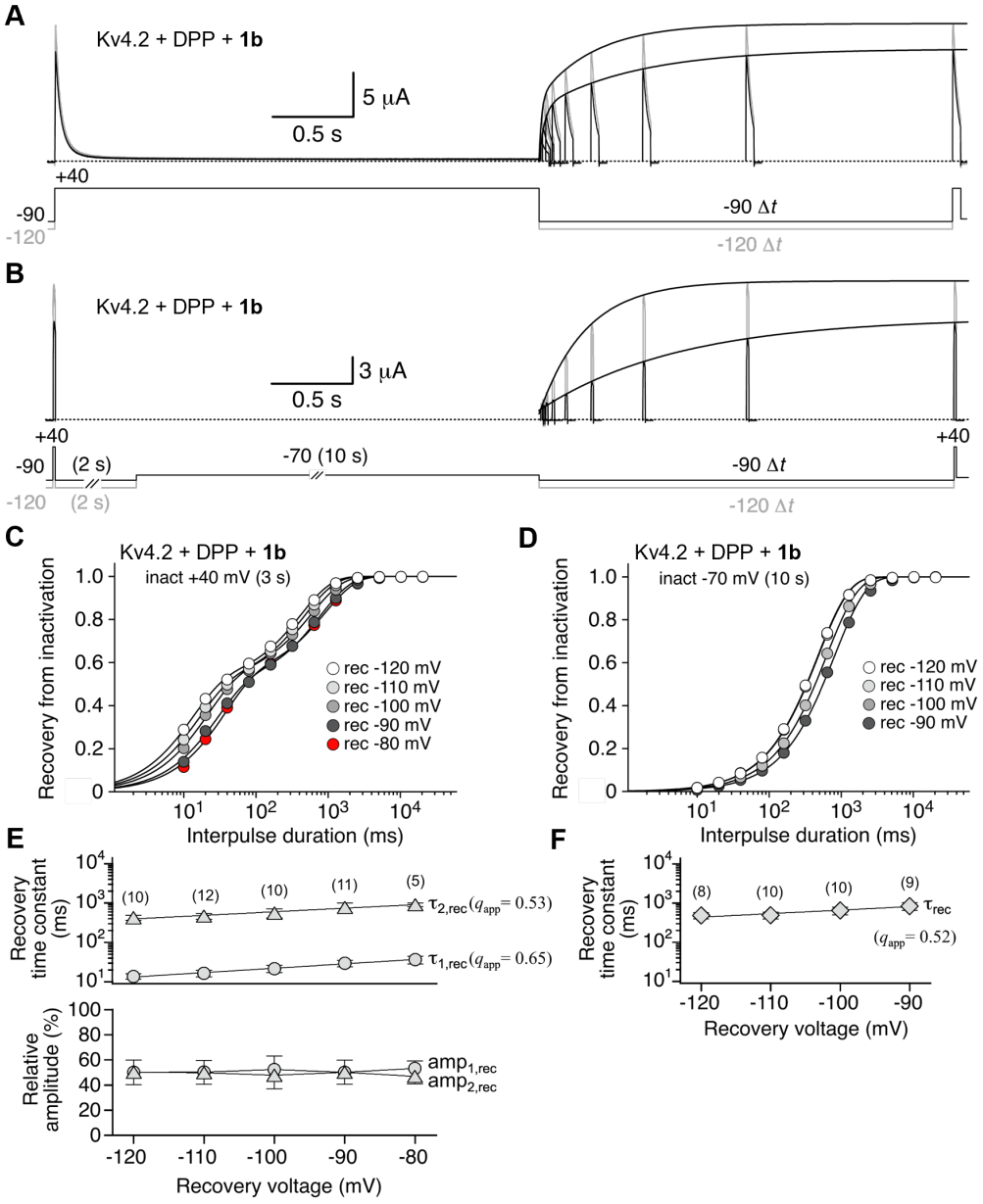

Figure 4.9 Kinetics of voltage dependence of recovery from high- and low-voltage inactivation in ternary Kv4.2 + DPP + 1b configuration. A: Recovery from inactivation with the same oocyte was measured using a double-pulse protocol with long control (3 s) and brief test pulses to +40 mV and variable interpulse durations at −120 and -90 mV (Δt, see inset). The maximum currents obtained with recovery potential at -120 mV were larger than that with -90 mV. B: Brief control and test current were recorded at +40 mV with a specialized double-pulse protocol, in which inactivation was induced at -70 mV (10 s) and recovery from inactivation was measured after variable interpulse durations at −120 and -90 mV (Δt, see inset), with the same oocyte. C: Recovery kinetics were described by a double exponential function (recovery potentials at -120, -110, -100, -90 and -80 mV). Recovery time constants and relative amplitudes of each time constant ($\tau_{1,rec}$ and $amp_{1,rec}$: circles, $\tau_{2,rec}$ and $amp_{2,rec}$: triangles) are plotted below. D: Recovery kinetics were described by a single exponential function when inactivation was induced at -70 mV (recovery potential at -120, -110, -100 and -90 mV). Recovery time constants (τ_{rec}: diamond) are plotted below (mean ± SD); numbers of oocytes indicated (n). Kv4.2 + DPP + 1b (1.7 + 5 + 10, ng per oocyte), measurement carried out on two days after cRNA injection.

At all recovery potentials the two recovery time constants accounted for roughly equal fractions of the total recovery process, which indicated that the contribution of the slow recovery component could not be affected by the hyperpolarization.

In a standard double-pulse protocol described above, inactivation is induced with a long and high voltage pulse (+40 mV for 3 s), so that most of the channels visit the open state before reaching the inactivated state. Since Kv4.2 channels exhibit preferential CSI as shown in Figure 2.5, we intended to measure a recovery process of Kv4.2 co-expressed with 1b in the presence of DPP, in which inactivation was induced at a low voltage, below the activation threshold (-70 mV for 10 s), in order to transit the channels directly into a closed-inactivated state without channel opening and then measure recovery from this state. Currents of recovery from such low-voltage inactivation at -70 mV, in which recovery potentials were -120 and -90 mV, were recorded after variable interpulse durations (Δt, see inset; Figure 4.9B). Similarly, it can be noticed that the maximum currents obtained with a recovery potential of -120 mV were larger than of -90 mV. Normalized data ($I_{test}/I_{control}$) at different recovery potentials (-120, -110, -100, and -90 mV) were plotted against the interpulse duration on a log-scale (Figure 4.9D). Surprisingly, the recovery from low-voltage inactivation of Kv4.2 + DPP + 1b, could be well described with a single-exponential function for all recovery potentials. The time constants obtained at different recovery potentials were 483 ± 87.3 ms (-120 mV; n = 8) and 830 ± 183 ms (-90 mV; n = 9; Figure 4.9D), with a voltage dependence (q_{app}) of 0.52, corresponding to $\tau_{2,rec}$ obtained from the recovery from high-voltage inactivation at +40 mV (Table 4.5). For Kv4.2 + DPP (Figure 4.11A), we measured the recovery from low-voltage inactivation at -100 mV as comparison and the recovery time constant obtained by a single-exponential fit was 45.1 ± 14.3 ms (n = 5), which was significantly smaller compared to the τ_{rec} of Kv4.2 + DPP + 1b at -100 mV (644 ± 149 ms). Our results indicated that if 1b was co-expressed and inactivation was induced at a low voltage, preventing the channel from opening and allowing the channel recovery from inactivation, only the slow recovery component was detected in this situation. Thus, 1b still slowed recovery from low-voltage inactivation.

Table 4.5 Kinetics of recovery from high- and low-voltage inactivation at different recovery potentials.

Recovery potential (mV)	recovery from high-voltage inactivation (+40 mV)				recovery from low-voltage inactivation (-70 mV)
	$\tau_{1,rec}$ (ms)	$amp_{1,rec}$ (%)	$\tau_{2,rec}$ (ms)	$amp_{2,rec}$ (%)	τ_{rec} (ms)
-120	13.7 ± 2.1 (10)	50.0 ± 9.8 (10)	423 ± 64.2 (10)	50.0 ± 9.8 (10)	483 ± 87.3 (8)
-110	16.4 ± 3.1 (12)	50.3 ± 9.2 (12)	467 ± 83.0 (12)	49.7 ± 9.2 (12)	492 ± 102 (10)
-100	21.6 ± 4.6 (10)	52.2 ± 10.7 (10)	577 ± 141.3 (10)	47.8 ± 10.7 (10)	644 ± 149 (10)
-90	29.3 ± 5.6 (11)	50.0 ± 9.6 (11)	775 ± 213.3 (11)	50.0 ± 9.6 (11)	830 ± 183 (9)
-80	36.5 ± 8.2 (5)	53.2 ± 6.0 (5)	900 ± 98.1 (5)	46.8 ± 6.0 (5)	-

Mean ± SD and numbers of observations (n) are given for recovery from inactivation ($\tau_{x,rec}$ and $amp_{x,rec}$) at different recovery potentials.

4.3.1.2 Recovery from inactivation with different inactivating voltages

Based on the results in Chapter 4.3.1.1, we found that in the Kv4.2 + DPP + 1b ternary configuration, if inactivation was induced at -70 mV and the channels went directly into an inactivated state without opening, recovery from inactivation was described by a single-exponential function with only a slow recovery component. Therefore, we wanted to find out how the recovery kinetics would change if inactivation were induced at stronger depolarized voltages and the channels were partially opened.

We applied a special double-pulse protocol to study the recovery from inactivation with different inactivating voltages (see Materials and methods; Figure 3.6). Recovery from inactivation, in which the inactivation was induced at -35 and +70 mV from the same oocyte, was measured after variable interpulse durations at -100 mV. The comparison of the test currents showed that recovery from inactivation was faster when the inactivation was induced at +70 mV compared to -35 mV (Figure 4.10A). Normalized data ($I_{test}/I_{control}$) with different inactivating voltages were plotted against the interpulse duration on a log-scale (Figure 4.10C). The data points with inactivation at -70 mV were identical to those shown in Figure 4.9D. Except for inactivation at -70 mV, when the channels were depolarized stronger and partially opened (inactivation at -35, 0, +35 and +70 mV), the fast recovery component became manifest and the recovery from inactivation of Kv4.2 + DPP + 1b had to be fitted with a double-exponential function. The respective time constants and their relative amplitudes obtained with different inactivating voltages were plotted below and summarized

in Table 4.6. Notably, the relative amplitudes of fast recovery time constants increased from 0 to 30 % with increasingly stronger depolarization of the inactivating voltages (from -70 mV to +70 mV; Figure 4.10C and 4.10E). However, the $\tau_{1,rec}$ and $\tau_{2,rec}$ were not different if inactivation was induced at different voltages. As comparison, for Kv4.2 + DPP, recovery from inactivation with different inactivating voltages was measured and the kinetics were well fitted with a single-exponential function (Figure 4.11A). The time constants obtained are summarized in Table 4.6, and they showed no significant difference if stronger depolarized inactivating voltages were applied ($p>0.05$). Moreover, they did not differ from the τ_{rec} of Kv4.2 + DPP obtained with the standard recovery protocols at -100 mV (τ_{rec} was 38.6 ± 9.1ms; n = 5). The data suggest that, if 1b was co-expressed, the Kv4.2 channel complexes not only accumulate in the known closed-inactivated state, from which they could directly recover, but may also enter another inactivated state in order to exert the extremely slow recovery component.

4.3.1.3 Recovery from inactivation with different inactivating pulse durations

As the kinetics of recovery from inactivation of Kv4.2 + DPP + 1b were modulated with different inactivating voltages, another special double-pulse protocol was performed to investigate recovery from inactivation with different inactivating durations (see Materials and methods; Figure 3.7). The test currents acquired after a shorter inactivating pulse duration (80 ms) were larger compared to a longer inactivating pulse duration (10 s; Figure 4.10B). Recovery kinetics were described by a double-exponential, if inactivation was induced at +40 mV for 40, 80, 400 and 3000 ms (Figure 4.10D). The data points with inactivation at +40 mV for 3 s were identical to those shown in Figure 4.3D. Intriguingly, if the inactivation was induced at +40 mV for 5, 10 or 20 s, a triple-exponential function was needed to fit the recovery kinetics, with $\tau_{1,rec}$ for fast time constant, $\tau_{2,rec}$ for intermediate time constant, and $\tau_{3,rec}$ for an extremely slow time constant (Figure 4.10D and Figure 4.10F). Recovery time constants and their relative amplitudes were summarized in Table 4.7. Specifically, if the inactivation was induced at +40 mV for 80 ms, $\tau_{1,rec}$ was 20.5 ± 5.9 ms (81.1 ± 3.3 %; n = 8) and $\tau_{2,rec}$ was 1374 ± 410 ms (18.9 ± 3.3 %). If the inactivation was induced at +40 mV for 10 s, $\tau_{1,rec}$ was 32.1 ± 5.6 ms (22.1 ± 3.4 %; n = 17), $\tau_{2,rec}$ was 898 ± 123 ms (67.8 ± 4.0 %), and $\tau_{3,rec}$ was 12090 ± 2401 ms (10.1 ± 2.6 %). Detailed analysis revealed that the recovery kinetics remained biphasic with roughly unchanged recovery time constants, while the relative amplitude of the fast component decreased gradually, and the

slow component became more dominant with increasing inactivating pulse durations.

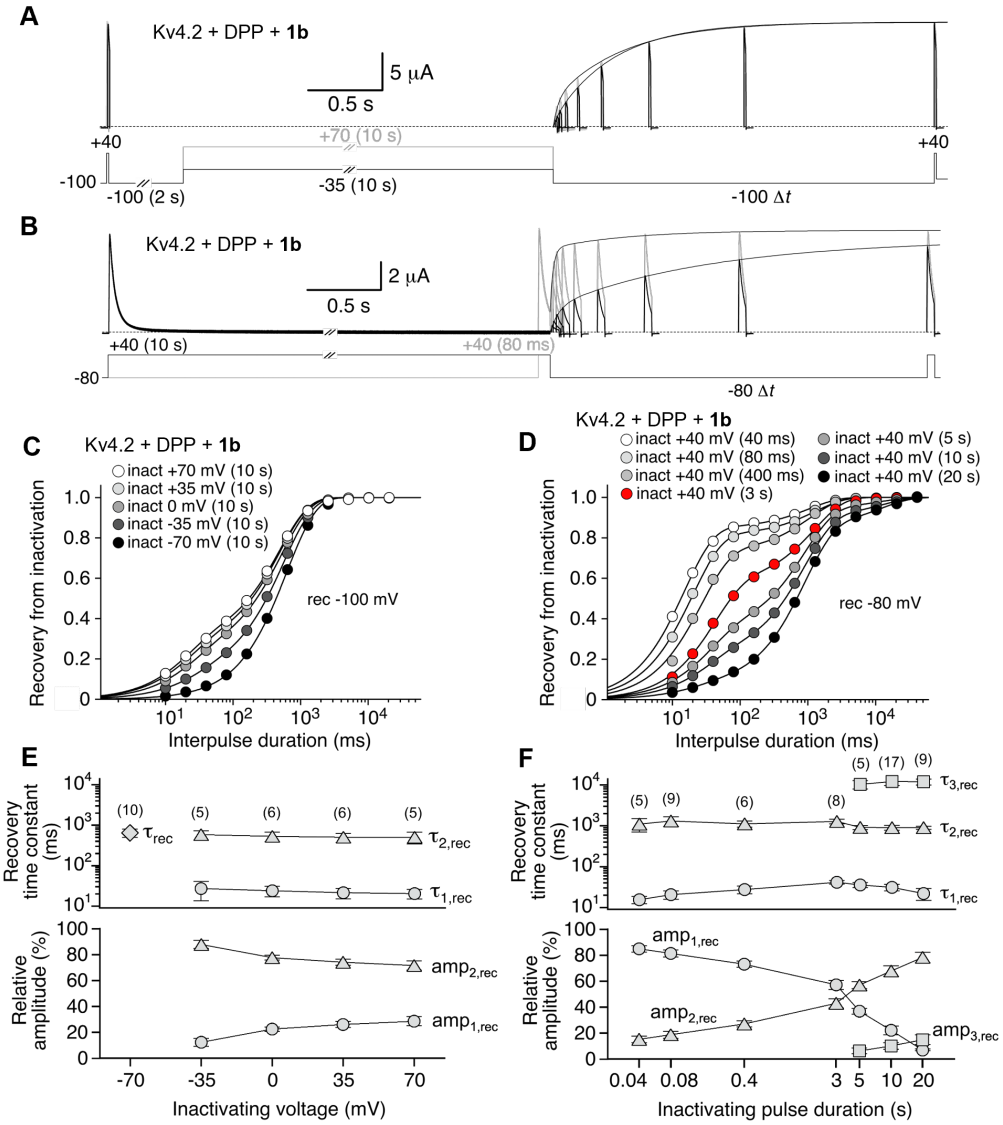

Figure 4.10 Kinetics of recovery from inactivation in ternary Kv4.2 + DPP + 1b configuration with different inactivating voltages and pulse durations. A: Inactivation was induced at different voltages from -70 to +70 mV for 10 s (recordings shown for -35 and +70 mV) and recovery from inactivation was measured after variable interpulse durations at -100 mV (recovery potential; Δt, see inset), with same oocyte; -35 mV in black and +70 mV in grey. Brief control and test currents were recorded at +40 mV. B: Inactivation was induced at +40mV for different durations from 40 ms to 20 s (recordings shown for 80 ms and 10 s) and recovery from inactivation was measured after variable interpulse durations at -80 mV (recovery potential; Δt, see inset), with same oocyte, 80 ms in black and 10 s in grey. C: Recovery kinetics were described by a single-exponential (inactivation induced at -70 mV, data from Figure 4.9) or a double-exponential function (inactivation at -35, 0, +35 and +70 mV); different recovery potential as indicated. D: Recovery kinetics were described by a double exponential (inactivation at +40 mV for 40, 80 and 400 ms, 3 s; 3 s data same as Figure 4.3) or a triple-exponential function (inactivation at +40 mV for 5, 10 and 20 s). E: Recovery time constants and relative amplitudes of each time constant (τ_{rec}: diamond; $\tau_{1,rec}$ and $amp_{1,rec}$: circles; $\tau_{2,rec}$ and $amp_{2,rec}$: triangles) are plotted below at different inactivating potentials (-70, -35, 0, +35 and +70 mV). F: Recovery time constants and relative amplitudes of each time constant ($\tau_{1,rec}$ and $amp_{1,rec}$: circles; $\tau_{2,rec}$ and $amp_{2,rec}$: triangles; $\tau_{3,rec}$ and $amp_{3,rec}$: squares) are plotted below at different inactivating pulse durations (40, 80, and 400 ms, 3, 5, 10 and 20 s); error bars are SD. numbers of oocytes indicated (n). Kv4.2 + DPP + 1b (1.7 + 5 + 10, ng per oocyte), measurement carried out on two days after cRNA injection (d2).

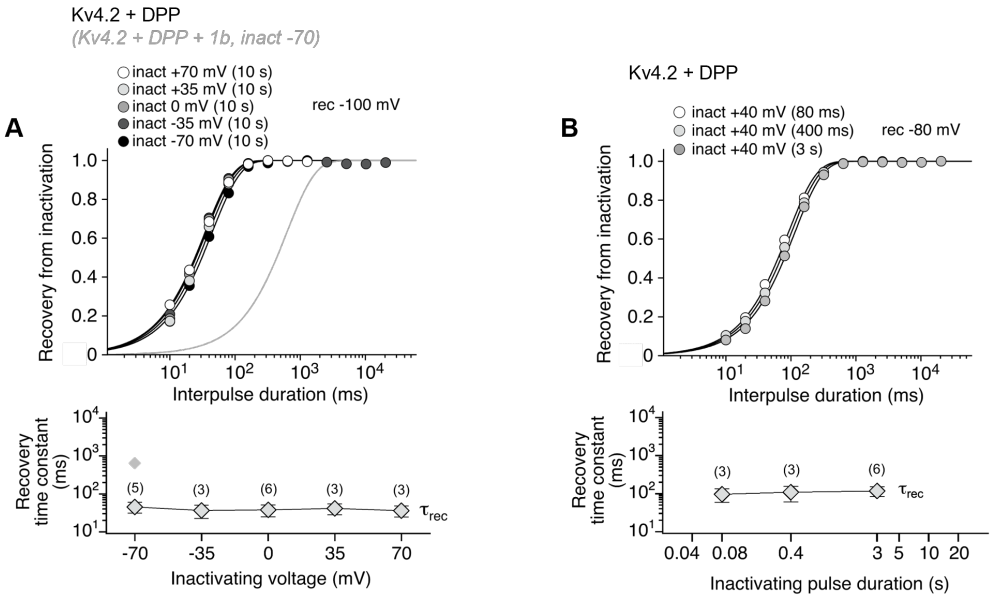

Figure 4.11 Kinetics of recovery from inactivation of Kv4.2 + DPP with different inactivating voltages and pulse durations in the absence of 1b. A: Inactivation was induced at different voltages from -70 to +70 mV for 10 s (recovery potential: -100 mV). Recovery kinetics were described by a single-exponential function. Recovery time constants (τ_{rec}: diamond) are plotted below at different inactivating voltages (-70, -35, 0, +35 and +70 mV); error bars are SD. B: Inactivation was induced at +40 mV for different pulse durations (40 ms, 80 ms and 3 s). Recovery kinetics were described by a single-exponential function and recovery time constants (τ_{rec}: diamond) are plotted below at different inactivating pulse durations; numbers of oocytes indicated (n). Kv4.2 + DPP (1.7 + 5 ng per oocyte), measurement carried out on two days after cRNA injection (d2).

Table 4.6 Kinetics of recovery from inactivation after different inactivating voltages.

Inactivating voltage (mV)	Kv4.2 + DPP + 1b				Kv4.2 + DPP
	$\tau_{1,rec}$ (ms)	$amp_{1,rec}$ (%)	$\tau_{2,rec}$ (ms)	$amp_{2,rec}$ (%)	τ_{rec} (ms)
-70			644 ± 149 (10)	100	45.1 ± 14.3 (5)
-35	27.0 ± 13.6 (5)	12.2 ± 3.1 (5)	579 ± 150 (5)	87.8 ± 3.1 (5)	36.4 ± 13.9 (3)
0	23.9 ± 7.0 (6)	22.4 ± 1.8 (6)	529 ± 146 (6)	77.6 ± 1.8 (6)	37.7 ± 13.0 (6)
+35	21.2 ± 6.1 (6)	26.0 ± 2.3 (6)	498 ± 128 (6)	74.0 ± 2.3 (6)	41.1 ± 13.0 (3)
+70	20.3 ± 5.4 (5)	28.5 ± 3.6 (5)	503 ± 161 (5)	71.5 ± 3.6 (5)	36.0 ± 11.7 (3)

Mean ± SD and numbers of observations (n) are given for recovery from inactivation ($\tau_{x,rec}$ and $amp_{x,rec}$) after different inactivating voltages. Recovery potentials is at -100 mV for all inactivating voltages.

Table 4.7 Kinetics of recovery from inactivation after different inactivating pulse durations.

Inactivating pulse duration (ms)	Kv4.2 + DPP + 1b						Kv4.2 + DPP
	$\tau_{1,rec}$ (ms)	$amp_{1,rec}$ (%)	$\tau_{2,rec}$ (ms)	$amp_{2,rec}$ (%)	$\tau_{3,rec}$ (ms)	$amp_{3,rec}$ (%)	τ_{rec} (ms)
40	15.5 ± 3.2 (5)	84.8 ± 2.5 (5)	1098 ± 392 (5)	15.2 ± 2.5 (5)	-		-
80	20.5 ± 5.9 (6)	81.1 ± 3.3 (6)	1374 ± 410 (6)	18.9 ± 3.3 (6)			95.3 ± 36.8 (3)
400	27.3 ± 5.8 (6)	73.0 ± 2.4 (6)	1110 ± 188 (6)	27.0 ± 2.4 (6)			108 ± 47.6 (3)
3000	41.4 ± 4.2 (8)	57.1 ± 3.5 (8)	1275 ± 167 (8)	42.9 ± 3.5 (8)			116.6 ± 32.4 (3)
5000	35.6 ± 5.0 (5)	36.8 ± 2.2 (5)	903 ± 96.8 (5)	56.9 ± 2.6 (5)	10262 ± 2362 (5)	6.3 ± 2.3 (5)	-
10000	32.1 ± 5.6 (17)	22.1 ± 3.4 (17)	898 ± 123 (17)	67.8 ± 4.0 (17)	12090 ± 2401 (17)	10.1 ± 2.6 (17)	
20000	21.9 ± 7.1 (9)	7.0 ± 0.7 (9)	893 ± 74.3 (9)	78.2 ± 4.0 (9)	11886 ± 1916 (9)	14.8 ± 3.7 (9)	

Mean ± SD and numbers of observations (n) are given for recovery from inactivation ($\tau_{x,rec}$ and $amp_{x,rec}$) after different inactivating pulse durations. Recovery potential is at -80 mV for all inactivating durations.

Moreover, with extraordinarily long inactivating pulse durations (> 3 s), a third recovery component became apparent. For comparison, recovery from inactivation with different inactivating pulse durations of Kv4.2 + DPP was recorded (80 ms, 400 ms and 3 s) and the kinetics were well fitted with a single-exponential function (Figure 4.11B). The time constants obtained were 95.3 ± 36.8 ms (80 ms; n = 3), 108 ± 47.6 ms (400 ms; n = 3) and 116.6 ± 32.4 ms (3 s; n = 6; same data from Figure 4.3D), which showed no statistic difference. Thus, upon co-expression with 1b, if the inactivating pulse duration was increased (from 40 ms to 20 s), recovery became increasingly slower, which was reflected in the extremely slow recovery time constants becoming even larger and accounting for more to the recovery kinetics. The increased inactivation pulse durations may force the channels to enter another inactivated state rather than just the closed-inactivated state.

4.3.2 Investigating the involvement of N-type inactivation in the KChIP1b-mediated biphasic recovery kinetics

As N-type inactivation is one classical inactivation mechanism of Kv channels if may be promoted by 1b co-expression in Kv4 channels. Therefore, we used the N-terminal deletion mutant Kv4.2 Δ10, in which the 10 amino acids of N-terminal of Kv4.2 α-subunit were deleted, to abolish N-type inactivation. Kv4.2 Δ10 was co-expressed with DPP and 1b to

form the ternary configuration (Kv4.2 Δ10 + DPP + 1b) to investigate the involvement of N-type inactivation in the 1b-mediated biphasic recovery kinetics. Figure 4.12A shows normalized currents mediated by Kv4.2 + DPP + 1b and Kv4.2 Δ10 + DPP + 1b upon depolarization at + 40 mV. Macroscopic inactivation of the two channel complexes was fitted with a triple-exponential function. For Kv4.2 Δ10 + DPP + 1b, $\tau_{1,inact}$ was 32.2 ± 7.1 ms (47.1 ± 14.5 %; n = 8), $\tau_{2,inact}$ was 78.9 ± 14.3 ms (48.6 ± 12.8 %), and $\tau_{3,inact}$ was 283.6 ± 74.4 ms (4.4 ± 1.8 %). The data for Kv4.2 + DPP + 1b here are identical to those shown in Figure 4.2D (d2; Table 4.1). Only $\tau_{3,inact}$ of Kv4.2 Δ10 + DPP + 1b was significantly smaller compared to $\tau_{3,inact}$ of Kv4.2 + DPP + 1b (513 ± 40 ms; 4.0 ± 1.3 %; n = 17). Other inactivation parameters of Kv4.2 Δ10 + DPP + 1b were not significantly different from Kv4.2 + DPP + 1b, indicating that the regulatory effect of 1b on the Kv4.2 Δ10 macroscopic inactivation was weaker compared to the wild-type Kv4.2 channel. Comparison of recovery kinetics between Kv4.2 + DPP + 1b and Kv4.2 Δ10 + DPP + 1b is shown in Figure 4.12B.

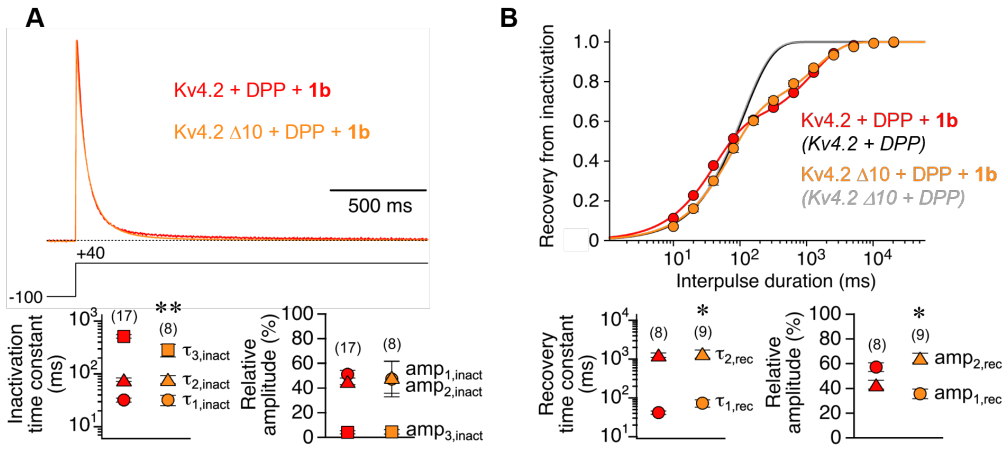

Figure 4.12 Macroscopic inactivation and recovery from inactivation of an N-terminal deletion mutant (Kv4.2 Δ10) co-expressed with DPP and 1b. A: Normalized currents mediated by Kv4.2 + DPP + 1b (red, same data as Figure 4.2D on d2) and Kv4.2 Δ10 + DPP + 1b (orange) channels; dotted line represents zero current. Inactivation time constants and their relative amplitudes, obtained by fitting the current decay kinetics with a triple-exponential function are plotted below ($\tau_{1,inact}$ and $amp_{1,inact}$: circle, $\tau_{2,inact}$ and $amp_{2,inact}$: triangles, $\tau_{3,inact}$ and $amp_{3,inact}$: squares; mean ± SD); numbers of oocytes (n) indicated. B: Kinetics of recovery from inactivation of Kv4.2 + DPP + 1b (red, same data as shown in Figure 4.3D) and Kv4.2 Δ10 + DPP + 1b (orange) channels were fitted with a double-exponential function. Recovery time constants and their relative amplitudes ($\tau_{1,rec}$ and $amp_{1,rec}$: circles, $\tau_{2,rec}$ and $amp_{2,rec}$: triangles; mean ± SD) are plotted below. Grey curve: Kv4.2 Δ10 + DPP; black curve: Kv4.2 + DPP (same data as shown in Figure 4.3D); single-exponential fit, as control; numbers of oocytes indicated (n); measurement carried out on d2. Mutant effects were compared using an unpaired Student's *t*-test; significance of mutant effects is indicated as $^{*}(p<0.05)$ or $^{**}(p<0.0001)$.

The data here for Kv4.2 + DPP and Kv4.2 + DPP + 1b were the same as in Figure 4.3D. Recovery from inactivation of Kv4.2 Δ10 + DPP was measured for control and fitted with a

single-exponential function with a τ_{rec} of 112 ± 27.9 ms (n = 7), which was not different from Kv4.2 + DPP (Figure 4.12B). For Kv4.2 Δ10 + DPP + 1b, the recovery from inactivation was still described with a double-exponential function. The $\tau_{1,rec}$ and its relative amplitude were slightly increased (72.9 ± 15.6 ms; 64.5 ± 3.9 %; n = 9), compared to $\tau_{1,rec}$ and $amp_{1,rec}$ of Kv4.2 + DPP + 1b, but the $\tau_{2,rec}$ induced by 1b was not affected by N-terminal deletion (Table 4.8), indicating that N-type inactivation is not involved in 1b-mediated biphasic recovery kinetics.

4.3.3 Investigating the involvement of P/C-type inactivation in the KChIP1b-mediated biphasic recovery kinetics

P/C-type inactivation is another classical inactivation mechanism of Kv channels. In order to investigate whether P/C-type inactivation is involved in 1b-mediated biphasic recovery kinetics, macroscopic inactivation and recovery from inactivation of Kv4.2 + DPP + 1b and Kv4.2 Δ10 + DPP + 1b were first recorded in a normal K^+ concentration (2 mM) as control, and then switched to elevated external K^+ (98 mM) with the same oocyte to inhibit P/C-type inactivation by preventing the conformational changes of pore domain. Figure 4.13A shows normalized currents mediated by Kv4.2 + DPP + 1b, which were recorded in 2 mM and 98 mM external K^+, respectively. Macroscopic inactivation was well fitted with a double-exponential function. The fast inactivation time constant ($\tau_{f,inact}$) of Kv4.2 + DPP + 1b was significantly reduced by elevated external K^+, decreasing from 34.9 ± 6.4 ms in 2 mM K^+ to 19.8 ± 0.8 ms in 98 mM K^+ (n = 5; Figure 4.13A). The slow inactivation time constant ($\tau_{s,inact}$) and its relative amplitude were not affected by elevated external K^+ (Table 4.8). Intriguingly, as shown in Figure 4.13B, the slow recovery time constant ($\tau_{2,rec}$) of Kv4.2 + DPP + 1b was significantly reduced by elevated external K^+, from 1377 ± 189 ms in 2 mM K^+ to 568 ± 129 ms in 98 mM K^+ (n = 6). The fast recovery time constant ($\tau_{1,rec}$) and relative amplitudes of each time constant were not affected (Table 4.8). The acceleration of slow recovery component and inactivation in elevated external K^+, indicated that upon 1b co-expression the Kv4.2 channel tends to experience P/C-type inactivation.

Elevated external K^+ also influenced Kv4.2 Δ10 + DPP + 1b channels in the same manner as wild-type channels. Figure 4.13C shows the normalized currents mediated by Kv4.2 Δ10 + DPP + 1b, which was recorded in 2 mM and 98 mM external K^+ from the same oocyte. Macroscopic inactivation was well fitted with a double-exponential function. Upon switching to elevated external K^+, both $\tau_{f,inact}$ and $\tau_{s,inact}$ of Kv4.2 Δ10 + DPP + 1b became

significantly smaller, and the relative amplitudes of $\tau_{f,inact}$ were also increased (Table 4.8).

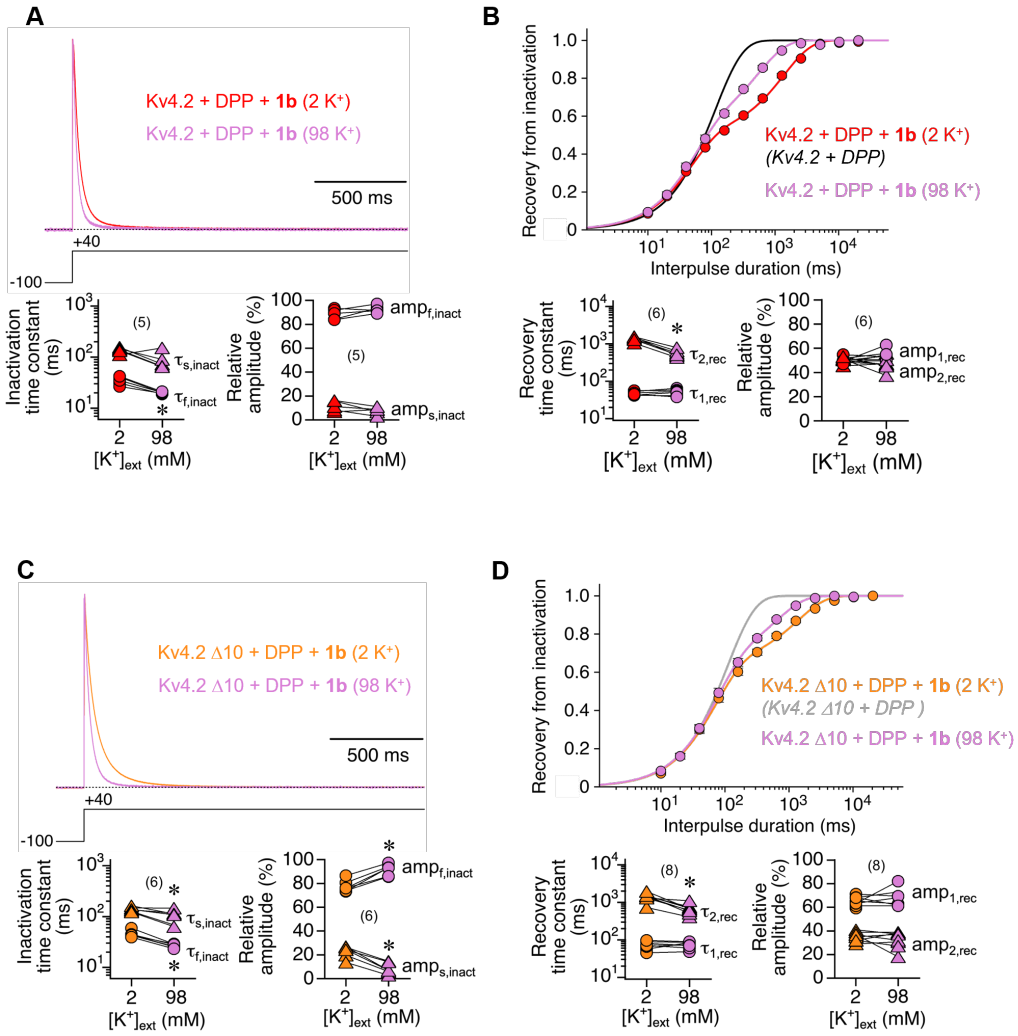

Figure 4.13 Macroscopic inactivation and recovery from inactivation of wild-type and mutant ternary Kv4.2 + DPP + 1b channels in normal and elevated external K^+. A: Normalized currents of Kv4.2 + DPP + 1b channels in 2 mM KCl (red) and 98 mM KCl (purple); dotted line represents zero current. Inactivation time constants and their relative amplitudes, obtained by fitting the current decay kinetics with a double-exponential function are plotted below ($\tau_{f,inact}$ and $amp_{f,inact}$: circle, $\tau_{s,inact}$ and $amp_{s,inact}$: triangles; data pairs indicated; mean ± SD); numbers of oocytes (n) indicated. B: Kinetics of recovery from inactivation of Kv4.2 + DPP + 1b channels in 2 mM KCl (red) and 98 mM KCl (purple) were analyzed using a double-exponential function; recovery time constants and relative amplitudes ($\tau_{1,rec}$ and $amp_{1,rec}$: circles, $\tau_{2,rec}$ and $amp_{2,rec}$: triangles; data pairs indicated) are plotted below. Black curve: Kv4.2 + DPP in 2 mM KCl, single-exponential function, as control; C and D: Same measurements and analysis for Kv4.2 Δ10 + DPP + 1b in 2 mM KCl (orange) and 98 mM KCl (purple); Grey curve: Kv4.2 Δ10 + DPP in 2 mM KCl, single-exponential function, as control. All time constants and relative amplitudes are presented as means ± SD; number of oocytes (n) indicated; measurement carried out on d2. In the recovery plots the data are presented as means ± SEM. Individual pairs are shown and were compared using a paired Student's *t*-test; significance of effects of switching to elevated external K^+ are indicated as * ($p<0.05$) or ** ($p<0.0001$).

As shown in Figure 4.13D, elevated external K^+ accelerated the slow recovery component of Kv4.2 Δ10 + DPP + 1b, with $\tau_{2,rec}$ decreasing from 1396 ± 339 ms in 2 mM K^+ to 670 ± 209 ms in 98 mM K^+ (n = 6). The $\tau_{1,rec}$ and relative amplitudes of each time constant remained unchanged (Table 4.8). The acceleration of slow recovery component and inactivation of Kv4.2 Δ10 + DPP + 1b in elevated external K^+, indicated that although N-type inactivation was abolished, Kv4.2 channel still tends to experience P/C-type inactivation upon 1b co-expression.

The process of P/C-type inactivation can also be slowed by application of extracellular TEA (López-Barneo et al., 1993). In order to further investigate the involvement of P/C-type inactivation, macroscopic inactivation and recovery from inactivation of Kv4.2 + DPP + 1b and Kv4.2 Δ10 + DPP + 1b were first recorded in control solution and then switched to elevated external TEA (98 mM) from the same oocyte, in order to inhibit P/C-type inactivation. Figure 4.14A shows normalized currents mediated by Kv4.2 + DPP + 1b, which were recorded in 2 mM and 98 mM TEA, respectively, from the same oocyte. Macroscopic inactivation was well fitted with a double-exponential function. Elevated external TEA had no significant effect on the inactivation kinetics of wild-type ternary. As shown in Figure 4.14B, the fast recovery component was accelerated by elevated external TEA, with a $\tau_{1,rec}$ of 38.3 ± 3.6 ms and a decreased relative amplitude of 43.0 ± 2.3 % (n = 5), while $\tau_{2,rec}$ remained unchanged. Differently, the $\tau_{f,inact}$ and $\tau_{s,inact}$ of Kv4.2 Δ10 + DPP + 1b were both significantly reduced by elevated external TEA, and the relative amplitude of fast time constant was increased (Figure 4.14C; Table 4.8). Figure 4.14D shows that $\tau_{2,rec}$ of Kv4.2 Δ10 + DPP + 1b in elevated external TEA (1303 ± 275 ms; 37.3 ± 2.5 %; n = 6) was smaller compared to $\tau_{2,rec}$ (1493 ± 248 ms; 36.3 ± 2.6 %) in control solution, whereas the $\tau_{1,rec}$ in different solutions remained unchanged (Table 4.8). Thus, superfusion with TEA solution had no obvious effects, except for an acceleration of current decay kinetics, which was more pronounced for Kv4.2 Δ10 + DPP + 1b than for wild-type channels.

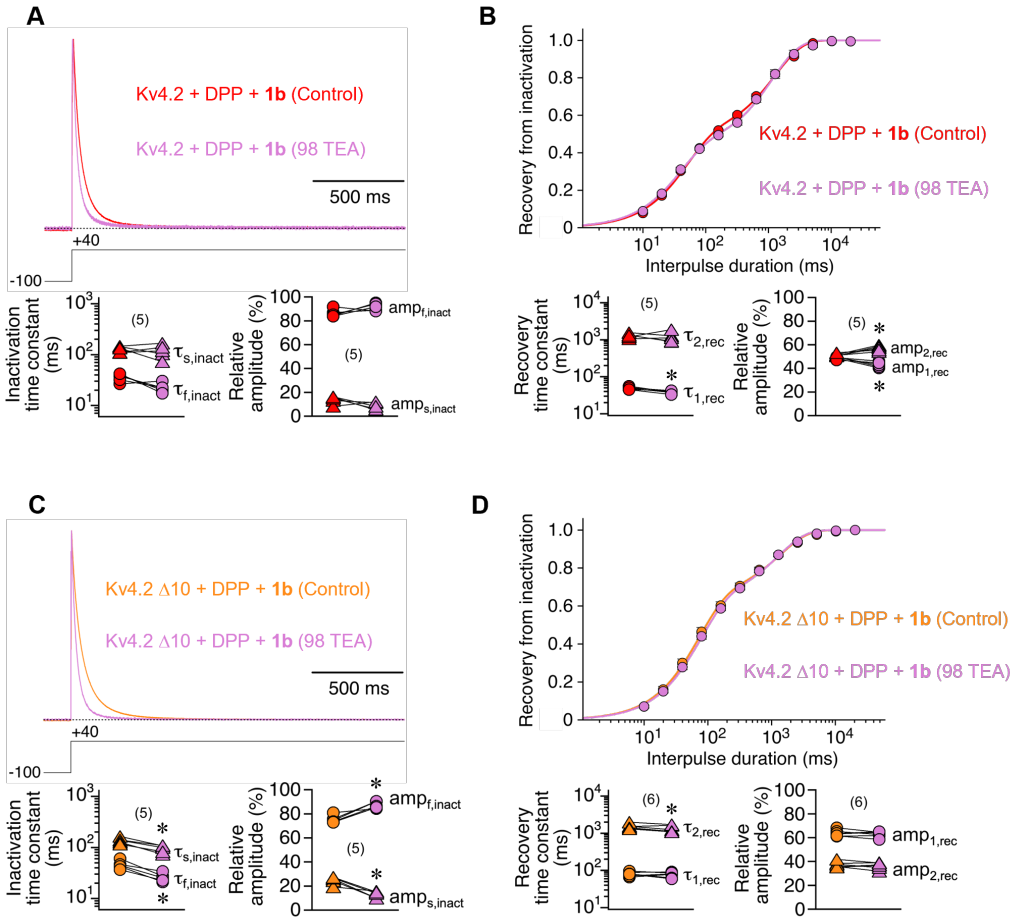

Figure 4.14 Macroscopic inactivation and recovery from inactivation of wild-type and mutant ternary Kv4.2 + DPP + 1b channels in normal and elevated external TEA. A: Normalized currents of Kv4.2 + DPP + 1b channels in control (red) and TEA solution (purple); dotted line represents zero current. Inactivation time constants and their relative amplitudes, obtained by fitting the current decay kinetics with a double-exponential function are plotted below ($\tau_{f,inact}$ and $amp_{f,inact}$: circle, $\tau_{s,inact}$ and $amp_{s,inact}$: triangles; data pairs indicated; mean ± SD); numbers of oocytes (n) indicated. B: Kinetics of recovery from inactivation of Kv4.2 + DPP + 1b channels in control and TEA solution were analyzed using a double-exponential function; recovery time constants and relative amplitudes ($\tau_{1,rec}$ and $amp_{1,rec}$: circles, $\tau_{2,rec}$ and $amp_{2,rec}$: triangles; data pairs indicated) are plotted below. C and D: Same measurements and analysis for Kv4.2 Δ10 + DPP + 1b in control (orange) and TEA solution (purple). All time constants and relative amplitudes are presented as means ± SD; number of oocytes (n) indicated; measurement carried out on d2. In the recovery plots the data are presented as means ± SEM. Individual pairs are shown and were compared using a paired Student's *t*-test; significance of effects of switching to elevated external TEA are indicated as * ($p<0.05$) or ** ($p<0.0001$).

4.3.4 Relationship between closed-state inactivation and KChIP1b-associated P/C-type inactivation features

In a previous study (Barghaan and Bähring, 2009), alanine-scanning mutagenesis was performed in the S4-S5 linker and the distal part of S6 of the Kv4.2 α-subunit, to investigate the dynamic coupling between the voltage sensors and the cytoplasmic gate that underlies

inactivation in Kv4.2 channels. Electrophysiological recordings indicated that the mutations in this domain influenced the likelihood of the channel entering the closed-inactivated state. Here, two S6 mutants were selected and co-expressed with DPP and 1b to study the effects of 1b on inactivation and recovery from inactivation under the condition of modified Kv4.2 channel CSI. The recovery time constant (τ_{rec}) of wild-type Kv4.2 in that study was 237 ms (Barghaan and Bähring, 2009; recovery potential at -100 mV). One mutant is Kv4.2 L400A, which exhibited the slowest recovery kinetics, with a τ_{rec} of 1924 ms, compared to wild-type Kv4.2 channel, indicative of a stable CSI. Another mutant is Kv4.2 N408A, which exhibited the fastest recovery kinetics, with a τ_{rec} of 69 ms, indicative of a very unstable CSI. Kinetics of macroscopic inactivation and recovery from inactivation of ternary configuration were measured in different solutions in order to study the relationship between CSI and KChIP1b-associated P/C-type inactivation features.

To investigate the mutant effects, normalized currents mediated by Kv4.2 + DPP + 1b (same as in Figure 4.2D on d2, as control), Kv4.2 L400A + DPP + 1b (Kv4.2 L400A ternary complex) and Kv4.2 N408A + DPP + 1b (Kv4.2 N408A ternary complex) are shown in Figure 4.15A. Macroscopic inactivation was here described with a triple-exponential function. The overall Kv4.2 L400A mutant effects was to slow the current decay. For Kv4.2 L400A ternary complex, $\tau_{3,inact}$ was 714 ± 125 ms (8.7 ± 3.0 %; n = 14), which was significantly larger compared to $\tau_{3,inact}$ of the wild-type ternary complex (Figure 4.15A; Table 4.8). The fast inactivation component accounted for 69.8 ± 11.5 % of the total decay, significantly larger compared to wild-type ternary complex. For Kv4.2 N408A ternary complex, $\tau_{1,inact}$ was significantly smaller (8.3 ± 1.8 ms), and its relative amplitude was larger (91.6 ± 2.2 %; n = 9), compared to the wild-type ternary complex, indicating that mutant effect of Kv4.2 N408A was to accelerate the current decay (Figure 4.15A; Table 4.8). In the absence of 1b, the recovery from inactivation of Kv4.2 N408A + DPP (21.3 ± 0.6 ms; n = 5) remained faster than Kv4.2 + DPP. Surprisingly, for Kv4.2 N408A ternary complex, 1b induced slower recovery kinetics, described by a single-exponential function (τ_{rec} was 690 ± 57.2 ms; n = 9) compared to τ_{rec} of Kv4.2 N408A + DPP (Figure 4.15B). For Kv4.2 L400A ternary complex, the kinetics of recovery from inactivation (Figure 4.15B) were not different from wild-type ternary complex (same as in Figure 4.3D).

To further investigate the involvement of P/C-type inactivation in two mutants upon 1b co-expression, normalized currents mediated by Kv4.2 L400A ternary complex recorded in 2 mM and 98 mM external K^+ from the same oocyte are shown in Figure 4.15C. The

macroscopic inactivation remained best described by a double-exponential function under this condition. The fast and slow inactivation constants of Kv4.2 L400A ternary complex were both significantly reduced by elevated external K^+, from 39.8 ± 263 ms (89 ± 3 %) in 2 mM K^+ to 24.7 ± 2.4 ms (91 ± 2 %) in 98 mM K^+ for $\tau_{f,inact}$, and from 532 ± 145 ms (11 ± 3 %) in 2 mM K^+ to 350 ± 88 ms (9 ± 2 %) in 98 mM K^+ for $\tau_{s,inact}$ (n = 5), accompanied by an increased relative amplitude of $\tau_{f,inact}$ (Table 4.8). $\tau_{2,rec}$ of Kv4.2 L400A ternary complex was significantly reduced by elevated external K^+, from 1254 ± 266 ms in 2 mM K^+ to 883 ± 263 ms in 98 mM K^+ (n = 9; $p < 0.05$), with a decrease of its relative amplitude (from 41.8 ± 4.4 % to 28.9 ± 7.1 %), whereas $\tau_{1,rec}$ remained unchanged (Table 4.8; Figure 4.15D). The acceleration of the slow recovery component and inactivation of Kv4.2 L400A ternary complex in elevated external K^+, indicates that 1b co-expression resulted in a similar modulation of inactivation and recovery kinetics in Kv4.2 L400A and wild-type Kv4.2 ternary.

Figure 4.15E shows the normalized currents mediated by Kv4.2 N408A + DPP + 1b, recorded in 2 mM and 98 mM external K^+ from the same oocyte. The fast inactivation time constant of Kv4.2 N408A + DPP + 1b was significantly reduced by elevated external K^+, and its relative amplitudes were decreased (Table 4.8). Interestingly, the recovery kinetics of Kv4.2 N408 A + DPP + 1b were well described with a single-exponential function under both conditions (Figure 4.15F), with a significantly faster recovery in 98 mM K^+ (310 ± 27.5 ms; n = 5) compared to in 2 mM K^+ (666 ± 63.5 ms). Taken together, these results indicate that 1b co-expression attenuates the CSI of Kv4.2 N408A ternary complex and therefore the channel complex now potentially enters another inactivated-state that slows the recovery process. The slow recovery process can be accelerated by inhibiting P/C-type inactivation. Thus, the attenuation of closed-state inactivation emphasizes that 1b enhances P/C-type inactivation.

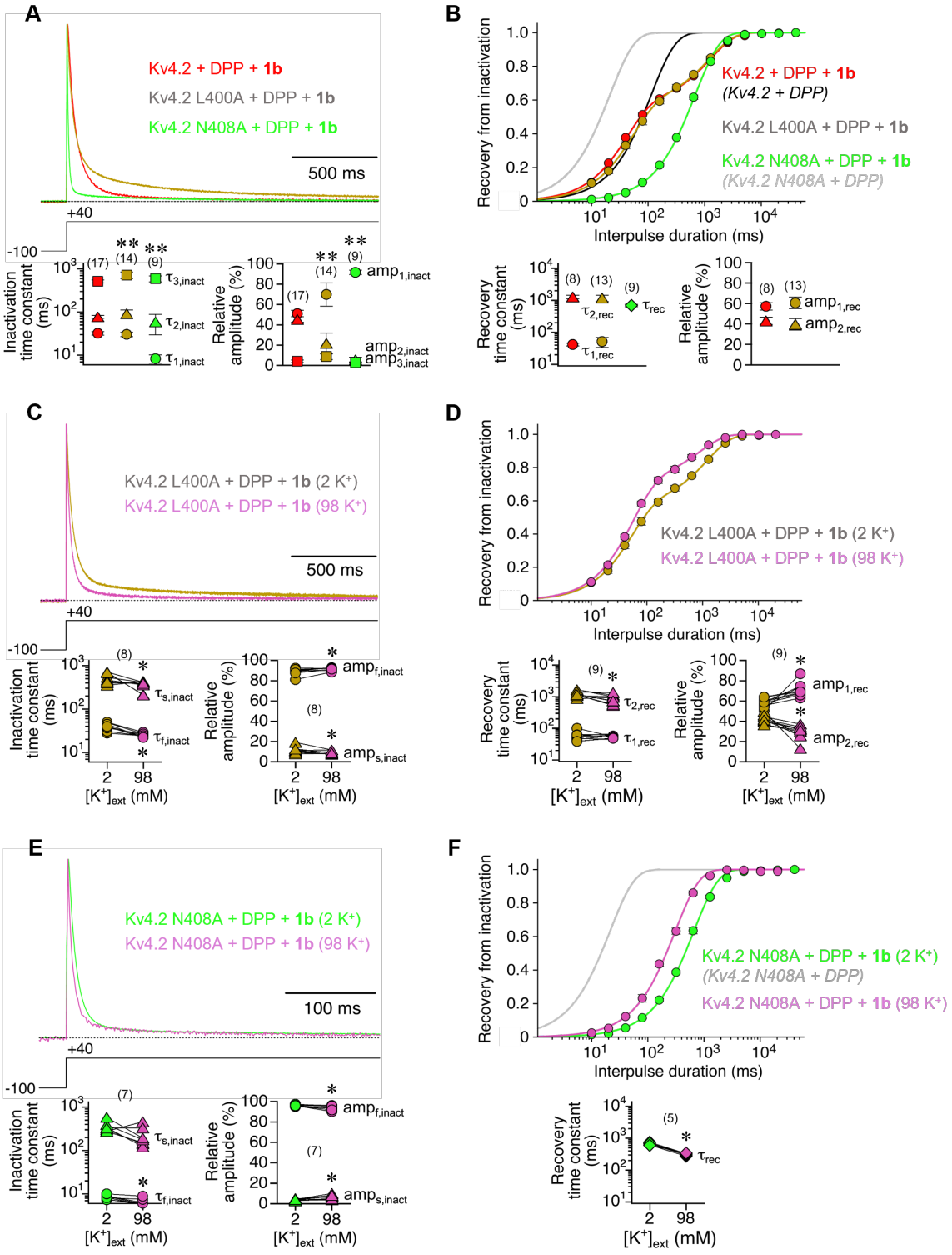
A
Kv4.2 + DPP + 1b
Kv4.2 L400A + DPP + 1b
Kv4.2 N408A + DPP + 1b
500 ms
+40
-100
Inactivation time constant (ms)
τ3,inact
τ2,inact
τ1,inact
Relative amplitude (%)
amp1,inact
amp2,inact
amp3,inact
B
Recovery from inactivation
Interpulse duration (ms)
Kv4.2 + DPP + 1b
(Kv4.2 + DPP)
Kv4.2 L400A + DPP + 1b
Kv4.2 N408A + DPP + 1b
(Kv4.2 N408A + DPP)
Recovery time constant (ms)
τ2,rec
τ1,rec
τrec
Relative amplitude (%)
amp1,rec
amp2,rec
C
Kv4.2 L400A + DPP + 1b (2 K+)
Kv4.2 L400A + DPP + 1b (98 K+)
500 ms
+40
-100
Inactivation time constant (ms)
τs,inact
τf,inact
[K+]ext (mM)
Relative amplitude (%)
ampf,inact
amps,inact
D
Recovery from inactivation
Interpulse duration (ms)
Kv4.2 L400A + DPP + 1b (2 K+)
Kv4.2 L400A + DPP + 1b (98 K+)
Recovery time constant (ms)
τ2,rec
τ1,rec
[K+]ext (mM)
Relative amplitude (%)
amp1,rec
amp2,rec
E
Kv4.2 N408A + DPP + 1b (2 K+)
Kv4.2 N408A + DPP + 1b (98 K+)
100 ms
+40
-100
Inactivation time constant (ms)
τs,inact
τf,inact
[K+]ext (mM)
Relative amplitude (%)
ampf,inact
amps,inact
F
Recovery from inactivation
Interpulse duration (ms)
Kv4.2 N408A + DPP + 1b (2 K+)
(Kv4.2 N408A + DPP)
Kv4.2 N408A + DPP + 1b (98 K+)
Recovery time constant (ms)
τrec
[K+]ext (mM)

Figure 4.15 Macroscopic inactivation and recovery from inactivation of Kv4.2 S6 mutants co-expressed with DPP and 1b in normal and elevated external K^+. From a previous alanine mutagenesis scan (Barghaan and Bähring, 2009) in the distal S6 segment Kv4.2 L400A and N408A (slowest and fastest recovery kinetics obtained in that study, respectively) were picked and co-expressed with DPP and 1b. A: Normalized currents of Kv4.2 + DPP + 1b (red), Kv4.2 L400A + DPP + 1b (olive) and Kv4.2 N408A + DPP + 1b (green) channels. Current decay kinetics were fitted with a triple-exponential function; inactivation time constants and relative amplitudes of the total decay ($\tau_{1,inact}$ and $amp_{1,inact}$: circles; $\tau_{2,inact}$ and $amp_{2,inact}$: triangles; $\tau_{3,inact}$ and $amp_{3,inact}$: squares) are plotted below. B: Kinetics of recovery from inactivation were fitted with a single-exponential function (Kv4.2 N408A + DPP + 1b) or a double-exponential function (Kv4.2 + DPP + 1b and Kv4.2 L400A + DPP + 1b). Recovery time constants and their relative amplitudes ($\tau_{1,rec}$ and $amp_{1,rec}$: circles; $\tau_{2,rec}$ and $amp_{2,rec}$: triangles; τ_{rec}: diamond) are plotted below. C: Normalized currents of Kv4.2 L400A + DPP + 1b channels in 2 mM KCl (olive) and 98 mM KCl (purple). Time constants of macroscopic inactivation and their relative amplitudes obtained with double-exponential fitting are shown ($\tau_{f,inact}$ and $amp_{f,inact}$: circle, $\tau_{s,inact}$ and $amp_{s,inact}$: triangles; data pairs indicated; mean ± SD). D: Kinetics of recovery from inactivation of Kv4.2 L400A + DPP + 1b channels in 2 mM KCl (olive) and 98 mM KCl (purple) were analyzed using a double-exponential fit; recovery time constants and their relative amplitudes ($\tau_{1,rec}$ and $amp_{1,rec}$: circles; $\tau_{2,rec}$ and $amp_{2,rec}$) are plotted below. E: Normalized currents of Kv4.2 N408A + DPP + 1b channels in 2 mM KCl (green) and 98 mM KCl (purple). Time constants of macroscopic inactivation and their relative amplitudes obtained with double-exponential fitting are shown ($\tau_{f,inact}$ and $amp_{f,inact}$: circle, $\tau_{s,inact}$ and $amp_{s,inact}$: triangles; data pairs indicated; mean ± SD). F: Kinetics of recovery from inactivation of Kv4.2 N408A + DPP + 1b channels in 2 mM KCl (green) and 98 mM KCl (purple) were analyzed using a single-exponential fit; recovery time constants (τ_{rec}: diamond log-scale) are plotted below.
(A-F): grey traces: Kv4.2 N408A + DPP; black traces: Kv4.2 + DPP; single-exponential fit, in 2 mM external KCl, as control; dotted line represents zero current; numbers of oocytes indicated (n); Kv4.2 (mutants) + DPP + 1b (1.7 + 5 + 10 ng per oocyte), measurement carried out on d2. Mutant effects were compared using unpaired Student's *t*-test; individual pairs are shown and were compared using a paired Student's *t*-test; significance of mutant effects and effects of switching to elevated external K^+ are indicated as * ($p<0.05$) or ** ($p<0.0001$).

Table 4.8 Experimental manipulation of Kv4.2 + DPP +1b channel inactivation.

Kv4.2 + DPP + 1b	I (+40) (µA)	$\tau_{1,inact}$ / $\tau_{f,inact}$ (ms)	$amp_{1,inact}$ / $amp_{f,inact}$ (%)	$\tau_{2,inact}$ / $\tau_{s,inact}$ (ms)	$amp_{2,inact}$ / $amp_{s,inact}$ (%)	$\tau_{3,inact}$ (ms)	$amp_{3,inact}$ (%)	$\tau_{1,rec}$ / τ_{rec} (ms)	$amp_{1,rec}$ (%)	$\tau_{2,rec}$ (ms)	$amp_{2,rec}$ (%)
Wildtype	**4.8 ± 0.9 (17)**	**32.0 ± 3.0 (17)**	**51 ± 3 (17)**	**77.4 ± 6.4 (17)**	**45 ± 3 (17)**	**513 ± 40 (17)**	**4 ± 1 (17)**	**41.4 ± 4.2 (8)**	**57 ± 4 (8)**	**1275 ± 167 (8)**	**43 ± 4 (8)**
Δ10	**22.4 ± 7.3 (9)**	**32.2 ± 7.1 (8)**	**47 ± 14.5 (8)**	**78.9 ± 14.3 (8)**	**49 ± 12.8 (8)**	**284 ± 74**** **(8)**	**4 ± 2 (8)**	**72.9 ± 15.6*** **(9)**	**65 ± 4*** **(9)**	**1382 ± 320 (9)**	**35 ± 4*** **(9)**
L400A	**3.2 ± 0.8 (11)**	**30.4 ± 3.5 (14)**	**70 ± 12**** **(14)**	**90.8 ± 20.2 (14)**	**22 ± 10 (14)**	**715 ± 125**** **(14)**	**8 ± 3 (14)**	**51.4 ± 17.6 (13)**	**61 ± 6 (13)**	**1177 ± 265 (13)**	**39 ± 6 (13)**
N408A	**6.9 ± 0.8 (11)**	**8.3 ± 1.8**** **(9)**	**92 ± 2**** **(9)**	**58.4 ± 29.1 (9)**	**5 ± 3**** **(9)**	**592 ± 98*** **(9)**	**3 ± 0.7 (9)**	**690 ± 57 (9)**	-		
Wildtype (2 / **98 K^+**)	6.8 ± 1.7 **4.2 ± 1.2 (6)**	34.9 ± 6.4 **19.8 ± 0.8*** (5)	88 ± 4 **92 ± 3** (5)	136 ± 17.0 **88.5 ± 36.3** (5)	12 ± 4 **8 ± 3** (5)			47.5 ± 5.7 **50.8 ± 10.0** (6)	50 ± 3 **53 ± 6** (6)	1377 ± 189 **568 ± 129**** (6)	50 ± 3 **47 ± 6** (6)
Wildtype (± **TEA**)	8.5 ± 2.8 **5.6 ± 1.3 (5)**	35.7 ± 6.4 **22.3 ± 4.7** (5)	86 ± 3 **91 ± 3** (5)	128 ± 17.4 **120 ± 36** (5)	14 ± 3 **9 ± 3** (5)			48.8 ± 4.4 **38.3 ± 3.6*** (5)	49 ± 1.1 **43 ± 2*** (5)	1279 ± 186 **1206 ± 398** (5)	51 ± 1 **57 ± 2*** (5)
Δ10 (2 / **98 K^+**)	20.4 ± 4.6 **11.9 ± 2.8 (8)**	45.0 ± 7.0 **26.5 ± 2.2*** (6)	78 ± 5 **92 ± 3** (6)	138 ± 14.3 **102 ± 31.4*** (6)	22 ± 5 **9 ± 5** (6)			72.7 ± 16.6 **72.9 ± 13.8** (6)	65 ± 4 **68 ± 7** (6)	1396 ± 339 **671 ± 209*** (6)	35 ± 4 **32 ± 4** (6)
Δ10 (± **TEA**)	22.0 ± 9.1 **15.6 ± 5.6 (6)**	45.8 ± 8.7 **25.9 ± 5.0*** (5)	75 ± 3 **87 ± 3*** (5)	136 ± 18.3 **93.7 ± 15.6*** (5)	25 ± 3 **13 ± 3*** (5)			79.4 ± 11.0 **75.8 ± 12.4** (6)	64 ± 3 **63 ± 3** (6)	1493 ± 248 **1303 ± 275*** (6)	36 ± 3 **37 ± 3** (6)
L400A (2 / **98 K^+**)		39.6 ± 7.8 **24.7 ± 2.4*** (8)	89 ± 3 **91 ± 2*** (8)	532 ± 145 **350 ± 88*** (8)	11 ± 3 **9 ± 2*** (8)			57.0 ± 18.7 **54.8 ± 7.4** (9)	58 ± 5 **71 ± 7*** (9)	1254 ± 266 **883 ± 263*** (9)	42 ± 5 **29 ± 7*** (9)
N408A (2 / **98 K^+**)	5.7 ± 2.1 **1.7 ± 0.1 (5)**	8.4 ± 0.9 **6.7 ± 1.2*** (7)	96 ± 0.8 **94 ± 2*** (7)	355 ± 0.9 **224 ± 124** (7)	4 ± 0.8 **6 ± 2*** (7)			666 ± 63 **310 ± 27*** (5)	-		

Wild-type and mutant Kv4.2 + DPP + 1b channels were expressed in *Xenopus* oocytes, and functional characterization under two-electrode voltage-clamp was performed under different conditions. Mean values ± SD and number of oocytes (n) are given for the time constants of macroscopic inactivation and recovery from inactivation (including relative amplitudes in %; control values in normal K^+ solution shown as grey numbers); recovery voltage: -80 mV. Statistical analyses were done using analysis of variance (ANOVA) and an unpaired Student's *t*-test for mutant effects or a paired Student's *t*-test for comparisons between two groups when the bath solution was changed during recordings from individual oocytes. Both significant mutant effects and significant effects when switching the bath from 2 mM K^+ to 98 mM K^+ or TEA are indicated as *($p<0.05$) or **($p<0.0001$).

5. Discussion

In this study, we aimed to critically revise a previous report regarding the modulation of Kv4 channels by KChIP1 splice variants, especially the distinctive features of the KChIP1b (referred to as 1b). In accordance with a previously reported trend, our results suggest that the ability to enhance the functional surface expression of Kv4 channels is attenuated for 1b in comparison to KChIP1a (referred to as 1a). The previously reported induction of a novel extremely slow recovery component by 1b is confirmed by our results, but in addition, our data reveal that 1a co-expression also causes biphasic recovery kinetics. This universal KChIP1 feature, albeit more pronounced for 1b than for 1a co-expression, is consistently observed for all Kv4.x subtypes, both in a binary configuration and in a ternary configuration with DPP. Kv4.2 + DPP + 1b ternary channels were chosen for a mechanistic study of the slow recovery process.

5.1 Modulation of Kv4 channels by KChIP1 in heterologous systems

Co-expression of an initially identified KChIP1, which is identical to the 1a splice variant used herein, with Kv4.2 in tissue culture cells and *Xenopus* oocytes has defined hallmarks of Kv4 channel modulation by KChIPs. These included an increase in current density, a slowing of macroscopic inactivation, an acceleration of recovery from inactivation and a shift of the voltage of halfmaximal activation to more negative potentials (An et al., 2000). The initially identified KChIP1 was in the focus of a detailed analysis of Kv4 channel assembly and trafficking. In particular, KChIP1 stabilizes the tetramerization of Kv4.3 (Cui et al., 2008), facilitates the release of Kv4.2 from ER retention by assisting the proper folding of its α-subunits hydrophobic domains, and promotes its localization to the cell surface (Hasdemir et al., 2005; Shibata et al., 2003). Additionally, KChIP1-specific N-terminal myristoylation is required for the subcellular targeting of the Kv4.2 + KChIP1 complex to post-ER transport vesicles (O'Callaghan et al., 2005), which together explains the observed increase in current densities upon KChIP1 co-expression. Moreover, the initially identified KChIP1 was used for a detailed biophysical analysis in *Xenopus* oocytes, showing similar remodelling of Kv4.1 and Kv4.3 channel inactivation, which included the typical streamlining effect on macroscopic currents, characterized by a slowing of the early phase of current decay and an acceleration of the late phase, with a crossover of normalized current traces obtained in the absence and presence of KChIP1, respectively (see Figure 4.2 and Figure 4.6). A shift of steady-state inactivation curves to more positive voltages was also

observed, most likely reflecting the accelerated recovery from inactivation (Beck et al., 2002). Our experimental results obtained with 1a co-expression largely confirmed these earlier observations. These effects may be explained by the structure basis of the Kv4 + KChIP1 interaction, in which KChIP1 has been shown to stabilize the S6 conformation and interact with both the C-terminal S6 segment and the N-terminal domain of a neighbouring α-subunit (Kise et al., 2021).

1b, an alternatively spliced variant of KChIP1, contains the N-terminal myristoylation motif required for subcellular targeting, but differs from 1a by the insertion of an extra 11-amino acid at the N-terminus (residues 22 - 33 in 1b; Figure 5.1), which is rich in aromatic side chains (Boland et al., 2003; Pruunsild and Timmusk, 2005; Van Hoorick et al., 2003). Apart from this aromatic cluster, a number of amino acid residues are conserved in KChIP2, KChIP3, and KChIP4 sequences but differ in the KChIP1 sequence. The less conserved N-terminal section of KChIP1 may contribute to the distinct modulation of Kv4 channels by KChIP1 splice variants. Similar to 1a, the 1b splice variant was shown to co-localize with Kv4.2 in the plasma membrane, indicating that 1b also functions as an integral component of A-type channel and contributes to post-ER membrane trafficking (Cui et al., 2008; Hasdemir et al., 2005; O'Callaghan et al., 2005; Shibata et al., 2003). 1b also increased Kv4.2 current density, and slightly lower current densities for Kv4.2 + 1b compared to Kv4.2 + 1a were observed, but the difference proved to be not significant in the original study (Van Hoorick et al., 2003). However, in our experiments using *Xenopus* oocytes injected with defined amounts of Kv4.x and KChIP1 cRNAs, the current upregulation induced by 1b was significantly smaller compared to that by 1a and this observation was not dose-dependent (see Figure 4.1). Of note, in the ternary configuration with DPP, 1b even induced a suppression of current amplitudes. Together, these findings suggest that the distinct 11-amino acid N-terminal aromatic cluster may possibly have an adverse effect on channel trafficking, likely representing an intrinsic property of the 1b splice variant. Although 1a and 1b have a similar overall effect on current decay, they modulate Kv4.2 channels differently in the binary configuration, mainly due to the fractional contribution of each inactivation time component, which is independent of the heterologous expression system used, while this difference tends to disappear in the ternary configuration with DPP. The 1b splice variant has previously been shown to differ substantially from 1a, by inducing biphasic recovery kinetics with an unprecedented extremely slow component. Accordingly, and in contrast to 1a, 1b was shown to shift the Kv4.2 steady-state inactivation curve to more negative voltages

(Van Hoorick et al., 2003).

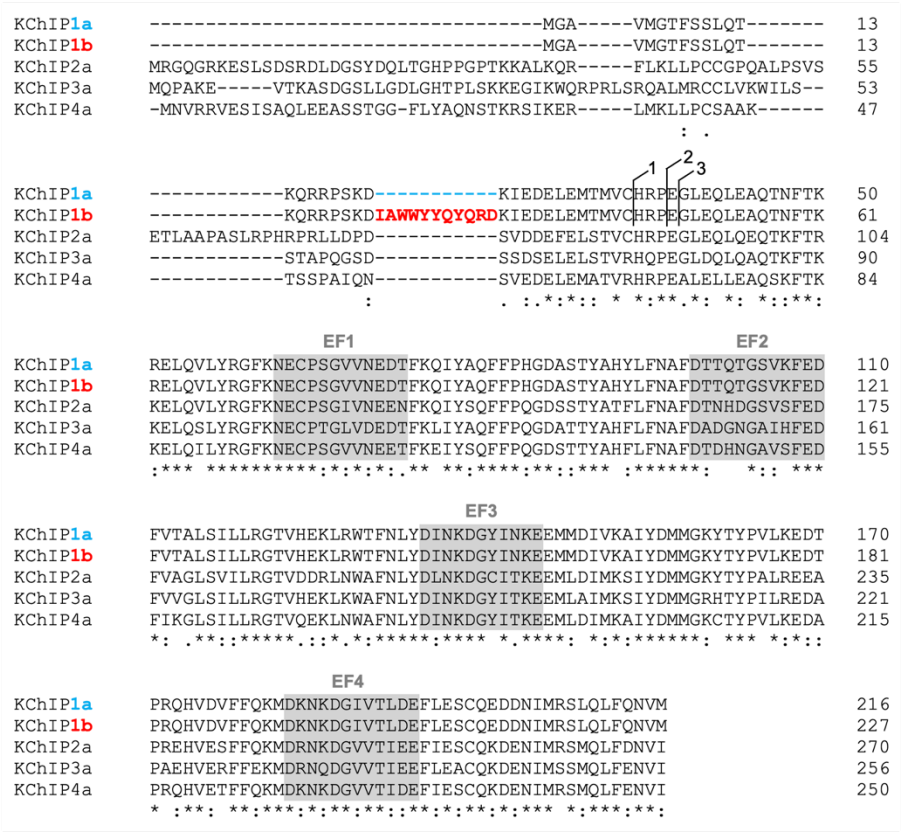

Figure 5.1 KChIP amino acid sequences. Alignment of KChIP1 (Q9NZI2; 1a and 1b splice variant shown), KChIP2a (Q9NS61), KChIP3a (Q9Y2W7) and KChIP4a (Q6PIL6) amino acid sequences created with UniProt (https://www.uniprot.org/); numbers on the right indicate amino acid positions. Residues that are perfectly conserved (*) or exhibit either strong (:) or weak (.) similarity are indicated. Note the highly variable KChIP N-termini but conserved core regions with four EF hand motifs (shaded grey). The eleven amino acid N-terminal aromatic cluster found in KChIP1b (red), but not in KChIP1a (blue), is captured by none of the available KChIP1 3D structures, starting with His34 (1; (Zhou et al., 2004)), Glu37 (2; (Kise et al., 2021)) or Gly38 (3; (Ma et al., 2022; Pioletti et al., 2006; Scannevin et al., 2004; Wang et al., 2007)).

Accordingly, and in contrast to 1a, 1b was shown to shift the Kv4.2 steady-state inactivation curve to more negative voltages (Van Hoorick et al., 2003). Our critical revision of this previous report on the distinctive features of 1b was motivated by the fact that the authors had used transient transfection of a stable Kv4.2-expressing cell-line with KChIP1 cDNA. In this system, cell-to-cell variations in cDNA uptake and differences in the temporal expression profiles of α-(stable) and β-subunits (transient), combined with a possible limited surface expression of 1b-containing channels, may result in the co-existence of two different Kv4.2 channel populations present in the plasma membrane, Kv4.2 alone (stable) and Kv4.2 + 1b, with fast and slow recovery kinetics, respectively. To overcome these limitations, we subjected the previous findings to a rigorous test by re-examining the effects of 1b-coexpression on Kv4.2 recovery kinetics using *Xenopus* oocytes, a system in which the

amount of injected cRNA can be precisely adjusted. However, the previously reported biphasic recovery kinetics were similarly observed, irrespective of the amount of 1b cRNA excess injected (see Figure 4.3). Thus, our results do not support the initial assumption that the expression system significantly influenced the findings. Furthermore, we asked whether the special 1b effect on recovery kinetics is also observed for other Kv4 subtypes, and whether it is still visible in a ternary configuration with DPP. Since DPP itself strongly accelerates the recovery of Kv4 channels from inactivation (Maffie and Rudy, 2008), by stabilizing the voltage sensor S1 and S2 conformations in order to promote the S4 movement (Kise et al., 2021), it may mask the 1b-induced effects. In our experiments, all Kv4 subtypes were co-expressed with excess amounts of 1b, both in a binary configuration and a ternary configuration with DPP, and recording were done on different days after cRNA injection, but the induction of an extremely slow recovery component by 1b was consistently observed, supporting that slowing recovery from inactivation is an intrinsic property of this isoform. This notion is further supported by our findings that the two Kv4.3 splice variants (S and L; Isbrandt et al., 2000), known for their differential modulation by KChIP2 (Abbott, 2017), displayed the same modulation by the 1b splice variant as seen for Kv4.2 and Kv4.1 (see Figure 4.5-Figure 4.8). Apart from 1b, KChIP2e has also been reported to show opposite effect compared to other KChIP isoforms, such as slowing recovery from inactivation of Kv4.3, due to the existence of an alternative exon 10 located at C-terminal (Decher et al., 2004).

Unexpectedly, we found that, similar to 1b, 1a is also capable of inducing a slow recovery component. Notably, most of the previous reports of initially identified KChIP1 co-expression effects on Kv4 channel, both in cDNA-transfected tissue culture cells (Amarillo et al., 2008; An et al., 2000; Bourdeau et al., 2011; Hatano et al., 2002; Van Hoorick et al., 2003; Van Hoorick et al., 2007; Zhou et al., 2004) and in cRNA-injected *Xenopus* oocytes (An et al., 2000; Beck et al., 2002; Boland et al., 2003; Bowlby et al., 2005; Holmqvist et al., 2002; Kaulin et al., 2008; Kise et al., 2021; Nadal et al., 2003; Pioletti et al., 2006; Scannevin et al., 2004; Wang et al., 2007; Zhang et al., 2003), have used a single-exponential function to describe the kinetics of recovery from inactivation. In our recordings, the slow recovery component was less obvious in binary Kv4.x + 1a channels, as the slow recovery time constant was smaller and contributed less to the total recovery process compared to Kv4.x + 1b channels. However, in ternary Kv4.x + DPP + 1a channels, the slow recovery component became more evident (Figure 4.3 and Figure 4.7), which differs from previous

studies on ternary Kv4.2 + DPP + 1a channels in either tissue culture cells (Amarillo et al., 2008) or in *Xenopus* oocytes (Nadal et al., 2003), where recovery kinetics were analysed using only a single-exponential function. Multi-exponential fitting of the 1a-induced recovery kinetics was not considered in these previous studies, despite sometimes the obvious inadequacy of the fitting procedure. It should be noted that in some of the previously used experimental protocols the interpulse durations may have been not long enough to capture such a slow component of recovery from inactivation. Van Hoorick and coworkers further showed that 1b-mediated recovery behavior can be converted into that of 1a-mediated recovery behavior by removal of three aromatic amino acid located on the N-terminal of 1b (Van Hoorick et al., 2007). Of note, a previous study using similar condition as in the present study, also reported that 1a induced biphasic recovery for Kv4.1 and Kv4.2 (Nakamura et al., 2001), consistent with our observations. Furthermore, our study noticed that both binary and ternary configurations containing 1b always exhibited the most negative inactivation curves, likely reflecting the extremely slow recovery kinetics of Kv4 channel complexes with 1b.

5.2 Mechanism of KChIP1-mediated remodelling of Kv4 channel inactivation

Inactivation of voltage-gated K^+ channels is a process, in which channel conductance is shut down during a prolonged or sustained membrane depolarization. This process is essential for controlling the occurrence and shape of action potentials, as well as establishing firing patterns in excitable tissues (Bähring and Covarrubias, 2011). By pure electrophysiological examination and in the absence of any structural correlate, Kv4 channels have been shown early on to undergo preferential CSI at all physiologically relevant membrane potentials. The closed-inactivated state is absorbing, meaning that during moderate depolarization, channels enter it directly from a preopen closed state without opening, whereas during strong depolarization, channels may only transiently open but tend to accumulate in the closed-inactivated state (Bähring et al., 2012; Bähring and Covarrubias, 2011). The conclusion was drawn from identical single-exponential recovery kinetics as well as their voltage dependences obtained for Kv4.2 channels, regardless of whether inactivation was induced at +40 or -50 mV (Bähring et al., 2001a). Different from most other KChIPs, the KChIP1 splice variant 1b causes Kv4 channel gating modulation with biphasic recovery kinetics ((Van Hoorick et al., 2003; Van Hoorick et al., 2007) and present data). For Kv4.2 + DPP + 1b, if inactivation is induced for 3s at +40 mV, allowing channels to open before they

inactivate, recovery from inactivation follows a double-exponential time course. The biphasic recovery kinetics, with both fast and slow recovery components exhibiting a shallow but similar voltage dependence ($q_{app} \approx 0.5$), suggest the presence of two distinct final inactivated states occupying roughly equal fractions of the channels. Intriguingly, if inactivation is induced at -70 mV for 10 s (see Figure 4.9D), without channel opening, recovery from inactivation follows a single-exponential time course, with the time constant and voltage dependence resembling those of the slow component observed in the former situation (recovery after 3 s at +40 mV; see Figure 4.9C). Apparently, Kv4.2 + DPP + 1b ternary channels need to open to exhibit the biphasic recovery kinetics; otherwise, they accumulate exclusively in the novel inactivated state with slow recovery kinetics. If channels are allowed to open, with inactivating voltages more positive than -40 mV, occupancy of the novel inactivated state is decreased with increasingly more depolarized inactivating voltages, suggesting that opening enables the channels to occupy an inactivated state from which recovery occurs rapidly. However, this trend seems to saturate with inactivating voltages around +70 mV (see Figure 4.10C), presumably due to a maximal opening probability. In contrast, if the inactivation is induced with increasingly longer inactivation pulses durations (from 40 ms to 20 s), the channels tend to accumulate in the novel inactivated state, and recovery from inactivation becomes increasingly slower (see Figure 4.10D). Taken together, these findings support the notion that, similar to preferential CSI, channels have to re-close after opening in order to enter the novel inactivated state, and that its entry is slow, while occupancy of an inactivated state with fast recovery is only temporary.

State occupancy kinetics related to the 1b-associated gating modulation has been computer-simulated by Van Hoorick and co-workers (Van Hoorick et al., 2007) using a Markov-chain model, based on the one that had been introduced earlier by Beck and co-workers to describe KChIP1 (= 1a) remodelling of Kv4 channels (Beck et al., 2002). In the adapted model (Figure 5.2A) one additional inactivated state (I_7), directly coupled to the final closed-inactivated state (I_4), was included. This "deeply" inactivated state is only occupied in the presence of KChIP1, with a particularly low exit-rate for 1b modelling (Van Hoorick et al., 2007). This gating model was able to reproduce the experimentally observed biphasic recovery kinetics. Notably, direct coupling of I_4 and I_7 in the model is in accordance with the highly similar voltage dependences of the two recovery time constants observed in our experiments (see Figure 4.9).

The gating model described above cannot explain the structure functional relationships of

the 1b-mediated inactivation behavior. Experimental evidences have identified three major inactivation mechanisms in Kv channels. Besides CSI, which is prominent in Kv4 channels (Bähring and Covarrubias, 2011), two other mechanisms of inactivation are utilized in many Kv channels, including N-type inactivation, where the open channel is blocked by an intrinsic N-terminal inactivation domain from the cytoplasmic side (Armstrong and Hollingworth, 2017), and/or P/C-type inactivation, involving conformational rearrangements of the external pore mouth near the selectivity filter (Hoshi and Armstrong, 2013). In *Shaker*-related (Kv1) channels CSI plays a minor role, whereas N- and P/C-type inactivation are the major pathways of inactivation. N-type inactivation is faster than P/C-type inactivation and dominates the current decay, while slow P/C-type inactivation controls the rate of recovery from inactivation because its rate-limiting properties (Bett et al., 2011). These classical *Shaker* inactivation mechanisms are also present in Kv4 channels in vestigial form (Gebauer et al., 2004; Kaulin et al., 2008), and may be enhanced by 1b co-expression to introduce the novel inactivated state. Several approaches were used in our study to test this possibility. Our data confirmed that N-type inactivation is not involved in the biphasic recovery kinetics, since a ten amino acid N-terminal truncation on Kv4.2 + DPP + 1b channel showed similar recovery behaviours to that of wild-type channels (see Figure 4.12B). Interestingly, elevated external K^+ specifically accelerated the slow component of the biphasic recovery process in our study (see Figure 4.13). The acceleration of recovery from inactivation observed in the elevated external K^+ is similar to what has been reported in typical P/C-type inactivation channels such as Kv1.3 (Levy and Deutsch, 1996) and Kv1.4 (Rasmusson et al., 1995), suggesting that the novel deeply inactivated state of Kv4 channels induced by 1b is related to P/C-type inactivation. Kaulin and co-workers previously reported the presence of P/C-type inactivation features in Kv4 + KChIP1 (= 1a) channels, observing that the inactivation of Kv4 + 1a was accelerated by elevated external K^+ (Kaulin et al., 2008), which supports the assumption that removal of vestigial P/C-type inactivation allows the channels to accumulate faster in the closed-inactivated state (Bähring et al., 2001a; Jerng and Covarrubias, 1997; Kaulin et al., 2008; Kirichok et al., 1998; Shahidullah and Covarrubias, 2003). Similarly, Eghbali and coworkers revealed that Kv4.3 exhibits P/C-type inactivation as removal of external K^+ destabilized the conducting state and accelerated the inactivation rate, leading to the collapse of the pore (Eghbali et al., 2002). To mechanistically explain these observations, Kaulin and coworkers introduced a corresponding gating model, (Figure 5.2B) showing that the main activation pathway (C_0 ... C_5, O) is paralleled not only

by a chain of closed-inactivated states (I_0 ... I_5), but also by a chain of P/C-type inactivated states (P_0 ... P_6). The main activation pathway runs between the two inactivation chains, indicating that each closed state has the chance to undergo either P/C-type inactivation or CSI, whereas the open state can only undergo P/C-type inactivation. In this model, the channels will not accumulate permanently in the P/C-type inactivated states, reflecting a relatively stable selectivity filter conformation of Kv4 channels. Of note, this model (Kaulin et al., 2008) substantially differs from the model suggested by Van Hoorick and co-workers (Van Hoorick et al., 2007), in that two optional inactivated states are directly coupled in the latter but not in the former (Figure 5.2A and 5.2B).

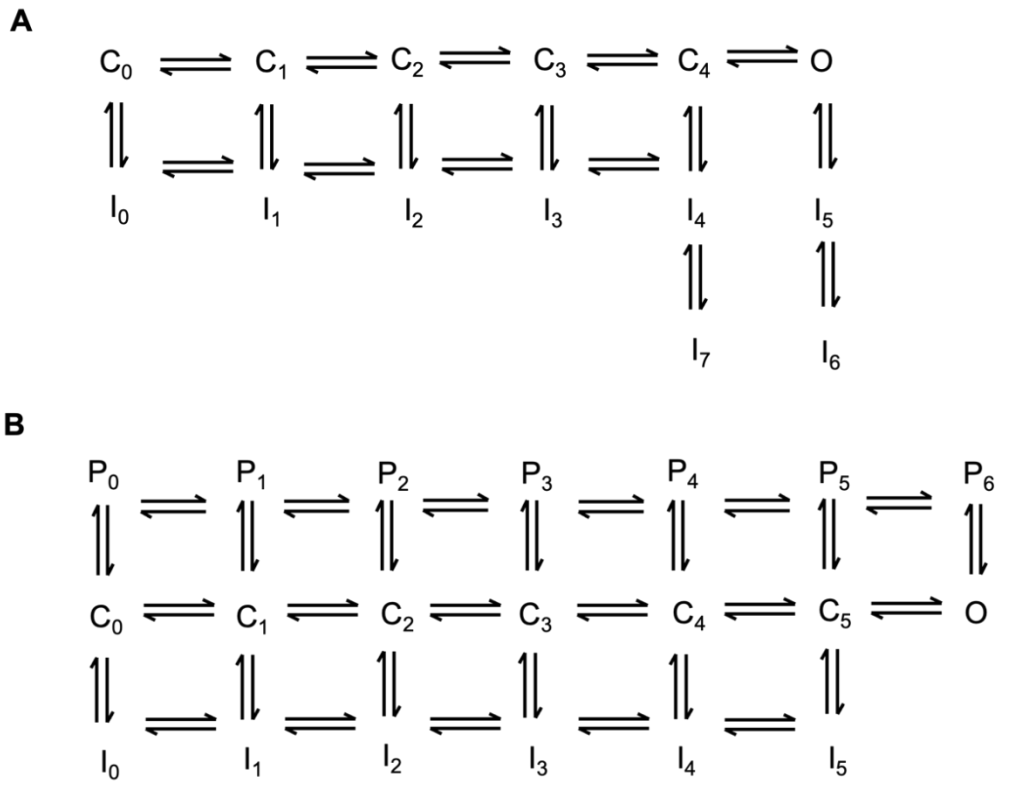

Figure 5.2 Modified Kv4 channel gating schemes. A: A model introduces one additional inactivated state (I_7), directly coupled to the final closed-inactivated state (I_4) adopted from Van Hoorick *et al.* (2007). C, closed-state, main activation pathway; O, open state; I, closed-inactivated state. B: A model introduces two parallel inactivation pathways adopted from Kaulin *et al.* (2008). C, closed-state, main activation pathway; P, P/C-type inactivated states; I, closed-inactivated state.

These functional observations promoted investigations into the structural basis of Kv channel inactivation. Recently, high resolution cryo-EM data provided detailed structural insights into P/C-type inactivation in Kv1.2 channels, suggesting a dilation instead of a constriction of the selectivity filter on the external side in the P/C-type inactivated states (Reddi et al., 2022). Moreover, isoleucine residues at position 398 (I398) along the pore lining segment S6 from four subunits seem to act as a state-dependent hydrophobic gate that

blocks K^+ conduction in P/C-type inactivation (Treptow et al., 2024). Another high resolution cryo-EM data elucidated the inactivation mechanisms of Kv4.2 channels. Upon inactivation, the homo-tetrameric channel pore loses its 4-fold symmetry and becomes 2-fold symmetric, accomplished by the coupling of the S4-S5 linker to both upper (Ile398) and lower gates (Val402). This conformational change produces a tight constriction that blocks K^+ conduction. They also reported that KChIP2 and DPP6 modulated gating properties but did not directly interact with the upper and lower gates, indicating the unprecedented symmetry breakdown for pore closure is an intrinsic feature of Kv4 channel alone (Ye et al., 2022). The lower gate involves the dynamic coupling between voltage sensors and gate modules (Barghaan and Bähring, 2009), leading to a symmetry breakdown of S6-segments, which underlies Kv4 channel CSI (Barghaan and Bähring, 2009; Ye et al., 2022). Intriguingly, Kv4.2 residue I398 corresponds to the conserved isoleucine gate responsible for Kv1 channel P/C-type inactivation (Treptow et al., 2024). Thus, based on these structural similarities, we speculate that in the presence of the 1b, the upper (isoleucine) gate in Kv4.2 channels may evolve into a major inactivation gate (P/C-type inactivation), especially if S6-related CSI (lower gate) is unstable, as suggested by our experimental findings with the N408A mutant (Figure 4.15).

Apart from the role of KChIPs in modulating Kv4 N-type inactivation by interacting with Kv4.2 proximal N-terminus (Gebauer et al., 2004), the structure-function relationships of Kv4 channel remodelling by KChIPs remain largely unknown. High resolution 3D structures involving KChIP1 have shown that the β-subunit also binds to the T-domain and to the cytoplasmic C-terminus of Kv4 channel α-subunits. However, the extra aromatic cluster inserted into the N-terminal domain of KChIP1 by alternative splicing, which is thought to be responsible for the special Kv4 remodelling by 1b (Van Hoorick et al., 2003; Van Hoorick et al., 2007) is not included in any of the KChIP1 structures available to date (Kise et al., 2021; Ma et al., 2022; Pioletti et al., 2006; Scannevin et al., 2004; Wang et al., 2007; Zhou et al., 2004; see also Figure 5.1). Thus, a putative interaction interface with the Kv4 α-subunit remains largely undefined.

It is intriguing that the naturally occurring Kv1.5 Δ209 N-terminal truncation variant exhibits not only classical P/C-type inactivation but also a form of CSI, which results in biphasic recovery from inactivation (Kurata et al., 2005). Notably, the Kv1.5 Δ209 variant lacks the T-domain, a configuration which apparently favors CSI. In the presence of a T-domain, Kv1.5 exhibits only classical P/C-type inactivation. Possibly, the presence and stabilization

of T-domains, for example by the clamping action of KChIP1 (Cui et al., 2008), may favor P/C-type inactivation.

5.3 Distribution and physiology of KChIP1-expressing neurons

Kv4 channels mediate the subthreshold activating somatodendritic A-type current (I_{SA}; Pak et al., 1991; Wei et al., 1990), a transient current widely expressed in excitable neurons (Jerng and Pfaffinger, 2014). I_{SA} plays a key role in regulating the neuronal excitability, controlling the firing frequency and action potential back-propagation, and influencing synaptic plasticity and integration (Hoffman et al., 1997). Kv4 channels require both of auxiliary β-subunits, KChIPs and DPPs, to achieve native A-type currents (Rhodes et al., 2004). In fact, Kv4 + KChIP + DPP ternary channels are thought to underlie a major portion of I_{SA} (Amarillo et al., 2008; Jerng et al., 2005; Jerng and Pfaffinger, 2012; Maffie and Rudy, 2008). The variety of β-subunit splice variants and their interaction with Kv4 α-subunits jointly contribute to the diversity of I_{SA} properties in different cell types with a considerable impact on neuronal excitability and discharge behavior (Jerng and Pfaffinger, 2014). Immunohistochemical and biochemical studies have shown that that the expression and localization profiles of Kv4 α-subunits, KChIPs and DPPs exhibit distinct distributions in the brain, but also considerable overlap, allowing a prediction of possible likely combinations (Clark et al., 2008; Rhodes et al., 2004; Xiong et al., 2004; Zagha et al., 2005). Specifically, Kv4.3 and KChIP1 are primarily co-localized in the somata and dendrites of hippocampal, striatal, and neocortical interneurons (Rhodes et al., 2004), and electron microscopic analysis further revealed that KChIP1 and Kv4.2 immunoreactivity is co-localized at the plasma membrane of cerebellar granule cell somata and dendrites (Strassle et al., 2005). In addition to its co-localization with Kv4 α-subunits, KChIP1 itself is highly expressed in a specific group of neurons throughout the brain, particularly in Purkinje cells of the cerebellum and in the reticular thalamic and medial habenular nuclei. Notably, in the reticular thalamic nucleus, only Kv4.2 transcripts are reported, suggesting the distinct interaction between KChIP1 and different Kv4 channels (Xiong et al., 2004). Consistent with these patterns, Kv4.3 and DPP6 are co-expressed in Purkinje cells, substantia nigra, and the periglomerular region of the olfactory bulb (Malloy et al., 2022). Of note, these initial studies on the distributions of KChIP1 in the brain did not distinguish between the 1a and 1b splice variants, and currently no specific researches have investigated co-localization of different KChIP1 splice variants with Kv4 channels and DPPs in the brain. However, several

other studies reported that both 1a and 1b are expressed in different brain regions with distinct abundances. 1a is broadly expressed across all examined human brain regions, such as cerebellum, hippocampus, striatum, and cerebral cortex (Pruunsild and Timmusk, 2005), and 1b has also been detected in the corresponding brain regions in mice (Boland et al., 2003; Van Hoorick et al., 2003; Xia et al., 2010), but the expression profiles of 1b in different human brain regions have not been clearly reported so far. Interestingly, 1a and 1b show different distributions in peripheral human tissues (Van Hoorick et al., 2003). These findings suggest that both KChIP1 splice variants may play equally important roles in shaping the properties of I_{SA}, as they can interact stably with Kv4.2 channels.

Apart from a component of I_{SA}, KChIP1 was highly co-localized with GABA transmitters in hippocampus and cerebral cortex, and potentiates GABA-mediated inhibitory synaptic transmission by increasing presynaptic GABA release. KChIP1 facilitates inhibitory synaptic transmission in neurons by inhibiting potassium channel activity rather than by enhancing calcium channel currents (Xia et al., 2010). In KChIP1-deficient mice, susceptibility to PTZ-induced epilepsy seizure, suggesting that increasing expression of KChIP1 strengthens GABAergic neurons activities and inhibits moto seizure pathways (Su et al., 2008; Xiong et al., 2009). Bourdeau and coworkers used short interfering RNA (siRNA) to down-regulate KChIP1 expression in order to investigate its contribution to I_{SA} properties and cellular excitability. In hippocampal interneurons, suppression of KChIP1 by siRNA moderately reduced peak I_{SA} and slowdown recovery from inactivation. In addition, siRNA-mediated knockdown of KChIP1 did not affect individual action potential waveform, but accelerates repetitive firing frequency during suprathreshold depolarizations, indicating that KChIP1 regulates interneuron excitability and enhances inhibitory control of firing during sustained activity (Bourdeau et al., 2011). Our data indicate that 1b is less effective than 1a in enhancing surface expression and slowing macroscopic inactivation, and has the opposite effect on recovery kinetics and steady-state inactivation, indicating that these two KChIP1 splice variants might also act as competitive inhibitors to regulate I_{SA} properties and modulate membrane excitability.

Taken together, we hypothesize that some KChIP1-expressing inhibitory neurons may rely more on 1a splice variant to maintain the low excitability, while the presence of 1b splice variant may reduce I_{SA} availability and thereby control of excitability and discharge behavior. Therefore, the variety of KChIP splice variants may contribute to the diversity of physiological roles of I_{SA} in different neuronal populations.

6. Summary

6.1 Summary

Voltage-gated potassium channels of the Kv4 subfamily mediate a somatodendritic A-type current, which controls repetitive firing, dendritic excitation and synaptic plasticity. Kv4 channels form complexes with two types of auxiliary β-subunits, DPPs and KChIPs, which enhance channel surface expression and modify channel gating. Although ternary Kv4 channel complexes (Kv4 + DPP + KChIP) resemble native channel configuration, our knowledge about the concerted modulation of channel properties by DPPs and KChIPs, especially by certain β-subunit splice variants, is fragmentary. Here, we studied the modulatory effects of two functionally distinct KChIP1 splice variants (1a and 1b), utilizing two-electrode voltage-clamp in the *Xenopus* oocyte expression system. We tested Kv4.1, Kv4.2, Kv4.3S, and Kv4.3L co-expressed with the two KChIP1 splice variants, both in a binary (Kv4 + KChIP1) and in a ternary channel configuration (Kv4 + DPP + KChIP1). We observed that in binary channels a stronger peak current amplitude increase for 1a than for 1b co-expression. Both KChIP1 splice variants induced an extremely slow component of recovery from inactivation, which was more prominent for 1b co-expression. In a ternary configuration with DPP, peak current amplitude could be suppressed by KChIP1 splice variants, but the induction of an extremely slow recovery component by both 1a and 1b persisted. For Kv4.2 + DPP + 1b ternary channels, the relative amplitude of the slow recovery component increased from 40% up to 100% with longer and less depolarized inactivating pulses, suggesting a distinctive state dependence of slow recovery kinetics. Further mechanistic investigations revealed that the normally vestigial P/C-type inactivation in Kv4 channels may play a crucial role in 1b-mediated biphasic recovery kinetics. Thus, the special regulation by 1b is general applicable and observed for all Kv4 channel subtypes and in a ternary configuration with DPP, independent of the utilized expression system and recording technique. Our results corroborate the distinct functional roles of KChIP1 splice variants, by critically controlling the time-dependent availability of the somatodendritic A-type potassium current in neurons.

6.2 Zussamenfassung

Spannungsgesteuerte Kaliumkanäle der Kv4-Unterfamilie vermitteln einen somatodendritischen A-Typ-Strom, der repetitives Feuern, dendritische Erregung und synaptische Plastizität steuert. Kv4-Kanäle bilden Komplexe mit zwei Arten von zusätzlichen β-Untereinheiten, DPPs und KChIPs, die die Expression des Kanal-Gating verstärken und die Kanalsteuerung modifizieren. Unser Wissen darüber, wie DPPs und KChIPs, insbesondere bestimmte β-Untereinheit-Spleißvarianten, gemeinsam die Eigenschaften ternärer Kv4-Kanalkomplexe modulieren, ist noch unvollständig. Hier untersuchten wir die modulatorischen Effekte zweier funktionell unterschiedlicher KChIP1-Spleißvarianten (1a und 1b) unter Verwendung einer Zweielektroden-Spannungsklemme im *Xenopus*-Oozyten-Expressionssystem. Wir testeten Kv4.1, Kv4.2, Kv4.3S und Kv4.3L in Koexpression mit den beiden KChIP1-Spleißvarianten, sowohl in einer binären als auch in einer ternären Kanalkonfiguration. Wir beobachteten, dass in binären Kanälen die Zunahme der Spitzenstromamplitude für die Koexpression von 1a größer war als für die Koexpression von 1b. Beide KChIP1-Spleißvarianten führten zu einer sehr langsamen Erholung von der Inaktivierung, wobei dieser Effekt bei 1b stärker ausgeprägt war. In der ternären Konfiguration konnte KChIP1 die Spitzenstromamplituden unterdrücken, jedoch blieb die Induktion der extrem langsamen Erholungskomponente durch sowohl 1a als auch 1b bestehen. Bei ternären Kanälen (Kv4.2 + DPP + 1b) nahm die relative Amplitude der langsamen Erholungskomponente mit längeren und weniger depolarisierten inaktivierenden Pulsen von 40 % auf 100 % zu, was auf eine starke Zustandsabhängigkeit der langsamen Erholungskinetik hinweist. Mechanistische Untersuchungen zeigten, dass die normalerweise rudimentäre P/C-Typ-Inaktivierung in Kv4-Kanälen eine zentrale Rolle in der 1b-vermittelten biphasischen Erholungskinetik spielen könnte. Diese spezifische Regulation durch 1b ist allgemein gültig und tritt in allen Kv4-Kanalsubtypen sowie in ternären Konfigurationen mit DPP auf – unabhängig vom Expressionssystem oder der Messtechnik. Unsere Ergebnisse bestätigen die wichtige funktionelle Rolle der KChIP1 Splice-Varianten, welche die zeitabhängige Verfügbarkeit des somatodendritischen A-Typ-Kaliumstroms in gezielt steuern.

7. References

Abbott, G.W., 2017. β-subunits functionally differentiate human Kv4.3 potassium channel splice variants. Front. Physiol. 8, 66.

Alfaro-Ruíz, R., Aguado, C., Martín-Belmonte, A., Moreno-Martínez, A.E., Luján, R., 2020. Cellular and subcellular localisation of Kv4-associated KChIP proteins in the rat cerebellum. Int. J. Mol. Sci. 21, 6403.

Amarillo, Y., De Santiago-Castillo, J.A., Dougherty, K., Maffie, J., Kwon, E., Covarrubias, M., Rudy, B., 2008. Ternary Kv4.2 channels recapitulate voltage-dependent inactivation kinetics of A-type K^+ channels in cerebellar granule neurons. J. Physiol. 586, 2093–2106.

An, W.F., Bowlby, M.R., Betty, M., Cao, J., Ling, H.-P., Mendoza, G., Hinson, J.W., Mattsson, K.I., Strassle, B.W., Trimmer, J.S., Rhodes, K.J., 2000. Modulation of A-type potassium channels by a family of calcium sensors. Nature 403, 553–556.

Armstrong, C.M., Hollingworth, S., 2017. A perspective on Na and K channel inactivation. J. Gen. Physiol. 150, 7–18.

Attali, B., 2009. The somatodendritic A-type K^+ channel complex: A Ménage à Trois. Front. Neurosci. 3, 158–159.

Bähring, R., 2018. Kv channel-interacting proteins as neuronal and non-neuronal calcium sensors. Channels 12, 187–200.

Bähring, R., Barghaan, J., Westermeier, R., Wollberg, J., 2012. Voltage sensor inactivation in potassium channels. Front. Pharmacol. 3, 100.

Bähring, Robert, Boland, L.M., Varghese, A., Gebauer, M., Pongs, O., 2001a. Kinetic analysis of open- and closed-state inactivation transitions in human Kv4.2 A-type potassium channels. J. Physiol. 535,

Bähring, R., Covarrubias, M., 2011. Mechanisms of closed-state inactivation in voltage-gated ion channels: Inactivation in voltage-gated ion channels. J. Physiol. 589, 461–479.

Bähring, R., Dannenberg, J., Peters, H.C., Leicher, T., Pongs, O., Isbrandt, D., 2001b. Conserved Kv4 N-terminal domain critical for effects of Kv channel-interacting protein 2.2 on channel expression and gating. J. Biol. Chem. 276, 23888–23894.

Barghaan, J., Bähring, R., 2009. Dynamic coupling of voltage sensor and gate involved in closed-state inactivation of Kv4.2 channels. J. Gen. Physiol. 133, 205–224.

Baumgartner, W., Islas, L., Sigworth, F.J., 1999. Two-microelectrode voltage clamp of

Xenopus oocytes: voltage errors and compensation for local current flow. Biophys. J. 77, 1980–1991.

Beck, E.J., Bowlby, M., An, W.F., Rhodes, K.J., Covarrubias, M., 2002. Remodelling inactivation gating of Kv4 channels by KChIP1, a small-molecular-weight calcium-binding protein. J. Physiol. 538, 691–706.

Bett, G.C.L., Dinga-Madou, I., Zhou, Q., Bondarenko, V.E., Rasmusson, R.L., 2011. A model of the interaction between N-type and C-type inactivation in Kv1.4 channels. Biophys. J. 100, 11–21.

Bezerra, G.A., Dobrovetsky, E., Seitova, A., Fedosyuk, S., Dhe-Paganon, S., Gruber, K., 2015. Structure of human dipeptidyl peptidase 10 (DPPY): a modulator of neuronal Kv4 channels. Sci. Rep. 5, 8769.

Birnbaum, S.G., Varga, A.W., Yuan, L.-L., Anderson, A.E., Sweatt, J.D., Schrader, L.A., 2004. Structure and function of Kv4-family transient potassium channels. Physiol. Rev. 84, 803–833.

Boland, L.M., Jiang, M., Lee, S.Y., Fahrenkrug, S.C., Harnett, M.T., O'Grady, S.M., 2003. Functional properties of a brain-specific NH2-terminally spliced modulator of Kv4 channels. Am. J. Physiol.-Cell Physiol. 285, C161–C170.

Bourdeau, M.L., Laplante, I., Laurent, C.E., Lacaille, J.-C., 2011. KChIP1 modulation of Kv4.3-mediated A-type K^+ currents and repetitive firing in hippocampal interneurons. Neuroscience 176, 173–187.

Bowlby, M.R., Chanda, P., Edris, W., Hinson, J., Jow, F., Katz, A.H., Kennedy, J., Krishnamurthy, G., Pitts, K., Ryan, K., Zhang, H., Greenblatt, L., 2005. Identification and characterization of small molecule modulators of KChIP/Kv4 function. Bioorg. Med. Chem. 13, 6112–6119.

Buckingham, S.D., Kidd, J.F., Law, R.J., Franks, C.J., Sattelle, D.B., 2005. Structure and function of two-pore-domain K^+ channels: contributions from genetic model organisms. Trends Pharmacol. Sci. 26, 361–367.

Callsen, B., Isbrandt, D., Sauter, K., Hartmann, L.S., Pongs, O., Bähring, R., 2005. Contribution of N- and C-terminal channel domains to Kv channel interacting proteins in a mammalian cell line: Kv4/KChIP interaction. J. Physiol. 568, 397–412.

Carrasquillo, Y., Burkhalter, A., Nerbonne, J.M., 2012. A-type K^+ channels encoded by Kv4.2, Kv4.3 and Kv1.4 differentially regulate intrinsic excitability of cortical pyramidal neurons. J. Physiol. 590, 3877–3890.

Carrión, A.M., Link, W.A., Ledo, F., Mellström, B., Naranjo, J.R., 1999. DREAM is a Ca^{2+}-regulated transcriptional repressor. Nature 398, 80–84.

Chen, J., Avdonin, V., Ciorba, M.A., Heinemann, S.H., Hoshi, T., 2000. Acceleration of P/C-type Inactivation in voltage-gated K^+ Channels by methionine oxidation. Biophys. J. 78, 174–187.

Choi, K.L., Aldrich, R.W., Yellen, G., 1991. Tetraethylammonium blockade distinguishes two inactivation mechanisms in voltage-activated K^+ channels. Proc. Natl. Acad. Sci. U. S. A. 88, 5092–5095.

Clark, B.D., Kwon, E., Maffie, J., Jeong, H.-Y., Nadal, M., Strop, P., Rudy, B., 2008. DPP6 localization in brain supports function as a Kv4 channel associated protein. Front. Mol. Neurosci. 1.

Coetzee, W.A., Amarillo, Y., Chiu, J., Chow, A., Lau, D., McCORMACK, T., Morena, H., Nadal, M.S., Ozaita, A., Pountney, D., Saganich, M., De Miera, E.V.-S., Rudy, B., 1999. Molecular diversity of K^+ channels. Ann. N. Y. Acad. Sci. 868, 233–255.

Covarrubias, M., Bhattacharji, A., De Santiago-Castillo, J.A., Dougherty, K., Kaulin, Y.A., Na-Phuket, T.R., Wang, G., 2008. The neuronal Kv4 channel complex. Neurochem. Res. 33, 1558–1567.

Cui, Y.Y., Liang, P., Wang, K.W., 2008. Enhanced trafficking of tetrameric Kv4.3 channels by KChIP1 clamping. Neurochem. Res. 33, 2078–2084.

Dascal, N., 2000. Voltage clamp recordings from *Xenopus* oocytes. Curr. Protoc. Neurosci. 10, 6.12.1-6.12.20.

Dascal, N., 1987. The use of *Xenopus* oocytes for the study of ion channels. CRC Crit. Rev. Biochem. 22, 317–387.

Decher, N., Barth, A.S., Gonzalez, T., Steinmeyer, K., Sanguinetti, M.C., 2004. Novel KChIP2 isoforms increase functional diversity of transient outward potassium currents. J. Physiol. 557, 761.

Demo, S.D., Yellen, G., 1991. The inactivation gate of the *Shaker* K^+ channel behaves like an open-channel blocker. Neuron 7, 743–753.

Dolga, A.M., Terpolilli, N., Kepura, F., Nijholt, I.M., Knaus, H.-G., D'Orsi, B., Prehn, J.H.M., Eisel, U.L.M., Plant, T., Plesnila, N., Culmsee, C., 2011. KCa2 channels activation prevents $[Ca^{2+}]i$ deregulation and reduces neuronal death following glutamate toxicity and cerebral ischemia. Cell Death Dis. 2, e147–e147.

Doyle, D.A., Cabral, J.M., Pfuetzner, R.A., Kuo, A., Gulbis, J.M., Cohen, S.L., Chait, B.T.,

MacKinnon, R., 1998. The structure of the potassium channel: molecular basis of K^+ conduction and selectivity. Science 280, 69–77.

Eghbali, M., Olcese, R., Zarei, M.M., Toro, L., Stefani, E., 2002. External pore collapse as an inactivation mechanism for Kv4.3 K^+ channels. J. Membr. Biol. 188, 73–86.

Enyedi, P., Czirják, G., 2010. Molecular background of leak K^+ currents: two-pore domain potassium channels. Physiol. Rev. 90, 559–605.

Foeger, N.C., Wang, W., Mellor, R.L., Nerbonne, J.M., 2013. Stabilization of Kv4 protein by the accessory K^+ channel interacting protein 2 (KChIP2) subunit is required for the generation of native myocardial fast transient outward K^+ currents. J. Physiol. 591, 4149.

Gebauer, M., Isbrandt, D., Sauter, K., Callsen, B., Nolting, A., Pongs, O., Bähring, R., 2004. N-type inactivation features of Kv4.2 channel gating. Biophys. J. 86, 210–223.

Goldstein, S.A., Price, L.A., Rosenthal, D.N., Pausch, M.H., 1996. ORK1, a potassium-selective leak channel with two pore domains cloned from *Drosophila melanogaster* by expression in *Saccharomyces cerevisiae*. Proc. Natl. Acad. Sci. U. S. A. 93, 13256–13261.

González, C., Baez-Nieto, D., Valencia, I., Oyarzún, I., Rojas, P., Naranjo, D., Latorre, R., 2012. K^+ channels: Function-structural overview. Comprehensive Physiology. Wiley, pp. 2087–2149.

Grizel, A.V., Glukhov, G.S., Sokolova, O.S., 2014. Mechanisms of activation of voltage-gated potassium channels. Acta Naturae 6, 10–26.

Guo, D., Ramu, Y., Klem, A.M., Lu, Z., 2003. Mechanism of rectification in inward-rectifier K^+ Channels. J. Gen. Physiol. 121, 261–276.

Gurdon, J.B., Lane, C.D., Woodland, H.R., Marbaix, G., 1971. Use of frog eggs and oocytes for the study of messenger RNA and its translation in living cells. Nature 233, 177–182.

Gutman, G.A., Chandy, K.G., Grissmer, S., Lazdunski, M., McKinnon, D., Pardo, L.A., Robertson, G.A., Rudy, B., Sanguinetti, M.C., Stühmer, W., Wang, X., 2005. International Union of Pharmacology. LIII. Nomenclature and molecular relationships of voltage-gated potassium channels. Pharmacol. Rev. 57, 473–508.

Halliwell, J., Plant, T., Robbins, J., Standen, N., 1999. 17 Chapter 2 Voltage clamp techniques.

Hasdemir, B., Fitzgerald, D.J., Prior, I.A., Tepikin, A.V., Burgoyne, R.D., 2005. Traffic of

Kv4 K^+ channels mediated by KChIP1 is via a novel post-ER vesicular pathway. J. Cell Biol. 171, 459.

Hatano, N., Ohya, S., Imaizumi, Y., 2002. Functional interaction between KChIP1 and GFP-fused Kv4.3L co-expressed in HEK293 cells. Pflugers Arch. 444, 80–88.

Heginbotham, L., Lu, Z., Abramson, T., MacKinnon, R., 1994. Mutations in the K^+ channel signature sequence. Biophys. J. 66, 1061–1067.

Hibino, H., Inanobe, A., Furutani, K., Murakami, S., Findlay, I., Kurachi, Y., 2010. Inwardly rectifying potassium channels: their structure, function, and physiological roles. Physiol. Rev. 90, 291–366.

Hille, B., 2001. Ion Channels of Excitable Membranes, Third Edition. Oxford University Press, Oxford, New York.

Hodgkin, A.L., Huxley, A.F., Katz, B., 1952. Measurement of current-voltage relations in the membrane of the giant axon of *Loligo*. J. Physiol. 116, 424–448.

Hoffman, D.A., Magee, J.C., Colbert, C.M., Johnston, D., 1997. K^+ channel regulation of signal propagation in dendrites of hippocampal pyramidal neurons. Nature 387, 869–875.

Holmqvist, M.H., Cao, J., Hernandez-Pineda, R., Jacobson, M.D., Carroll, K.I., Sung, M.A., Betty, M., Ge, P., Gilbride, K.J., Brown, M.E., Jurman, M.E., Lawson, D., Silos-Santiago, I., Xie, Y., Covarrubias, M., Rhodes, K.J., Distefano, P.S., An, W.F., 2002. Elimination of fast inactivation in Kv4 A-type potassium channels by an auxiliary subunit domain. Proc. Natl. Acad. Sci. 99, 1035–1040.

Hoshi, T., Armstrong, C.M., 2013. C-type inactivation of voltage-gated K^+ channels: Pore constriction or dilation? J. Gen. Physiol. 141, 151–160.

Hoshi, T., Zagotta, W.N., Aldrich, R.W., 1990. Biophysical and molecular mechanisms of *Shaker* potassium channel inactivation. Science 250, 533–538.

Huang, H.-Y., Cheng, J.-K., Shih, Y.-H., Chen, P.-H., Wang, C.-L., Tsaur, M.-L., 2005. Expression of A-type K^+ channel α subunits Kv4.2 and Kv4.3 in rat spinal lamina II excitatory interneurons and colocalization with pain-modulating molecules. Eur. J. Neurosci. 22, 1149–1157.

Huo, R., Sheng, Y., Guo, W.-T., Dong, D.-L., 2014. The potential role of Kv4.3 K^+ channel in heart hypertrophy. Channels 8, 203–209.

Isbrandt, Dirk, Leicher, T., Waldschütz, R., Zhu, X., Luhmann, U., Michel, U., Sauter, K., Pongs, O., 2000. Gene structures and expression profiles of three human *KCND* (Kv4)

potassium channels mediating A-type currents I_{TO} and I_{SA}. Genomics 64, 144–154.

Jerng, H.H., Covarrubias, M., 1997. K^+ channel inactivation mediated by the concerted action of the cytoplasmic N- and C-terminal domains. Biophys. J. 72, 163–174.

Jerng, H.H., Kunjilwar, K., Pfaffinger, P.J., 2005. Multiprotein assembly of Kv4.2, KChIP3 and DPP10 produces ternary channel complexes with I_{SA}-like properties. J. Physiol. 568, 767.

Jerng, H.H., Lauver, A.D., Pfaffinger, P.J., 2007. DPP10 splice variants are localized in distinct neuronal populations and act to differentially regulate the inactivation properties of Kv4-based ion channels. Mol. Cell. Neurosci. 35, 604–624.

Jerng, H.H., Pfaffinger, P.J., 2014. Modulatory mechanisms and multiple functions of somatodendritic A-type K^+ channel auxiliary subunits. Front. Cell. Neurosci. 8, 82.

Jerng, H.H., Pfaffinger, P.J., 2012. Incorporation of DPP6a and DPP6K variants in ternary Kv4 channel complex reconstitutes properties of A-type K current in rat cerebellar granule cells. PloS One 7, e38205.

Jerng, H.H., Pfaffinger, P.J., Covarrubias, M., 2004. Molecular physiology and modulation of somatodendritic A-type potassium channels. Mol. Cell. Neurosci. 27, 343–369.

Jerng, H.H., Shahidullah, M., Covarrubias, M., 1999. Inactivation gating of Kv4 potassium channels. J. Gen. Physiol. 113, 641–660.

Johnston, D., Christie, B.R., Frick, A., Gray, R., Hoffman, D.A., Schexnayder, L.K., Watanabe, S., Yuan, L.-L., 2003. Active dendrites, potassium channels and synaptic plasticity. Philos. Trans. R. Soc. Lond. B. Biol. Sci. 358, 667–674.

Kalm, T., Schob, C., Völler, H., Gardeitchik, T., Gilissen, C., Pfundt, R., Klöckner, C., Platzer, K., Klabunde-Cherwon, A., Ries, M., Syrbe, S., Beccaria, F., Madia, F., Scala, M., Zara, F., Hofstede, F., Simon, M.E.H., van Jaarsveld, R.H., Oegema, R., van Gassen, K.L.I., Holwerda, S.J.B., Barakat, T.S., Bouman, A., van Slegtenhorst, M., Álvarez, S., Fernández-Jaén, A., Porta, J., Accogli, A., Mancardi, M.M., Striano, P., Iacomino, M., Chae, J.-H., Jang, S., Kim, S.Y., Chitayat, D., Mercimek-Andrews, S., Depienne, C., Kampmeier, A., Kuechler, A., Surowy, H., Bertini, E.S., Radio, F.C., Mancini, C., Pizzi, S., Tartaglia, M., Gauthier, L., Genevieve, D., Tharreau, M., Azoulay, N., Zaks-Hoffer, G., Gilad, N.K., Orenstein, N., Bernard, G., Thiffault, I., Denecke, J., Herget, T., Kortüm, F., Kubisch, C., Bähring, R., Kindler, S., 2024. Etiological involvement of *KCND*1 variants in an X-linked neurodevelopmental disorder with variable expressivity. Am. J. Hum. Genet. 111, 1206–1221.

Kamb, A., Iverson, L.E., Tanouye, M.A., 1987. Molecular characterization of *Shaker*, a *Drosophila* gene that encodes a potassium channel. Cell 50, 405–413.

Kaulin, Yu.A., De Santiago-Castillo, J.A., Rocha, C.A., Covarrubias, M., 2008. Mechanism of the modulation of Kv4:KChIP-1 channels by external K^+. Biophys. J. 94, 1241–1251.

Kim, D.M., Nimigean, C.M., 2016. Voltage-gated potassium channels: A structural examination of selectivity and gating. Cold Spring Harb. Perspect. Biol. 8, a029231.

Kirichok, Y.V., Nikolaev, A.V., Krishtal, O.A., 1998. [K^+]out accelerates inactivation of *Shal*-channels responsible for A-current in rat CA1 neurons. Neuroreport 9, 625–629.

Kise, Y., Kasuya, G., Okamoto, H.H., Yamanouchi, D., Kobayashi, K., Kusakizako, T., Nishizawa, T., Nakajo, K., Nureki, O., 2021. Structural basis of gating modulation of Kv4 channel complexes. Nature 599, 158–164.

Koval, O.M., Fan, Y., Rothberg, B.S., 2007. A role for the S0 transmembrane segment in voltage-dependent gating of BK Channels. J. Gen. Physiol. 129, 209–220.

Kuang, Q., Purhonen, P., Hebert, H., 2015. Structure of potassium channels. Cell. Mol. Life Sci. CMLS 72, 3677–3693.

Kuo, M.M.-C., Haynes, W.J., Loukin, S.H., Kung, C., Saimi, Y., 2005. Prokaryotic K($^+$) channels: from crystal structures to diversity. FEMS Microbiol. Rev. 29, 961–985.

Kurata, H.T., Doerksen, K.W., Eldstrom, J.R., Rezazadeh, S., Fedida, D., 2005. Separation of P/C- and U-type inactivation pathways in Kv1.5 potassium channels. J. Physiol. 568, 31–46.

Kurata, H.T., Fedida, D., 2006. A structural interpretation of voltage-gated potassium channel inactivation. Prog. Biophys. Mol. Biol. 92, 185–208.

Lamothe, S.M., Hogan-Cann, A.E., Li, W., Guo, J., Yang, T., Tschirhart, J.N., Zhang, S., 2018. The N-terminus and transmembrane segment S1 of Kv1.5 can co-assemble with the rest of the channel independently of the S1–S2 linkage. J. Biol. Chem. 293, 15347–15358.

Levy, D.I., Deutsch, C., 1996. A voltage-dependent role for K^+ in recovery from C-type inactivation. Biophys. J. 71, 3157–3166.

Lin, L., Long, L.K., Hatch, M.M., Hoffman, D.A., 2014. DPP6 domains responsible for its localization and function. J. Biol. Chem. 289, 32153–32165.

Long, S.B., Tao, X., Campbell, E.B., MacKinnon, R., 2007. Atomic structure of a voltage-dependent K^+ channel in a lipid membrane-like environment. Nature 450, 376–382.

López-Barneo, J., Hoshi, T., Heinemann, S.H., Aldrich, R.W., 1993. Effects of external cations and mutations in the pore region on C-type inactivation of Shaker potassium channels. Receptors Channels 1, 61–71.

Ma, D., Zhao, C., Wang, X., Li, X., Zha, Y., Zhang, Y., Fu, G., Liang, P., Guo, J., Lai, D., 2022. Structural basis for the gating modulation of Kv4.3 by auxiliary subunits. Cell Res. 32, 411–414.

Maffie, J., Blenkinsop, T., Rudy, B., 2009. A novel DPP6 isoform (DPP6-E) can account for differences between neuronal and reconstituted A-type K^+ channels. Neurosci. Lett. 449, 189.

Maffie, J., Rudy, B., 2008. Weighing the evidence for a ternary protein complex mediating A-type K^+ currents in neurons. J. Physiol. 586, 5609–5623.

Malloy, C., Ahern, M., Lin, L., Hoffman, D.A., 2022. Neuronal roles of the multifunctional protein dipeptidyl peptidase-like 6 (DPP6). Int. J. Mol. Sci. 23, 9184.

Nadal, M.S., Ozaita, A., Amarillo, Y., Miera, E.V.-S. de, Ma, Y., Mo, W., Goldberg, E.M., Misumi, Y., Ikehara, Y., Neubert, T.A., Rudy, B., 2003. The CD26-related dipeptidyl aminopeptidase-like protein DPPX is a critical component of neuronal A-Type K^+ channels. Neuron 37, 449–461.

Nakamura, T. Y., Nandi, S., Pountney, D.J., Artman, M., Rudy, B., Coetzee, W.A., 2001. Different effects of the Ca^{2+}-binding protein, KChIP1, on two Kv4 subfamily members, Kv4.1 and Kv4.2. FEBS Lett. 499, 205–209.

Niwa, N., Nerbonne, J.M., 2010. Molecular determinants of cardiac transient outward potassium current I_{to} expression and regulation. J. Mol. Cell. Cardiol. 48, 12–25.

Nowotny, T., Levi, R., 2013. Voltage-Clamp Technique, in: Jaeger, D., Jung, R., Encyclopedia of Computational Neuroscience. Springer, New York, NY, pp. 1–5.

O'Callaghan, D.W., Haynes, L.P., Burgoyne, R.D., 2005. High-affinity interaction of the N-terminal myristoylation motif of the neuronal calcium sensor protein hippocalcin with phosphatidylinositol 4,5-bisphosphate. Biochem. J. 391, 231–238.

Ong, S.T., Tyagi, A., Chandy, K.G., Bhushan, S., 2022. Mechanisms underlying C-type inactivation in Kv channels: lessons from structures of human Kv1.3 and fly *Shaker*-IR Channels. Front. Pharmacol. 13.

Pak, M.D., Baker, K., Covarrubias, M., Butler, A., Ratcliffe, A., Salkoff, L., 1991. m*Shal*, a subfamily of A-type K^+ channel cloned from mammalian brain. Proc. Natl. Acad. Sci. U. S. A. 88, 4386–4390.

Piechotta, P.L., Rapedius, M., Stansfeld, P.J., Bollepalli, M.K., Erhlich, G., Andres-Enguix, I., Fritzenschaft, H., Decher, N., Sansom, M.S.P., Tucker, S.J., Baukrowitz, T., 2011. The pore structure and gating mechanism of K_{2P} channels. EMBO J. 30, 3607–3619.

Pioletti, M., Findeisen, F., Hura, G.L., Minor, D.L., 2006. Three-dimensional structure of the KChIP1-Kv4.3 T1 complex reveals a cross-shaped octamer. Nat. Struct. Mol. Biol. 13, 987–995.

Pischalnikova, A.V., Sokolova, O.S., 2009. The domain and conformational organization in potassium voltage-gated ion channels. J. Neuroimmune Pharmacol. 4, 71–82.

Pruunsild, P., Timmusk, T., 2005. Structure, alternative splicing, and expression of the human and mouse KCNIP gene family. Genomics 86, 581–593.

Qi, S.Y., Riviere, P.J., Trojnar, J., Junien, J.-L., Akinsanya, K.O., 2003. Cloning and characterization of dipeptidyl peptidase 10, a new member of an emerging subgroup of serine proteases. Biochem. J. 373, 179–189.

Ramachandran, P.L., Craig, T.A., Atanasova, E.A., Cui, G., Owen, B.A., Bergen, H.R., Mer, G., Kumar, R., 2012. The potassium channel interacting protein 3 (DREAM/KChIP3) heterodimerizes with and regulates calmodulin function. J. Biol. Chem. 287, 39439–39448.

Rasmusson, R.L., Morales, M.J., Castellino, R.C., Zhang, Y., Campbell, D.L., Strauss, H.C., 1995. C-type inactivation controls recovery in a fast inactivating cardiac K^+ channel (Kv1.4) expressed in *Xenopus* oocytes. J. Physiol. 489, 709–721.

Rasmusson, R.L., Morales, M.J., Wang, S., Liu, S., Campbell, D.L., Brahmajothi, M.V., Strauss, H.C., 1998. Inactivation of voltage-gated cardiac K^+ channels. Circ. Res. 82, 739–750.

Reddi, R., Matulef, K., Riederer, E.A., Whorton, M.R., Valiyaveetil, F.I., 2022. Structural basis for C-type inactivation in a *Shaker* family voltage-gated K^+ channel. Sci. Adv. 8, eabm8804.

Rhodes, K.J., Carroll, K.I., Sung, M.A., Doliveira, L.C., Monaghan, M.M., Burke, S.L., Strassle, B.W., Buchwalder, L., Menegola, M., Cao, J., An, W.F., Trimmer, J.S., 2004. KChIPs and Kv4 α-subunits as integral components of A-type potassium channels in mammalian brain. J. Neurosci. 24, 7903–7915.

Salinas, M., Duprat, F., Heurteaux, C., Hugnot, J.P., Lazdunski, M., 1997. New modulatory alpha subunits for mammalian *Shab* K^+ channels. J. Biol. Chem. 272, 24371–24379.

Salkoff, L., Butler, A., Ferreira, G., Santi, C., Wei, A., 2006. High-conductance potassium

channels of the *SLO* family. Nat. Rev. Neurosci. 7, 921–931.

Scannevin, R.H., Wang, K., Jow, F., Megules, J., Kopsco, D.C., Edris, W., Carroll, K.C., Lü, Q., Xu, W., Xu, Z., Katz, A.H., Olland, S., Lin, L., Taylor, M., Stahl, M., Malakian, K., Somers, W., Mosyak, L., Bowlby, M.R., Chanda, P., Rhodes, K.J., 2004. Two N-terminal domains of Kv4 K^+ channels regulate binding to and modulation by KChIP1. Neuron 41, 587–598.

Serôdio, P., Rudy, B., 1998. Differential expression of Kv4 K^+ channel subunits mediating subthreshold transient K^+ (A-type) currents in rat brain. J. Neurophysiol. 79, 1081–1091.

Shahidullah, M., Covarrubias, M., 2003. The link between ion permeation and inactivation gating of Kv4 Potassium Channels. Biophys. J. 84, 928–941.

Shibata, R., Misonou, H., Campomanes, C.R., Anderson, A.E., Schrader, L.A., Doliveira, L.C., Carroll, K.I., Sweatt, J.D., Rhodes, K.J., Trimmer, J.S., 2003. A fundamental role for KChIPs in determining the molecular properties and trafficking of Kv4.2 potassium channels. J. Biol. Chem. 278, 36445–36454.

Strassle, B.W., Menegola, M., Rhodes, K.J., Trimmer, J.S., 2005. Light and electron microscopic analysis of KChIP and Kv4 localization in rat cerebellar granule cells. J. Comp. Neurol. 484, 144–155.

Strop, P., Bankovich, A.J., Hansen, K.C., Christopher Garcia, K., Brunger, A.T., 2004. Structure of a human A-type potassium channel interacting protein DPPX, a member of the dipeptidyl aminopeptidase family. J. Mol. Biol. 343, 1055–1065.

Su, T., Cong, W.D., Long, Y.S., Luo, A.H., Sun, W.W., Deng, W.Y., Liao, W.P., 2008. Altered expression of voltage-gated potassium channel 4.2 and voltage-gated potassium channel 4-interacting protein, and changes in intracellular calcium levels following lithium-pilocarpine-induced status epilepticus. Neuroscience 157, 566–576.

Tan, X.-F., Bae, C., Stix, R., Fernández-Mariño, A.I., Huffer, K., Chang, T.-H., Jiang, J., Faraldo-Gómez, J.D., Swartz, K.J., 2022. Structure of the *Shaker* Kv channel and mechanism of slow C-type inactivation. Sci. Adv. 8, eabm7814.

Treptow, W., Liu, Y., Bassetto, C.A., Pinto, B.I., Alves Nunes, J.A., Uriarte, R.M., Chipot, C.J., Bezanilla, F., Roux, B., 2024. Isoleucine gate blocks K^+ conduction in C-type inactivation. eLife 13, e97696.

Tu, L., Wang, J., Deutsch, C., 2007. Biogenesis of the T1−S1 Linker of voltage-gated K^+ channels. Biochemistry 46, 8075–8084.

Van Hoorick, D., Raes, A., Keysers, W., Mayeur, E., Snyders, D.J., 2003. Differential modulation of Kv4 kinetics by *KCHIP*1 splice variants. Mol. Cell. Neurosci. 24, 357–366.

Van Hoorick, D., Raes, A., Snyders, D.J., 2007. The aromatic cluster in *KCHIP*1b affects Kv4 inactivation gating: The aromatic cluster in KChIP1b. J. Physiol. 583, 959–969.

Vergara, C., Latorre, R., Marrion, N.V., Adelman, J.P., 1998. Calcium-activated potassium channels. Curr. Opin. Neurobiol. 8, 321–329.

Wang, H., Yan, Y., Liu, Q., Huang, Y., Shen, Y., Chen, L., Chen, Y., Yang, Q., Hao, Q., Wang, K., Chai, J., 2007. Structural basis for modulation of Kv4 K^+ channels by auxiliary KChIP subunits. Nat. Neurosci. 10, 32–39.

Wang, N., Dries, E., Fowler, E.D., Harmer, S.C., Hancox, J.C., Cannell, M.B., 2022. Inducing $I_{to,f}$ and phase 1 repolarization of the cardiac action potential with a Kv4.3/KChIP2.1 bicistronic transgene. J. Mol. Cell. Cardiol. 164, 29.

Weber, W.-M., 1999. Endogenous ion channels in oocytes of *Xenopus laevis*: Recent developments. J. Membr. Biol. 170, 1–12.

Wei, A., Covarrubias, M., Butler, A., Baker, K., Pak, M., Salkoff, L., 1990. K^+ current diversity is produced by an extended gene family conserved in *Drosophila* and mouse. Science 248, 599–603.

Wollberg, J., Bähring, R., 2016. Intra- and inter-subunit dynamic binding in Kv4.2 channel closed-State inactivation. Biophys. J. 110, 157–175.

Wu, L.-Y., Song, Y.-J., Zhang, C.-L., Liu, J., 2023. Kv channel-interacting proteins in the neurological and cardiovascular Systems: An updated review. Cells 12, 1894.

Xia, K., Xiong, H., Shin, Y., Wang, D., Deerinck, T., Takahashi, H., Ellisman, M.H., Lipton, S.A., Tong, G., Descalzi, G., Zhang, D., Zhuo, M., Zhang, Z., 2010. Roles of KChIP1 in the regulation of GABA-mediated transmission and behavioral anxiety. Mol. Brain 3, 23.

Xiong, H., Kovacs, I., Zhang, Z., 2004. Differential distribution of KChIPs mRNAs in adult mouse brain. Brain Res. Mol. Brain Res. 128, 103–111.

Xiong, H., Xia, K., Li, B., Zhao, G., Zhang, Z., 2009. KChIP1: a potential modulator to GABAergic system. Acta Biochim. Biophys. Sin. 41, 295–300.

Xu, Y., McDermott, A.E., 2019. Inactivation in the potassium channel KcsA. J. Struct. Biol. X 3, 100009.

Ye, W., Zhao, H., Dai, Y., Wang, Y., Lo, Y., Jan, L.Y., Lee, C.-H., 2022. Activation and

closed-state inactivation mechanisms of the human voltage-gated Kv4 channel complexes. Mol. Cell 82, 2427-2442.e4.

Zagha, E., Ozaita, A., Chang, S.Y., Nadal, M.S., Lin, U., Saganich, M.J., McCormack, T., Akinsanya, K.O., Qi, S.Y., Rudy, B., 2005. DPP10 modulates Kv4-mediated A-type potassium channels. J. Biol. Chem. 280, 18853–18861.

Zhang, Y., MacLean, J.N., An, W.F., Lanning, C.C., Harris-Warrick, R.M., 2003. KChIP1 and frequenin modify *Shal*-evoked potassium currents in pyloric neurons in the lobster stomatogastric ganglion. J. Neurophysiol. 89, 1902–1909.

Zhou, W., Qian, Y., Kunjilwar, K., Pfaffinger, P.J., Choe, S., 2004. Structural insights into the functional interaction of KChIP1 with *Shal*-type K^+ channels. Neuron 41, 573–586.

8. Abbreviations

ANOVA	Analysis of variance
b-APs	Back-propagating action potentials
BK	“big” potassium
CA	Cornu Ammonis
CHO	Chinese hamster ovary
CNS	Central nervous systems
Cryo-EM	Cryogenic electron microscopy
CSI	Closed-state inactivation
DEPC	Diethyl pyrocarbonate
DNA	Deoxyribonucleic acid
DPPs	Dipeptidyl amino peptidase-related proteins
DREAM	Downstream regulatory element antagonistic modulator
EAG	The Ether à-go-go
eag	*eag*- ether à-go-go
erg	*erg*- ether à-go-go
elk	*elk*- ether à-go-go
EPSPs	Excitatory postsynaptic potentials
GC	Granule cell
G-V	Conductance-voltage
HEK	Human embryonic kidney
HEPES	Hydroxyethylpiperazine-ethansulfonicate
i.e.	id est
I_{SA}	Somatodendritic subthreshold A-type K^+ current
I_{to}	Transient outward current
I-V	Current-voltage
Kir	Inward-rectifier potassium channel
K_{2P}	Two-pore domain potassium
Kv	Voltage-gated potassium
KIS	Kv channel inactivation suppressor
NCS	Neuronal calcium sensor
OSI	Open-state inactivation
PCR	Polymerase chain reaction

RNA	Ribonucleic acid
S1-S6	Six transmembrane segments
SD	Standard deviation
SEM	Standard error of the mean
SKCa	Small conductance Ca^{2+}-activated K^{+}
T1	Tetramerisation
TEA	Tetraethylammonium
TEVC	Two-electrode voltage clamp
TMD	Transmembrane domain
UV	Ultraviolet
VSD	Voltage-sensing domain

9. List of Figures

10. List of Tables

11. Publication

Wuyou Cao, Georgios Tachtsidis & Robert Bähring (2024). Modification of human Kv4 channels by KChlP1 splice variants. Poster presentation at Annual Meeting ofthe German Physiological Society (103rd), Austrian Physiological Society and Life Sciences Switzerland (LS2) Physiology in Vienna.

12. Declaration of personal contribution

This study was conducted at Institute of Cellular and Integral Physiology in Universitätsklinikum Hamburg-Eppendorf under the supervision of Prof. Dr. Robert Bähring. I contributed the following:

1) Study concept: collaborative discussion on research design, experimental conditions and interpretation of results;
2) Heterologous channel expression: frog surgery assistance, oocytes preparation, cRNA preparation and injection, solutions preparation;
3) Electrophysiological experiments: experimental set-up including preparation of electrodes, recording system, and recording solutions, TEVC recordings;
4) Data collection and analysis: raw data analysis including current recordings evaluation with software, statistical analysis;
5) Manuscript writing: text writing, figures and summary tables.

13. Eidesstattliche Versicherung

Ich versichere ausdrücklich, dass ich die Arbeit selbständig und ohne fremde Hilfe, insbesondere ohne entgeltliche Hilfe von Vermittlungs- und Beratungsdiensten, verfasst, andere als die von mir angegebenen Quellen und Hilfsmittel nicht benutzt und die aus den benutzten Werken wörtlich oder inhaltlich entnommenen Stellen einzeln nach Ausgabe (Auflage und Jahr des Erscheinens), Band und Seite des benutzten Werkes kenntlich gemacht habe. Das gilt insbesondere auch für alle Informationen aus Internetquellen.

Soweit beim Verfassen der Dissertation KI-basierte Tools („Chatbots“) verwendet wurden, versichere ich ausdrücklich, den daraus generierten Anteil deutlich kenntlich gemacht zu haben. Die „Stellungnahme des Präsidiums der Deutschen Forschungsgemeinschaft (DFG) zum Einfluss generativer Modelle für die Text- und Bilderstellung auf die Wissenschaften und das Förderhandeln der DFG“ aus September 2023 wurde dabei beachtet.

Ferner versichere ich, dass ich die Dissertation bisher nicht einem Fachvertreter an einer anderen Hochschule zur Überprüfung vorgelegt oder mich anderweitig um Zulassung zur Promotion beworben habe.

Ich erkläre mich damit einverstanden, dass meine Dissertation vom Dekanat der Medizinischen Fakultät mit einer gängigen Software zur Erkennung von Plagiaten überprüft werden kann.

Datum 12.05.2025 Unterschrift Cao, Wuyou

14. Acknowledgements

Firstly, I would like to express my deepest thank to my supervisor, Prof. Dr. Robert Bähring for giving me the opportunity to complete this interesting project in his research group. Without his continuous supervision, support, great care and encouragement, I couldn't finish my project. He is always patient to answer my questions and tells me it's no need to worry and he will help me whenever I face problems. Besides scientific study, he also shares me a lot interesting stories in Germany, which help me better understand the way of life here. I'm so grateful and will always treasure this wonderful experience to work with him.

I want to thank colleagues at the Institute of Cellular and Integral Physiology for their kindness. Many thanks to Prof. Dr. Catherine Meyer-Schwesinger and Claudia Kollien for helping me work smoothly at the institute. Thanks to Tassja Kalm, Fabian Schönewald and Dr. Georgios Tachtsidis for working together in Robert's group. Especially George, as we spend a lot of time in the lab and office. I felt enjoyable to discuss with him not only about science but also our common hobbies. Special thanks to Man Wang, Leya Eckermann-Reimer, Kimberley Dreger and Johannes Brand. I really enjoy chatting with them, which helps me relax during my work breaks. I also want to thank Prof. Dr. Christiane Bauer for providing me with different research perspectives. Many thanks to Annett Hasse and Peter Bassalay for helping me overcoming technical problems.

And then I'd like to thank the China Scholarship Council (CSC) for financial support. Finally, a heartfelt thank also goes to my family and my friends. Without their sweet support, I will not be able to overcome the difficulties in a foreign country.